



Title	Studies on Plasmon-Driven Efficient Multi-Electron Transfer Reactions at Electrified Interfaces
Author(s)	王, 禹淳
Citation	北海道大学. 博士(理学) 甲第14258号
Issue Date	2020-09-25
DOI	10.14943/doctoral.k14258
Doc URL	<a href="http://hdl.handle.net/2115/82720">http://hdl.handle.net/2115/82720</a>
Type	theses (doctoral)
File Information	Yuchun_Wang.pdf



[Instructions for use](#)

**Studies on plasmon-driven efficient multi-electron  
transfer reactions at electrified interfaces**

(電気化学界面におけるプラズモン誘起高効率多電子移動反  
応に関する研究)

WANG Yuchun

*Graduate School of Chemical Sciences and Engineering  
Hokkaido University*

2020

# Contents

<b>Chapter 1. General introduction</b> .....	1
<b>1.1 Utilization of solar energy</b> .....	1
<b>1.2 Plasmonic photon energy utilization</b> .....	1
<b>1.3 Plasmonic strong coupling</b> .....	5
<b>1.4 Plasmon induced photocatalysis reaction</b> .....	9
<b>1.5 Detecting the fermi level of photocatalysis electrode</b> .....	17
<b>1.6 Investigation of oxygen evolution reaction on different catalysis</b> .....	19
<b>1.7 Problems and target of our research</b> .....	28
<b>1.8 Objective and outline of this thesis</b> .....	29
<b>References</b> .....	29
<b>Chapter 2. Active tuning the strong coupling state between Ag/MoS<sub>2</sub> heterostructure via electrochemical method</b> .....	36
<b>2.1 Introduction</b> .....	36
<b>2.2 Experimental</b> .....	38
<b>2.3 Results and discussion</b> .....	39
<b>2.3.1 Determination of layer number of MoS<sub>2</sub></b> .....	39
<b>2.3.2 Interaction between MoS<sub>2</sub> and Ag LSPR in air</b> .....	40
<b>2.3.3 Active tuning of the strong coupling state between MoS<sub>2</sub> and Ag silver by electrochemical method</b> .....	42
<b>2.4 Conclusion</b> .....	44
<b>References</b> .....	44
<b>Chapter 3. In-situ monitoring of electronic structure of modal strong coupling electrode for enhanced plasmonic water oxidation</b> .....	47
<b>3.1 Introduction</b> .....	47
<b>3.2 Experimental</b> .....	49
<b>3.2.1 Preparation of the Au NPs / TiO<sub>2</sub> / Au film (ATA) substrate</b> .....	49
<b>3.2.2 Preparation of graphene supported ATA and Raman measurements</b> .....	49
<b>3.3 Results and discussion</b> .....	49
<b>3.4 Conclusion</b> .....	60
<b>References</b> .....	61
<b>Chapter 4. Investigation on the unique reaction mechanism of OER on plasmonic photoelectrode</b> .....	67
<b>4.1 Introduction</b> .....	67

<b>4.2 Experimental.....</b>	<b>68</b>
<b>4.3 Results and discussion.....</b>	<b>70</b>
<b>4.4 Conclusion.....</b>	<b>72</b>
<b>References .....</b>	<b>73</b>
<i>Chapter 5. Acceleration of water oxidation reaction on Ni-Loaded Au / TiO<sub>2</sub> electrode by plasmon.....</i>	<i>75</i>
<b>5.1 Introduction .....</b>	<b>75</b>
<b>5.2 Experimental.....</b>	<b>76</b>
<b>5.3 Results and discussion.....</b>	<b>77</b>
<b>5.4 Conclusion.....</b>	<b>87</b>
<b>References .....</b>	<b>88</b>
<i>Chapter 6. General Conclusion .....</i>	<i>90</i>
<b>Acknowledgements .....</b>	<b>92</b>

## *Chapter 1.*

### **General introduction**

---

#### **1.1 Utilization of solar energy**

As one of the most renewable, clean and environment-friendly energy, the utilization of solar energy has attracted great attention since the reserve of traditional fossil fuel has been reduced dramatically. Plenty of work and efforts has been devoted in this field, including the development and optimization of photovoltaic devices, photochemistry and molecular photocatalysis and great achievements have been achieved.<sup>1-3</sup>

#### **1.2 Plasmonic photon energy utilization**

From the environmental point of view, the photon energy conversion system has always been regarded as the effective solution for the energy problem.<sup>4-5</sup> However, a lot of limitations prevent the application. For instance, the low absorption cross-section of materials, the low utilization efficiency of visible light, or the low incident photon-to-electron conversion efficiency.<sup>6-7</sup> Plasmonic system is now considered as an effect method to overcome these problems, since the absorption of metal nanoparticles reaches maximum when the light is at the plasmon frequency and the typical plasmon band appears at visible to near infrared regions.

##### **1.2.1 Concept and definition of plasmon resonance**

Plasmon resonance is defined as the collective oscillation of free electrons inside metal induced by the incident light.<sup>7-9</sup> It can also be described as the quantized plasma oscillation. One can consider as that plasmon is the mechanical oscillation of electron gas inside the metal. Due to the external electromagnetic field, the displacement of electron gas occurs from the fixed ionic cores. For bulk plasmon, the energy at plasma frequency is described as follow:<sup>7</sup>

$$E_p = \hbar \sqrt{\frac{ne^2}{m\epsilon_0}}$$

where  $n$  is the electron density,  $m$  is the electron mass  $e$  is the electron charge and  $\epsilon_0$  is the permittivity of free space.<sup>7</sup>

When the surface plasmon is localized into nanoscale which is comparable to the wavelength of light, it termed a localized surface plasmon resonance (LSPR). The electromagnetic field are dramatically enhanced in the vicinity of metal nanoparticles while falling off rapidly with distance. At the plasmon resonant frequency, the extinction of the metal nanoparticles reaches the maximum, as Fig.1.1 (a) and (b) shown.<sup>7, 10</sup>

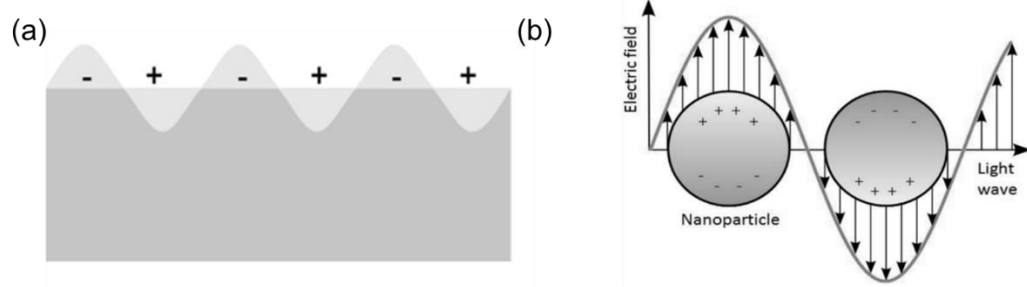


Figure 1.1. Schematic diagram of (a) surface plasmons<sup>7</sup> and (b) a localized surface plasmon.<sup>10</sup>

### 1.2.2 Effects of particle size, shape, and material on plasmon resonance

According to Mie theory, if the radius of spherical particles is less than the wavelength of instant light, the cross-section of absorption and scattering of LSPR could be described as follow:<sup>11</sup>

$$C_{sca} = \frac{8\pi}{3} k^4 a^6 \left| \frac{\epsilon - \epsilon_m}{\epsilon + 2\epsilon_m} \right|^2$$

$$C_{abs} = 4\pi k a^3 \text{Im} \left[ \frac{\epsilon - \epsilon_m}{\epsilon + 2\epsilon_m} \right]$$

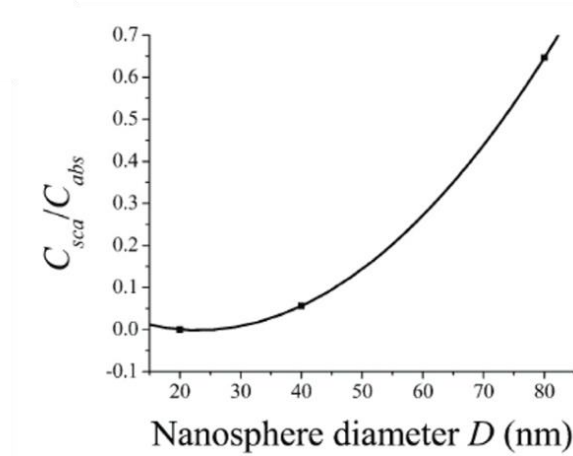


Figure 1.2. Correlation between  $C_{sca}/C_{abs}$  and radius of particles.<sup>12</sup>

where  $k = 2\pi/\lambda$  is the wavenumber,  $\varepsilon$  and  $\varepsilon_m$  are dielectric function of metal and medium respectively and  $a$  is the radius of metal nanoparticles.

From the above functions, we could conclude that  $C_{abs}$  and  $C_{sca}$  is related with the radius of metal nanoparticles. The  $C_{abs}$  is proportional to the radius of particles  $a^3$  while  $C_{sca}$  is proportional to  $a^6$ . Fig.1.2 shows the correlation between  $C_{sca}/C_{abs}$  and radius of particles. From it, it can be found that the scattering becomes dominant as the size of particle increase.

Although Mie theory is based on a simple approximation that the nanoparticles are sphere, a lot of experiment and calculation have proved that plasmon is influenced by the shape of particles. Mock *et al.* fabricated silver nanoparticles with different shape. The wavelength of LSPR appeared at different positions, as shown in Fig. 1.3.<sup>12</sup>

Apart from the size and shape, the properties of metal materials also influence plasmon. It has been known that the frequency of LSPR is related with the dielectric constant of media  $\varepsilon_m$  and LSPR should satisfy the condition of  $\varepsilon_1 = -2\varepsilon_m$ , thus it is self-evident that for different kinds of metal, LSPR differs from each other. Taking silver and gold as an example, the real and imaginary part of the dielectric function of Ag and Au is shown in Fig. 1.4. Link *et al.* fabricated Au-Ag alloy and discussed the dependence of absorption on the composition. They found that when increase the proportion of Au, LSPR red shifts.<sup>13</sup>

The combination of plasmonic materials with wide bandgap semiconductor electrodes can allow increase the charge separation efficiency as the recombination of carriers can be reduced via injection of carriers to the conduction band.

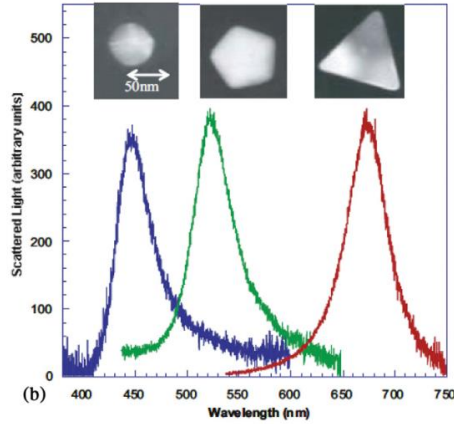


Figure 1.3. Scattering spectra of silver nanoparticles with different size and shape.<sup>15</sup>

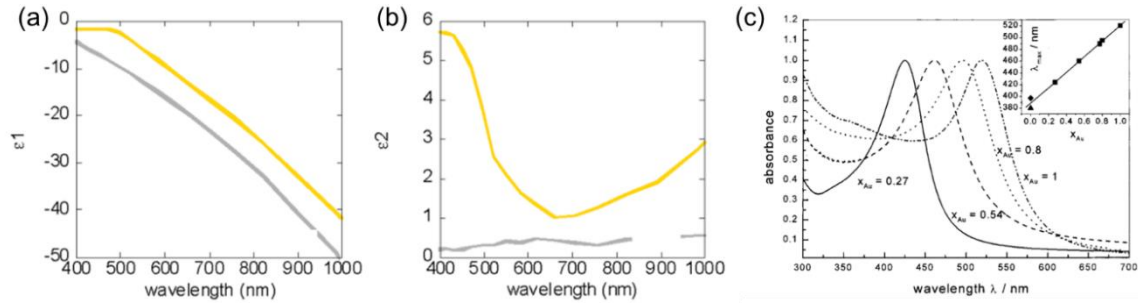


Figure 1.4. The (a) real (b) imaginary part of dielectric function of gold and silver. Yellow line indicates gold and gray line indicates silver. (c) absorption spectra of Au and Au-Ag alloy nanoparticles with different amount of Au. The inset figure indicates the relationship between the peak position of the absorption and the fraction of gold.<sup>13</sup>

### 1.2.3 Decay process of LSPR in metal nanoparticles

When the metal nanoparticles are exposed to instant light, LSPR is generated. After that, LSPR will decay via either radiative or nonradiative way. As Fig.1.5 illustrates, via radiative way, a photon is emitted, while in the case of nonradiative way, hot carriers are generated within 1~100 fs by both interband or intraband excitation. These hot carriers can



be used to induce chemical reactions. After that, electron-electron scattering takes place within 100 fs to 1 ps. Some hot electrons relax and loss energy because of this scattering, while the secondly electron-hole pair can be generated owing to this process. Later, electrons will scatter with phonons and the energy of plasmon will convert to heat within 100 ps to 10 ns.<sup>14-15</sup>

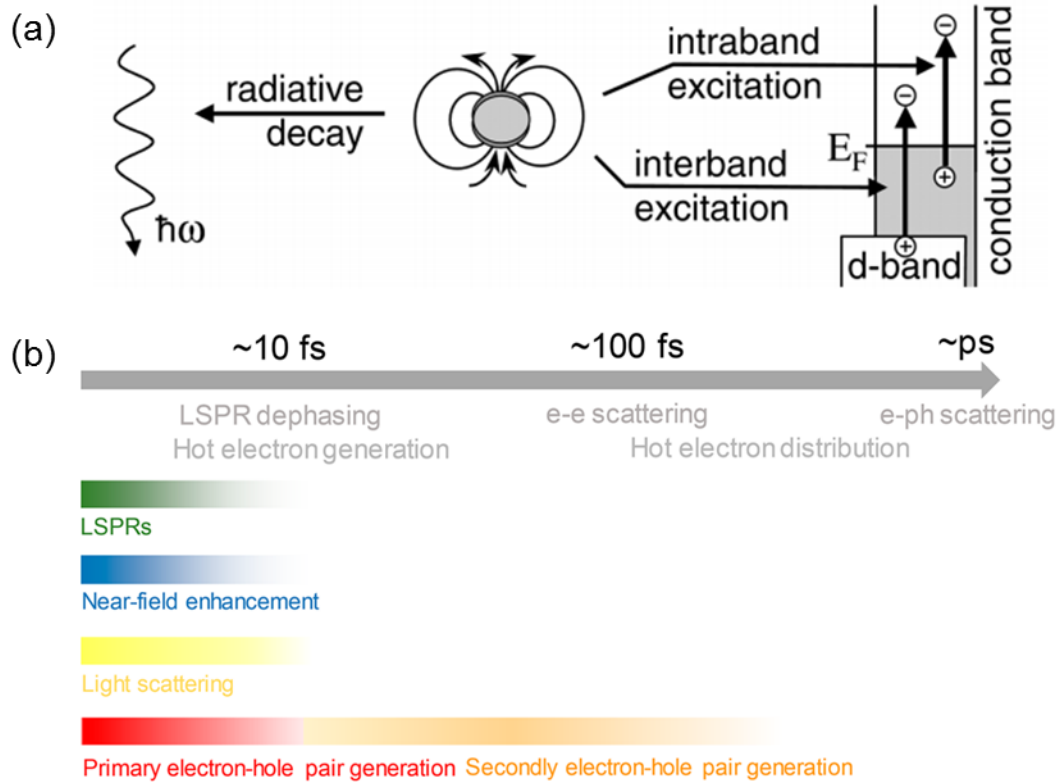


Figure 1.5. (a) Illustration of decay process of LSPR in metal nanoparticles via both radiative or nonradiative way. (b) Time domains of different process involved in plasmonic devices.<sup>14-15</sup>

### 1.3 Plasmonic strong coupling

For the efficient utilization of the light energy, the arbitrary tune of the light-matter interaction is one of the addressing issues. The criterion to access the magnitude of interaction is named coupling strength,  $g$ . According to the relative magnitudes of coupling strength  $g$  and decay rates of the matter polarization ( $\gamma_e$ ) and the light in the cavity ( $\gamma_c$ ), the

system could be divided to three regimes. (1) weak coupling regime, where  $g < 1/2(\gamma_e - \gamma_c)$ , In this region, the eigenstates of the system is unchanged and the Purcell effect could be observed. (2) intermediate coupling regime, where  $1/2(\gamma_e - \gamma_c) < g < \sqrt{\frac{1}{2}(\gamma_e^2 + \gamma_c^2)}$ . In this region, the normal mode splitting occurs and the anticrossing behavior is gradually generated. (3), when  $g > \sqrt{\frac{1}{2}(\gamma_e^2 + \gamma_c^2)}$ , the system is considered as strong coupling system. In this regime, the interchanging rate between optical cavities and the emitters exceeds the dissipation rate for each other, a new hybridized state could be generated.

This new hybridized state called Rabi splitting has been recognized as the promising prospect for improving energy efficiency.<sup>16</sup> Plasmonic cavity is the enhanced highly polarized electromagnetic field induced by the light illumination onto noble metal nanoparticles. Recently, the plasmonic cavity has been widely applied to the strong coupling because of its strong field localization.<sup>17</sup>

Wen *et al.* discussed the strong coupling formed between WS<sub>2</sub> and the optical environment of Au nanorod supported plasmon, as Fig. 1.6 shows. They realized the room temperature control of strong coupling. They also stressed another two conditions which are necessary to demonstrate the entrance of strong coupling regime: a spectra dip and anti-crossing behavior which depended on the plasmon mode. In order to make sure that the gold nanorod-WS<sub>2</sub> structure entered the strong coupling regime, they prepare gold nanorod with different longitudinal plasmon modes by varying their aspect ratios. As the longitudinal plasmon mode energies were continuously changed across the transition energy of exciton, from the scattering spectra, two distinguished hybrid modes existed indicating that strong coupling takes place when the interaction between an emitter and the optical cavity is strong and their respective dissipation of rates can be overcome by this exchange.<sup>18</sup>

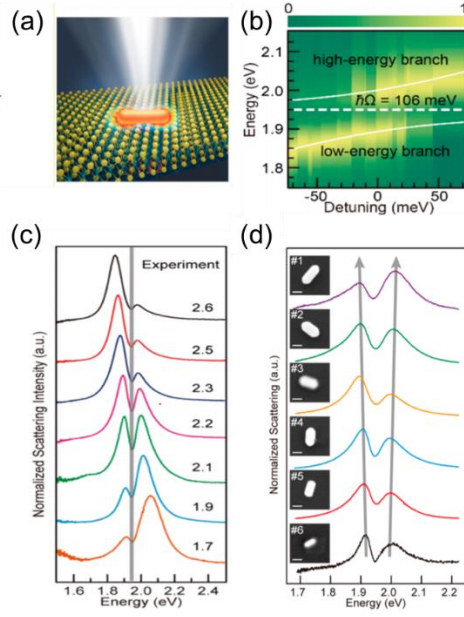


Figure 1.6. (a) Illustration of the Au nanorod – WS<sub>2</sub> system. (b) Normalized scattering spectra of the Au nanorod – WS<sub>2</sub> system with different detunings. Normalized scattering spectra of the heterostructures. (c) Aspect ratio of Au nanorod ranging from 1.7 to 2.6 and (d) Au volumes and polarizations are different.<sup>18</sup>

Nagasawa *et al.* investigated the strong coupling between Ag LSPR and dye molecule, as Fig. 1.7 shows. They prepared the Ag dimer structure and tuning the coupling strength by changing the distance between the dimer structure. They applied this strong coupling system to the surface enhanced Raman spectra (SERS) and they found that at the optimized resonant energy between the hybrid states and Raman excitation, Raman scattering cross section could be effectively enhanced.<sup>19</sup>

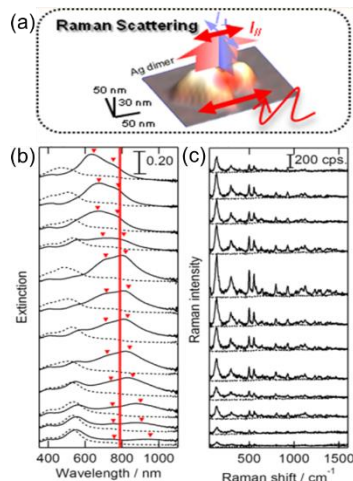


Figure 1.7. (a) illustration of Ag dimer. (b) extinction of Ag@HITC with different gap distance of Ag. (c) Polarized Raman spectra obtained on the surface of Ag@HITC.<sup>19</sup>

Kato *et al.* did some work to understand the strong coupling state between Au nanostructures and dye molecules, as Fig. 1.8 shows. They succeed in the active tuning of the number of dye molecules by electrochemical methods. They also found the novel dependence of strong coupling on the applied electrochemical potential. The number of dye molecule is not only related with the redox state but also increasing the coupling strength thus enhancing the interaction between dye molecule and metal surface.<sup>20</sup>

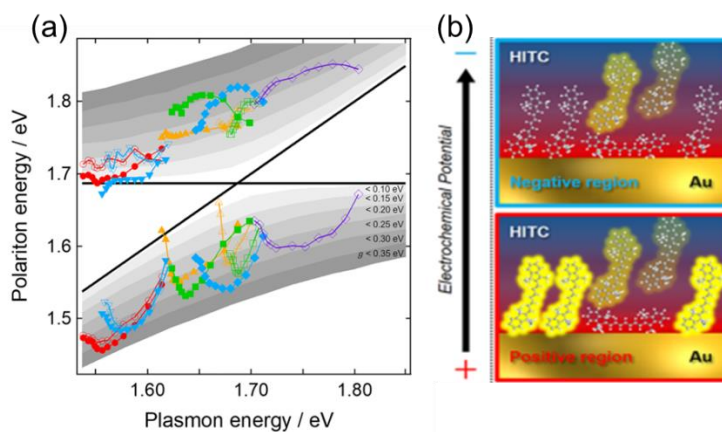


Figure 1.8. (a) Dispersion relations of  $\omega_{UB}$  and  $\omega_{LB}$  vs.  $\omega_{LSP}$  at electrode with different Ag height. (b) Illustration of the active tuning of dye molecules by electrochemical potential.<sup>20</sup>

Strong coupling with plasmon cavity exhibits great advantages compared with common optical cavity. First, the mode volume of plasmonic cavity is extremely low, fulfilling high coupling strength.<sup>21</sup> Second, the field confinement property of plasmon lead to an enhancement of field, which enables the detection using surface enhanced Raman spectra (SERS).<sup>22</sup> Third, amount of molecule emitters could be increased, the dipole moment could also be increased, generating a higher coupling strength.<sup>23</sup> Based on the above advantages, plasmonic strong coupling is always be the focus of research.

#### **1.4 Plasmon induced photocatalysis reaction**

Plasmon induced photocatalysis has captured much attention because of its high catalysis performance.<sup>24-26</sup> Compared with the common semiconductor photocatalysis, plasmonic photocatalysis combines semiconductors and noble metal nanoparticles together. With the unique properties of such system, the recombination of carriers are reduced, resulting in the high light utilization efficiency.

##### **1.4.1 Plasmon induced carrier separation**

The charge separation efficiency was proposed by Tatsuma's group.<sup>27-28</sup> They prepared the Ag or Au nanoparticles with TiO<sub>2</sub> sol gel film. To explain the enhancement of incident photon-to-current efficiency (IPCE), they proposed the mechanism of plasmon induced charge separation (PICS). As show in Fig. 1.9, when the system was exposed to light, hot electrons are excited and injected to TiO<sub>2</sub> and electrons and holes could separate efficiently.

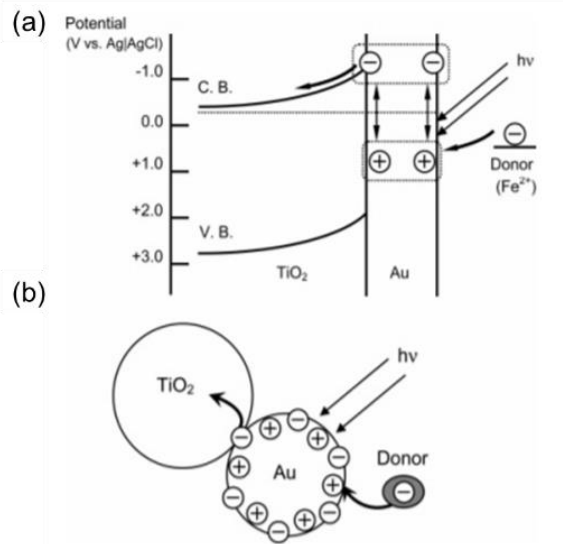


Figure 1.9. (a) The mechanism for the plasmon-assisted photoelectrochemistry. (b) Charge separation progress at a gold nanoparticle-TiO<sub>2</sub> system with visible light.<sup>28</sup>

In this case, hot electrons are generated in metal and subsequently injected to the semiconductor. Later it was discovered that the hot electrons could be excited directly to semiconductor or absorbed molecule.<sup>29-30</sup> As shown in Fig. 1.10, Linic *et al.* prepared Ag nanoparticles with methylene blue (MB) absorbed. By measuring the ration between anti-Stokes and Stokes phenomenon using Raman, the temperatures of Ag nanoparticles and MB could be obtained and the conclusion of hot electrons directly injected to the unoccupied orbit of MB could be obtained.

The generating position of hot carriers in metal also influence the carrier separation. As Fig. 1.11 shows, Uskov *et al.* studied two mechanisms of photoelectrons injected from plasmonic materials as surface charge separation (a) and distal charge separation (b). Their work revealed that surface charge separation can generate larger photoelectric effect than distal charge separation, as the former reduced the contact possibility of hot electrons with low energy electrons and the discontinuity of the dielectric permittivity at the boundary.<sup>31</sup>

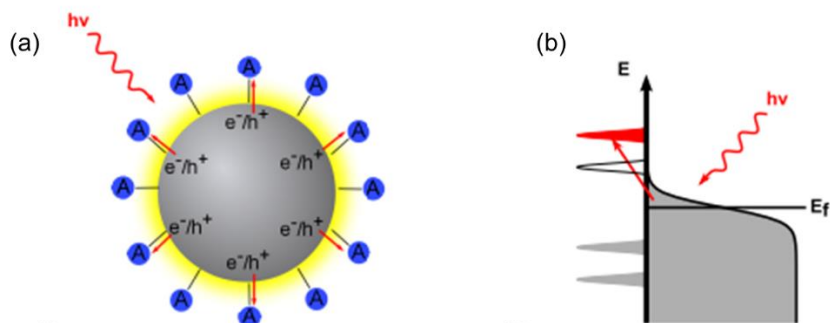


Figure 1.10. (a) Illustration of the structure of Ag nanoparticles with MB absorbed. (b) Energy diagram of MB / Ag when it is exposed to light of 785 nm wavelength. Electrons are excited to the unoccupied orbit of MB directly.<sup>29</sup>

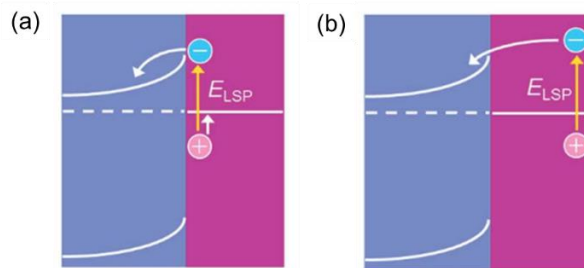


Figure 1.11. (a) Plasmon induced surface charge separation and (b) distal charge separation.<sup>31</sup>

Apart from these mechanism, plasmon could also increase the charge separation efficiency by reducing the diffusion length of carriers in semiconductor or triggering the generation of carriers by nanoantenna effect.<sup>32-33</sup>

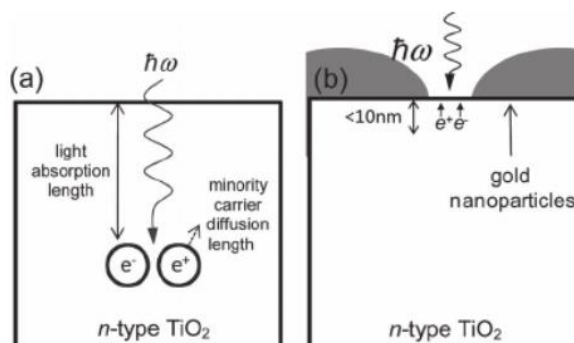


Figure 1.12. Carrier generation in (a) semiconductor (b) plasmon / semiconductor system.<sup>32</sup>

One challenge for photocatalysis with semiconductor is that the light absorption length in semiconductor is much deeper, thus the diffusion length of carriers is long and carriers easily recombine before migrating to the surface to catalyze chemical reaction, as Fig. 1.12 (a) indicates. With plasmon, the localization effect can confine light at the surface and carriers can be generated near the surface. Therefore, the diffusion length is reduced, charge separation efficiency is improved.<sup>32</sup>

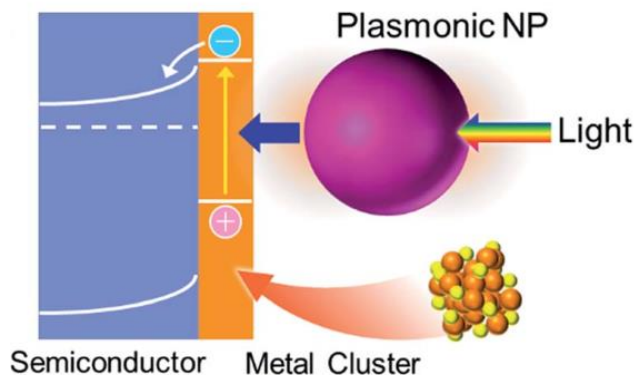


Figure 1.13. Energy diagram of Au cluster /  $\text{TiO}_2$  / Au nanoparticle (NP) system. Au cluster is not plasmonic metal. Au NP serves as nanoantenna to absorb light and excites carriers.<sup>33-34</sup>

Another kind of plasmonic charge separation is through plasmonic nanoantenna effect. As Fig. 1.13 shows, in the system of Au cluster /  $\text{TiO}_2$  / Au nanoparticle (NP), large Au NP served as plasmonic nanoantenna and enhances the absorption of light. Au cluster played a similar role like molecule. When the electrode was exposed to light, due to the nanoantenna effect, light was absorbed and carriers were generated in the surface of semiconductor. Thus charge separation efficiency could also be increased.<sup>33-34</sup>

#### 1.4.2 Plasmonic water splitting

Since plasmonic system can improve the reaction efficiency dramatically, it has been widely used for the water splitting. Misawa *et al.* prepared gold nanostructure on  $\text{TiO}_2$ . When irradiated with visible light, multiple electrons and hole were generated, leading to the high effective water oxidation as in Fig.1.14.<sup>28</sup> Later, they also conducted the water splitting under visible light with strontium titanate ( $\text{SrTiO}_3$ ) single crystal, as Fig. 1.15



shows. The evolution of  $H_2$  and  $O_2$  was demonstrated in their research stoichiometrically. By fixing pH at either the side for  $O_2$  generation and the side for  $H_2$  generation as 13 and 1 and increase or decrease pH of the other side and observing the pH at which evolution of hydrogen and oxygen just took place, they could obtain the chemical bias of this cell. Based on this thinking, the minimum chemical bias of this system was obtained and it was rather low because of plasmon, which indicating a low-energy consuming method for artificial photosynthesis was possible.<sup>26</sup>

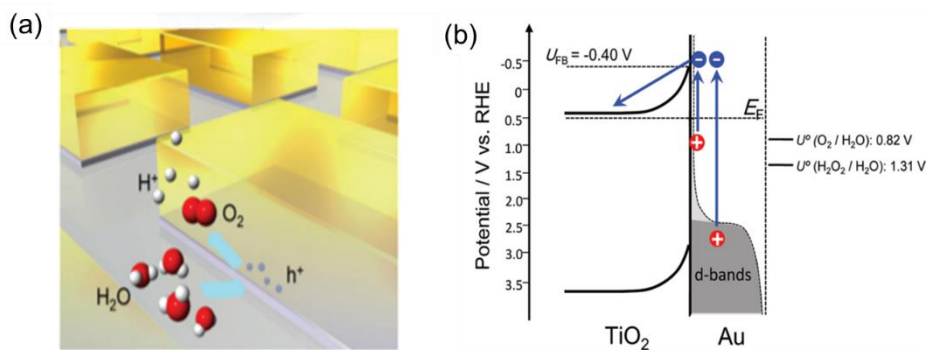


Figure 1.14. (a) Illustration of the structure of the photocatalysis electrode for OER. (b) Energy diagram for the progress of charge separation during OER.<sup>28</sup>

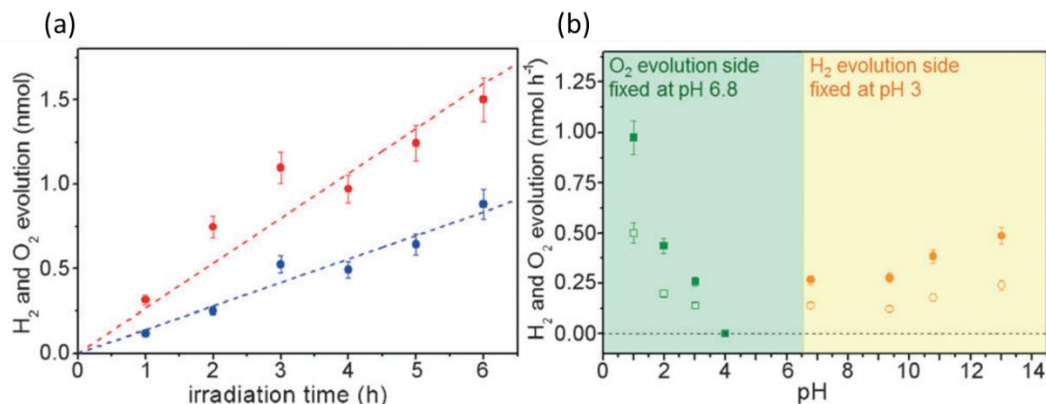


Figure 1.15. Plasmonic water splitting occurred on SrTiO<sub>3</sub> single crystal. (a) Relationship between the gas generation rate and irradiation time. Red circles indicate H<sub>2</sub> and blue circles indicate O<sub>2</sub>. (b) The relationship between gas generation rate and pH.<sup>26</sup>

Maeda *et al.* optimized the Au / TiO<sub>2</sub> plasmonic system for OER by depositing cobalt catalysis on the edge of Au nanoparticles, as shown in the illustration of Fig.1.16 (a). The

principle of the deposition is that when Au / TiO<sub>2</sub> was exposed to light, active sites was generated and holes accumulated at the junction of Au and TiO<sub>2</sub>, therefore cobalt oxides could be deposited selectively. After depositing, the photocurrent was enhanced by three times compared with bare Au/ TiO<sub>2</sub> system. By tuning the amount of electric charge, the amount of cobalt could be controlled thus generating different IPCE.<sup>25</sup>

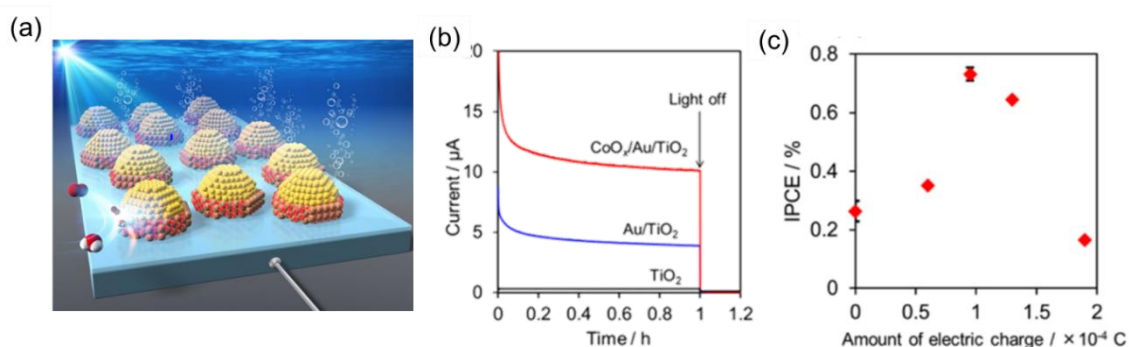


Figure 1.16. (a) Illustration of the structure of the CoO<sub>x</sub> / Au /TiO<sub>2</sub> electrode for OER. (b) Photocurrent on CoO<sub>x</sub> / Au / TiO<sub>2</sub> (red line), Au /TiO<sub>2</sub> (blue line) and TiO<sub>2</sub> (black line) respectively. (c) Relationship between IPCE of CoO<sub>x</sub> / Au / TiO<sub>2</sub> and the amount of charge consumed by deposition.<sup>25</sup>

### 1.4.3 Plasmonic electron transfer reaction

Minamimoto and coworkers triggered the deposition reaction of pyrrole monomers using LSPR supported on Au nanostructures. The active reaction sites were visualized and the localization of the hot spots for reaction can be proved by the morphological characteristics of the deposited conductive polymer. They also managed to determine the electrochemical of holes for oxidation of polypyrrole. From Fig. 17 (b), the Raman intensity at 1600 cm<sup>-1</sup> (C=C, characteristic peak of polypyrrole) varies with applied potential. If the applied potential is negative than -0.8 V, excited electrons transfer back and recombine with holes, thus oxidation of polypyrrole does not occur. When the potential is positive than 0.8 V, since schottky occurs, charge separation takes place. By comparing E<sub>fb</sub> (flat band potential) of TiO<sub>2</sub> and laser energy, potential of holes could be evaluated. Additionally, since the transfer rate of hole to reaction is slower than recombination, active sites which trapped holes or shift of Fermi level was proposed in this system.<sup>35</sup>

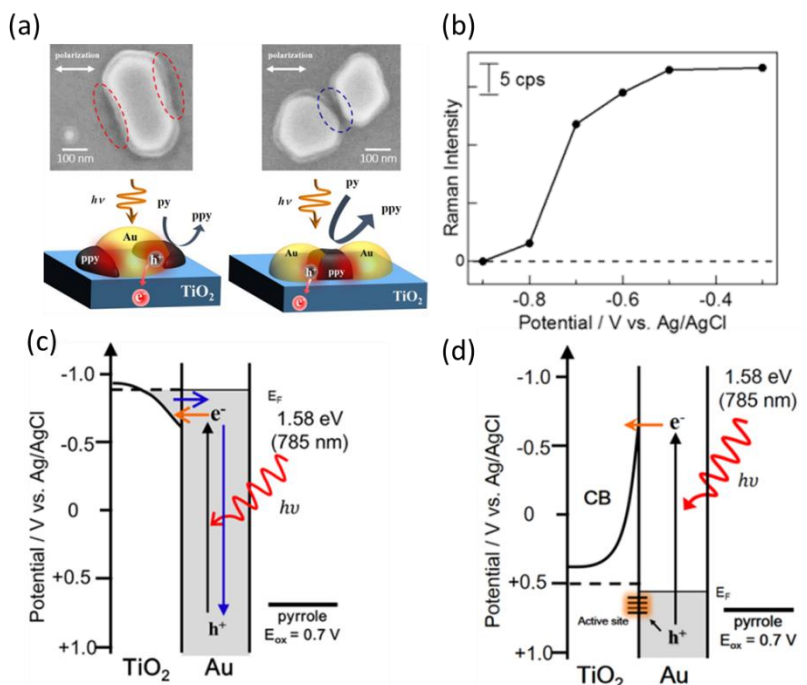


Figure 1.17. (a) SEM and illustrations of plasmonic oxidation polymerization of polypyrrole on Au / TiO<sub>2</sub>. (b) Potential dependent Raman intensity at 1600 cm<sup>-1</sup>(C=C). Energy diagram of plasmonic oxidation polymerization of polypyrrole (c) with an applied energy of 0.5 and (d) with an applied energy of -0.9 V.<sup>35</sup>

#### 1.4.4 Enhancement of water oxidation under modal strong coupling

Plenty of work has been done to optimize the plasmonic photo electron conversation system and most of them exhibit excellent performance. However, there is still room for improvement. One of them is to broaden the available spectra, since most plasmonic system, the absorption peak is rather low.

Shi *et al.* made great achievement in this field. They tuned the energy of LSPR and Fabry-Pérot nanocavity mode with an Au / TiO<sub>2</sub> / Au system and generated modal strong coupling, as Fig. 1.18 shows.<sup>22</sup> Gold film and TiO<sub>2</sub> film was served as nanocavity and Au nanoparticles produce LSPR mode. The hybrid mode enhanced the electronic excitation of Au nanoparticles over a wide range of wavelength, followed by hot electron injection to TiO<sub>2</sub>. An excellent overlap between the optical properties of electrode and IPCE was observed. This work is promising for the effective utilization of solar light.<sup>24</sup> Based on this

work, also under modal strong coupling, Cao *et al.* did some work to reveal the hot electron transfer efficiency on Au film / TiO<sub>2</sub> / Au nanoparticles. Their results indicated that the electron transfer efficiency was enhanced by the electron donor, as shown in Fig.1.19.<sup>36</sup>

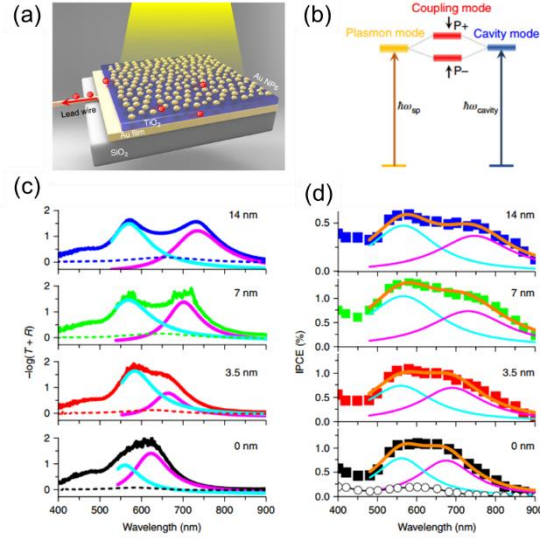


Figure 1. 18. (a) Illustration of the modal strong coupling electrode (Au film / TiO<sub>2</sub> / Au nanoparticles). (b) Energy diagram of the modal strong coupling electrode between the Fabry-Pérot cavity mode and LSPR. (c) Optical spectra of Au film / TiO<sub>2</sub> / Au nanoparticles with different thickness of interlayer. (d) Corresponding IPCE of Au film / TiO<sub>2</sub> / Au nanoparticles.<sup>24</sup>

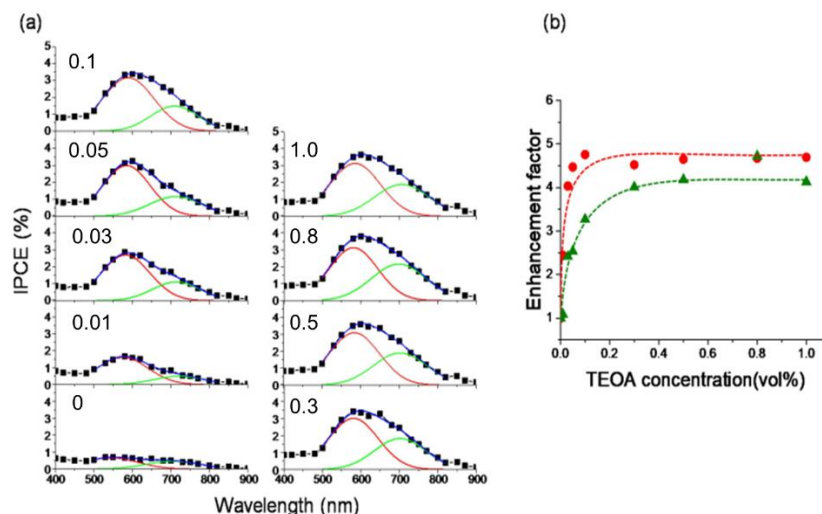


Figure 1.19. (a) IPCE of Au film / TiO<sub>2</sub> / Au nanoparticles with different amount of electron donor. (b) Enhancement factors calculated from IPCE with and without electron donor. Red circles indicate the enhancement factor of the upper branches and green triangles indicate that of the lower branch.<sup>36</sup>

### 1.5 Detecting the fermi level of photocatalysis electrode

Since Fermi level is closely related with the catalysis performance of photoconversion system, it is important to obtain the information about the Fermi level of the plasmonic system for further understanding the charge transfer progress. Some work has been done in this field. As discussed, Cao prepared modal strong coupling system and use electron donor to understand the progress of electron transfer.<sup>36</sup> They also paid attention on the determination of Fermi level shift during the reaction, as Fig. 1.20 shows. By in situ spectroelectrochemical measurements, a shift of lower branch was observed without electron donor, while the shift was restrained with electron donor. When increase the amount of donor, the shift was restrained further. The reason is that the holes not consumed by oxygen evolution reaction, recombined with electrons, leading to the increase of Fermi level. With electron donor, these holes are consumed, reducing the recombination of carriers, thus the shift of Fermi level was also restrained.

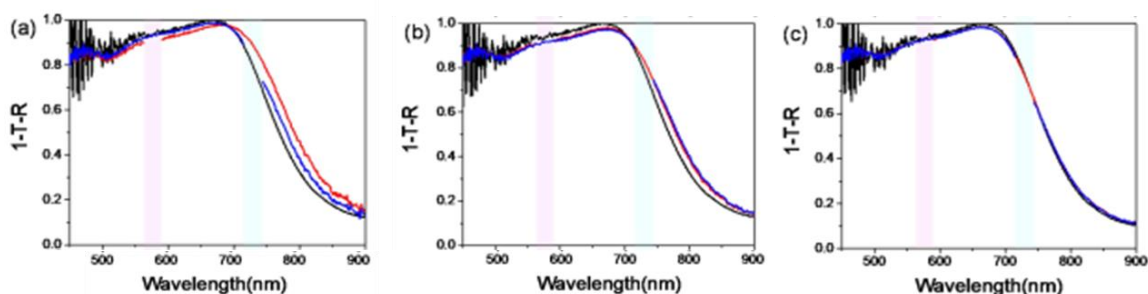


Figure 1.20. Absorption of Au film / TiO<sub>2</sub> / Au nanoparticles in a 1 mol /dm<sup>3</sup> KOH solution at 0.3 V: (a) without electron donor, (b) with 0.01 (c) with 1 vol% electron donor. Blue lines indicate irradiation with 730 nm, red lines indicate the irradiation with 580 nm and black lines indicate no irradiation.<sup>36</sup>

Apart from in situ spectroscopy, Kamat *et al.* made use of the equilibration potential of C<sub>60</sub>/C<sub>60</sub><sup>-</sup> to measure the shift of Fermi level of Au / TiO<sub>2</sub> nanocomposites, as Fig. 1.21 shows. Fermi level was supposed to be dependent quantitatively on the density of C<sub>60</sub>. In their experiment, the formation from C<sub>60</sub><sup>-</sup> to C<sub>60</sub> could be observed by UV absorption and Transient absorption, Fermi level could be calculated from the standard reduction potential of (C<sub>60</sub><sup>-</sup> / C<sub>60</sub>) and the equilibrium concentration of C<sub>60</sub><sup>-</sup> / C<sub>60</sub> and the later could be obtained from the absorption, thus Fermi level could be detected.<sup>37</sup>

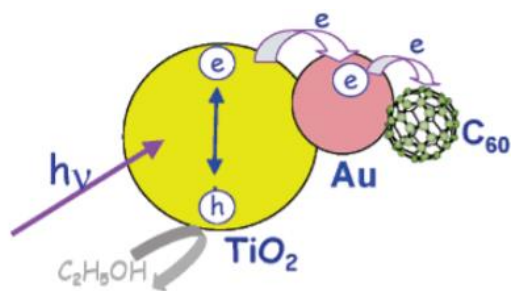


Figure 1.21. Illustration of the charge transfer process of Au / TiO<sub>2</sub> with C<sub>60</sub><sup>-</sup> / C<sub>60</sub>.<sup>37</sup>

Yasuda *et al.* transferred graphene on Au / TiO<sub>2</sub> electrode. Since the properties of G and 2D bands of graphene are dependent on Fermi level of graphene, they adopted

graphene as a detector and obtained the Fermi level of electrode by measuring SERS spectra, as Fig.1.22 indicates.<sup>38</sup>

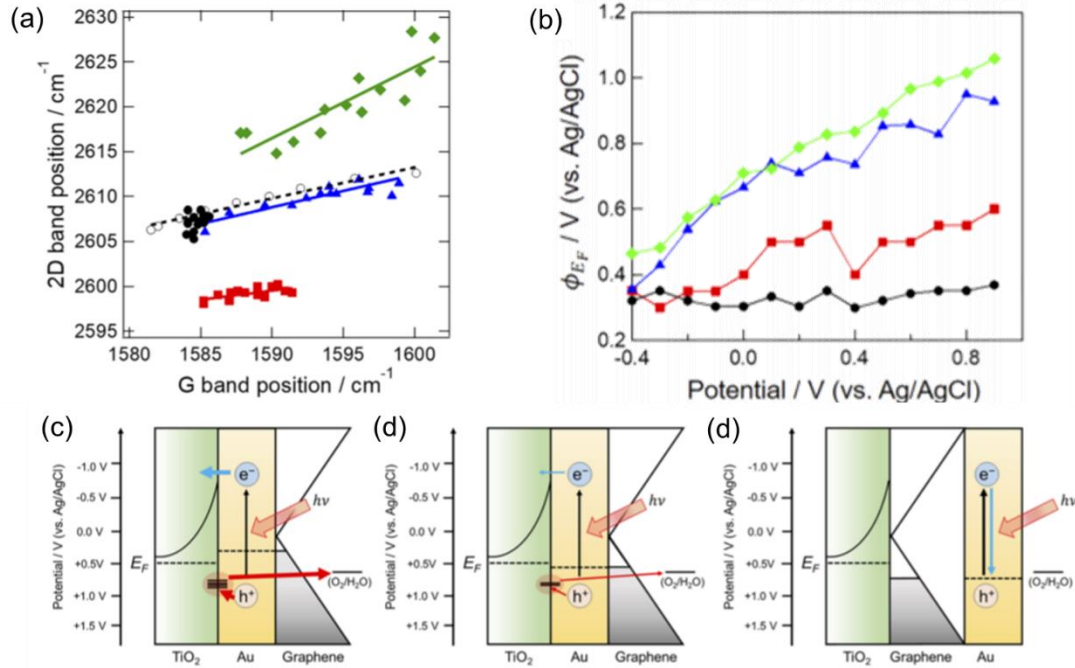


Figure 1.22. (a)  $\omega_G$  vs.  $\omega_{2D}$  at different electrodes (b) Calculated Fermi Level vs. applied potential. The black circle, red square, blue triangle, and green rhombus indicate graphene / TiO<sub>2</sub>, graphene / Au / TiO<sub>2</sub> (with high catalysis performance), graphene / Au / TiO<sub>2</sub> (with low catalysis performance), and Au / graphene / TiO<sub>2</sub>. Energy diagram of (c) Graphene / Au / TiO<sub>2</sub> (with high catalysis performance) (d) Graphene / Au / TiO<sub>2</sub> (with low catalysis performance), and (e) Au / graphene / TiO<sub>2</sub>.<sup>38</sup>

## 1.6 Investigation of oxygen evolution reaction on different catalysis

Oxygen evolution reaction (OER) is very important for solving the energy crisis of the world. Thermodynamically, the standard electrode potential for OER is 1.23 V vs. NHE, indicating that this reaction is difficult to take place. Kinetically, water oxidation involves the transition of multi electrons and protons, leading to the sluggish reaction rate. This proton coupled electron transfer (PCET) may experience of a stepwise mechanism. Such a complicated reaction mechanism hinders the application of OER. Until now, plenty of work has been done to obtain deep insight of OER.



The transition of protons and electrons can be carried out through a stepwise mechanism by forming charged intermediates. Although it is important to consider the actual situation of the reaction, including the probability of electron/proton tunneling effect and the actual solution, etc., usually the order of transfer of protons and electrons can be judged by the relative stability of the intermediate.<sup>39</sup> Proton transfer is closely related to the acid dissociation constant  $Ka$ . When the system undergoes deprotonation,  $pH > pKa$ , on the contrary, the  $pH < pKa$ . Therefore, the standard deprotonation free energy of an acid-base chemical reaction can be expressed as  $\Delta G = 2.303RT \text{ p}Ka$ .

The illustration of PCET is shown in Fig.1.23 for both basic and acidic condition.<sup>40</sup> To achieve concerted proton-electron transfer (CPET), proton and electron transfer must have similar thermochemical or kinetic barriers. In the system, if the  $pKa$  of the active site is comparable to the  $pH$  of the electrolyte, and the proton transfer reaction is easier to perform. Similarly, if the overpotential of the OER is similar to the potential, the electron transfer reaction will proceed easily. For low  $pKa$  (high acidity) reaction site, deprotonation is advantageous and may occur first, especially when the redox potential of the active site inhibits electron transition process. A negatively charged intermediate will be produced. Conversely, in the case of low acidity and low redox potential, electron transfer is more likely to occur, resulting in a positively charged intermediate. In short, in the PCET process, the transfer which has faster kinetics will take place first.

Various researches has been done to prepare high performance catalysis for OER.<sup>41-</sup>  
<sup>44</sup> During the process of developing catalysis, PCET theory is one of the most principle basis. In the study of OER catalysts, Fe, Mn, Co and Ni have been received particularly attention because these metals exhibit promising prospects in the hydrogen evolution reaction (HER) by industrialized water splitting. In addition, the properties of the oxide of these elements are stable, and the specific surface area of the catalyst can be increased by nanocrystallized to increase the activity of the catalyst.<sup>45</sup>



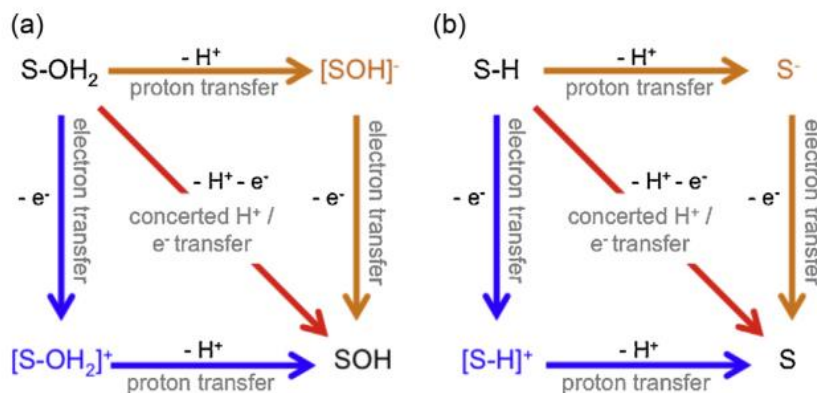
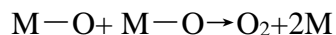
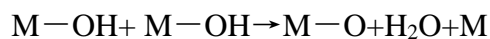
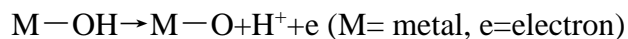


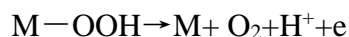
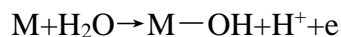
Figure 1.23. Illustration of the proton and electron transfer process during water oxidation in (a) basic condition and (b) acidic condition.<sup>40</sup>

### 1.6.1 Gold catalysis

Gold has been deeply investigated for a long time and it has been proved that gold catalysis exhibits great performance in various field including photocatalysis,<sup>46-47</sup> photo energy conversion<sup>48</sup> or artificial photosynthesis.<sup>49</sup> Usually, the overpotential for water oxidation on the surface of gold catalysis is rather high. According to the previous report, two main reaction pathways have been proposed as follow:<sup>50</sup>



And



Yeo *et al.* reported the first detection of Au-OOH as the intermediates of water oxidation on the surface of gold catalysis. They also proposed that the decomposition of hydroperoxy species on Au was slow thus enable the accumulation of Au-OOH, which

facilitate the observation.<sup>50</sup> Based on this work, Koper *et al.* found that O<sub>2</sub> is produced from two O atoms originated from the surface oxides, indicating the occurrence of decomposition of hydroperoxy species, as Fig. 1.24 shows. Their results indicated that the reaction mechanism of water oxidation was more complicated than expected.<sup>51</sup>

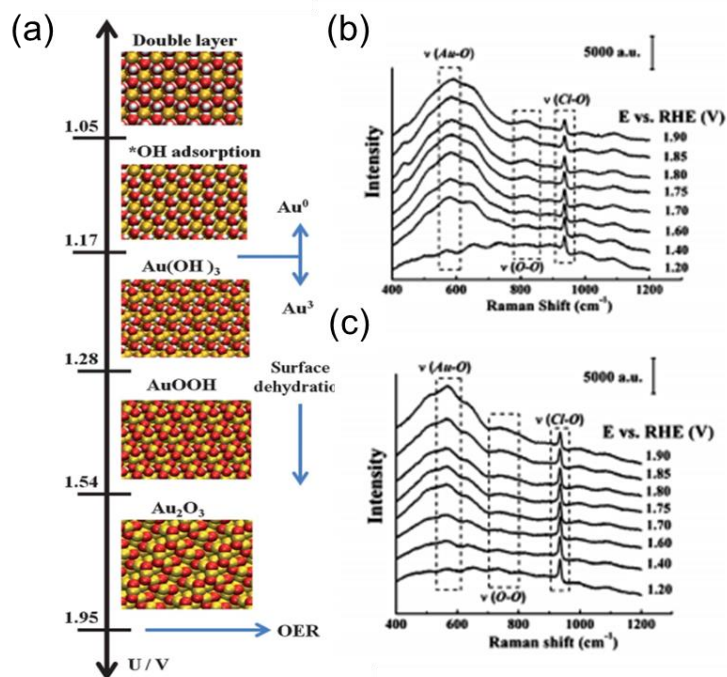


Figure 1.24. (a) illustration of the surface structure of Au catalysis and reaction species for OER at different applied potential. In situ SERS of OER obtained at different constant potential (b) with H<sub>2</sub>O and (c) H<sub>2</sub><sup>18</sup>O.<sup>51</sup>

Tatsuma *et al.* discussed the oxidation ability of gold plasmon on water oxidation with Au / TiO<sub>2</sub> electrode quantitatively.<sup>52</sup> They have proposed the dependence of the electrochemical potential of Au surface on pH values using Pourbaix diagram as shown in Fig. 1.25. Although they referred to the importance of the photon energy for the chemical reactions, the experimental observation of the intermediate species on the plasmonic metal surface is still difficult to be achieved.

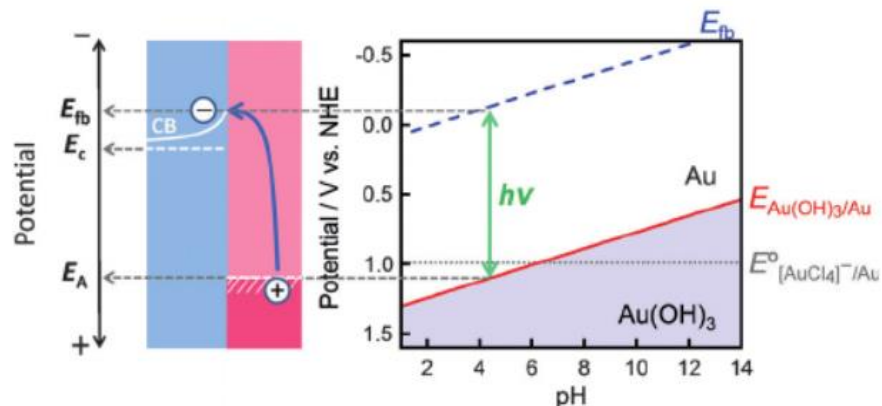


Figure 1.25. charge transfer process of Au / TiO<sub>2</sub> system and the Pourbaix diagram of Au-H<sub>2</sub>O system.<sup>52</sup>

### 1.6.2 Mn, Fe and Co catalysis

Manganese oxides have also received considerable attention for the catalysis of water oxidation since 1977.<sup>53</sup> Plenty of work has been done to synthesize high-performance Mn catalysis. Frei<sup>45</sup> prepared high-performance Mn catalysis dispersed on porous silicon support for OER in weak acidic condition. It provided high surface area for the dispersion and stable the active site of Mn, which contributed to the high catalysis performance. Stahl reported a comprehensive study of different kinds of crystalline MnO<sub>x</sub> materials as water oxidation catalysis and discovered that the characteristic of the catalysis with highest performance.<sup>54</sup> Dau improved the catalysis performance of Mn catalysis for OER by control the potential.<sup>55</sup> According to their research, the voltage-cycling protocol can modify the nano structure of Mn oxide thus improve the catalysis performance. It was better than the materials prepared by electrodepositing at constant potential, which is the reason for the high catalysis performance. Although synthesize high performance material is important, the lack of the detailed mechanism of this catalysis system prohibit the further optimization.

Nakamura did some work to expound the reaction mechanism of OER on MnO<sub>2</sub>, as Fig. 1.26 shows.<sup>56</sup> They found that Mn(III) is active for OER. They also revealed the reason why Mn catalysis is only effective in basic condition: the comproportionating of Mn(II) and Mn(IV) to Mn(III) take place in basic condition, which reduce the overpotential. Based

on this research, they further detected the limitation of stability of Mn(III) and within this limitation, Mn catalysis showed an excellent performance of 8000 h.

Although Nakamura found the none Faradaic pH dependence, at that time they did not expound this dependence clearly. Later they did some work to understand this unique phenomenon.<sup>41</sup> They found that the independence of pH in acidic and neutral condition is due to the redox change from  $\text{Mn}^{2+}$  to  $\text{Mn}^{3+}$  forced the unchanged of overpotential. They invoked the CPET mechanism by adding proton acceptor with pKa between the reactant and transition state and reduced the overpotential in the neutral region successfully, as Fig. 1.27 shows.

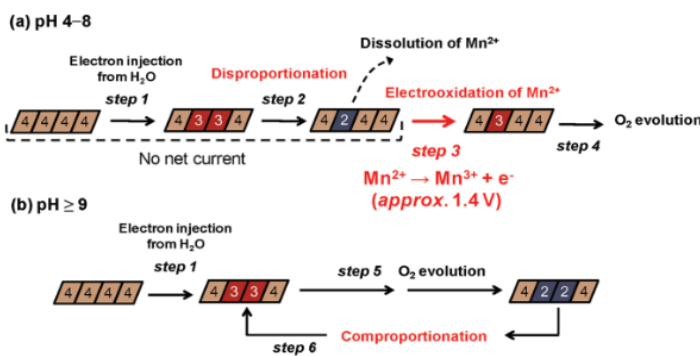


Figure 1.26. Evolution of the redox state of Mn catalysis for OER at (a) acidic and neutral conditions and (b) basic condition.<sup>56</sup>

Nocera also did some work on the PCET and disproportionation of Mn oxide, and proposed the illustration of OER mechanism on Mn oxide.<sup>57</sup> According to his results, a minor equilibrium of  $2e^- - 2\text{H}^+$  was needed during  $\text{MnO}_x$  catalytic oxidation. After that,  $\text{Mn}^{2+}$  could be chemically oxidized in the later PCET process. However, the pKa to invoke PCET process is lower than that of disproportionation, thus catalytic activity for water oxidation in  $\text{MnO}_x$  film is dominated by disproportionation. Therefore, it is important for more efficient Mn oxygen evolution catalyst to control disproportionation as well as PCET process.

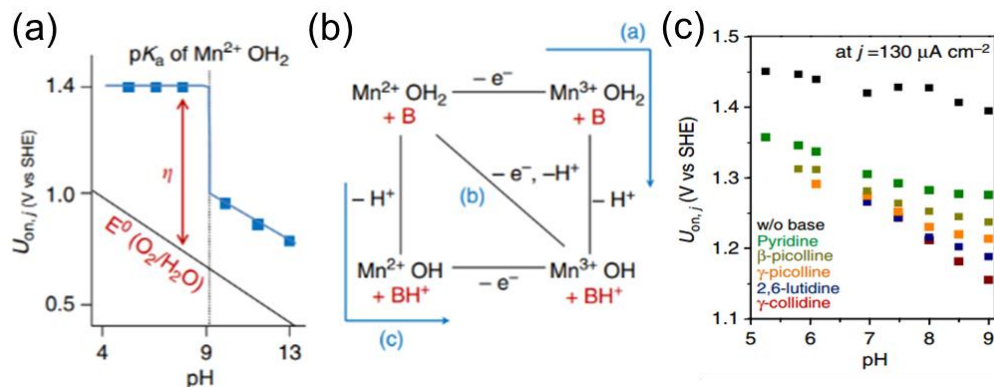


Figure 1.27. (a) onset potential vs. pH of Mn catalysis for OER. (b) proton-electron transition pathways of OER on Mn catalysis. (c) onset potential vs. pH with proton acceptors with different  $pK_a$ .<sup>41</sup>

Iron oxide materials for water oxidation have been deeply studied because it is abundant on the earth. Meyer and his coworkers using a Monomeric Amidate-Ligated Fe(III)–Aqua Complex to study the electrocatalysis of water oxidation, as Fig. 1.28 shows.<sup>42</sup> By kinetics study, they found that Fe(IV) is the active catalysis state for OER. Hiroshi using  $La_2O_3$  as a proton acceptor and successfully induced the concerted proton-electron transfer (CPET) by which enhanced the catalysis performance.<sup>43</sup> They found without  $La_2O_3$ , the onset potential of OER showed unique pH-dependence. When the pH is lower than 10, the on-set potential remain unchanged while in the region of  $pH > 10$ , it shows pH dependence. This phenomenon is due to PCET. Since the  $pK_a$  of  $\alpha-Fe_2O_3$  ( $Fe^{III}-OH$ ) is reported as 10 and that of  $Fe^{IV}=O$  can be adopted as 4. By adding proton acceptor with a  $pK_a$  within 4~10, CPET could be induced, as Fig. 1.30 shows.

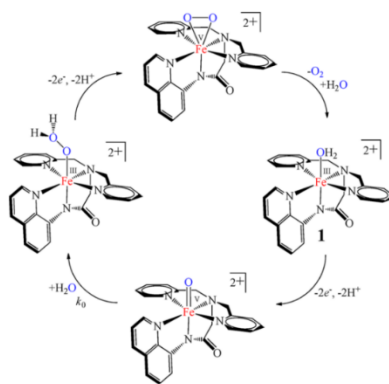


Figure 1.28. Reaction pathway of OER catalyzed by  $[\text{Fe}^{\text{III}}(\text{dpaq})(\text{H}_2\text{O})](\text{ClO}_4)_2$ .<sup>42</sup>

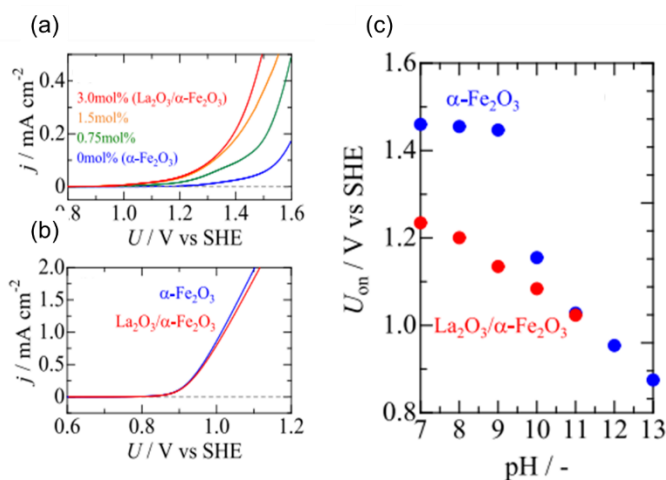
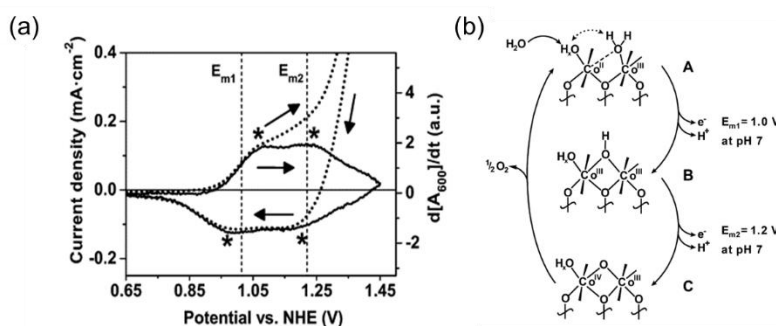
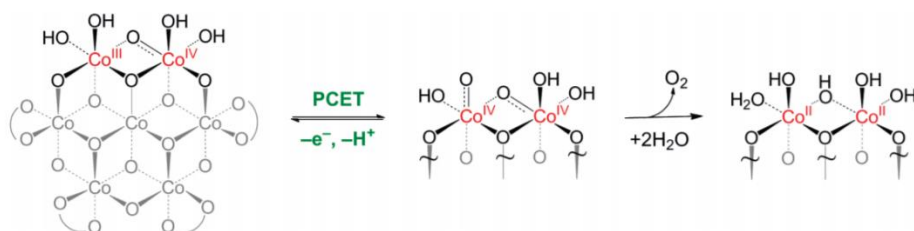


Figure 1.29. Polarization curves with different amount of  $\text{La}_2\text{O}_3$  as proton acceptor at (a) pH 7 and (b) pH 13. (c) the onset potential for OER at different pH. Blue circles indicate the system without  $\text{La}_2\text{O}_3$  and red circles indicate the system with  $\text{La}_2\text{O}_3$ .<sup>43</sup>

Cobalt and its oxides have been investigated extensively. There are several characteristics of Co catalysis: 1.  $\text{Co}^{\text{III/IV}}$  mixed valence clusters is considered as a catalyst resting state.<sup>58</sup> 2. The change of oxide state of Co goes through the process of releasing proton to the electrolyte and indicates that the O-O bond formation is the turnover limiting step according to previous research.<sup>58-59</sup> 3. The Co catalysis usually consists of 14-19 Co atom and the catalysis of water oxidation usually occurs in the bulk, at the edge of the  $\text{CoO}_x$  fragments<sup>60-61</sup>. There is several mechanism research on the reaction mechanism of OER on

Co catalysis. Nocera and his collaborators suggests that a one-electron, one-proton equilibrium step takes place in the turnover-limiting step in water oxidation on Co-Pi catalysis as Fig. 1.31 shows.<sup>58</sup> The phosphate electrolyte plays the essential role of maintaining this PCET equilibrium by facilitating rapid proton transfer. Marcel and his coworkers investigated changes of structures of Co film and found that dioxygen could be generated benefiting from the accumulation of oxidizing equivalents, as Fig. 1.32 shows.<sup>62</sup> They also proposed new framework of catalysis: reversible change of the oxidation states between  $\text{Co}^{\text{II}}$  /  $\text{Co}^{\text{III}}$  /  $\text{Co}^{\text{IV}}$  took place during water oxidation, accompanied with changing and deprotonating Co-oxo bridge.



### 1.6.3 Nickel catalysis

When immersed in electrolyte, Ni will be oxidized immediately to form  $\alpha$ -Ni(OH)<sub>2</sub>, which will transform to  $\beta$ -Ni(OH)<sub>2</sub> due to aging. After charge transferring,  $\beta$ -NiOOH as peroxide of OER will be generated and then produce oxygen, producing  $\alpha$ -Ni(OH)<sub>2</sub> to repeat this cycle.<sup>63</sup>

In order to determine the type of Ni hydroxide which shows better performance, Srinivasan did some work and found the  $\beta$ -Ni(OH)<sub>2</sub> is better for the water oxidation. Boettcher found that addition of iron can enhance catalytic activity greatly even for accidental addition of Fe.<sup>64</sup> However, it increases the complexity of the problem. For the reaction mechanism of water oxidation on Ni surface, Koper *et al.* conducted electrochemical reaction of water oxidation at different pH, they found that the performance increased as the solution became more basic. They proposed that a deprotonation step was involved in the reaction mechanism. By spectroscopic method, they also demonstrated that superoxide was the intermediate species of water oxidation. The reaction mechanism of OER on nickel catalysis is shown in Fig.1.33.<sup>65</sup>

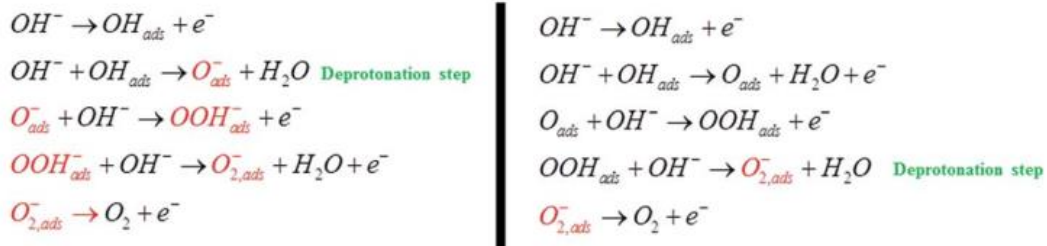


Figure 1.32. Proposed reaction mechanism of Ni(OH)<sub>2</sub> / Au for OER.<sup>65</sup>

## 1.7 Problems and target of our research

According to the above discussion, I may summarize that there are still unclear points in the multiple electron transfer process at the plasmonic field. According to the above discussion, there still remain great space to improve in the field of plasmon induced electron transfer process. One is the photon confinement of plasmon induced chemical reactions is still a challenging issue, the second is that the electronic structure at the metal-semiconductor interface is still unclear, and the third is the electron transfer process needs to be understood for further optimization. Based on these problems, the targets of my thesis is to improve the collection and localization of photons to enhance chemical reactions. It



includes three aspects: to clarify the electronic structure of plasmonic electrode; to optimize the system to localize photon energy for chemical reactions and to control the plasmon induced reaction activity.

## 1.8 Objective and outline of this thesis

The aim of this study is to expound the electronic properties of plasmonic electrode and the unique influence of plasmon on the reaction mechanism on the multiple electron transfer process accelerated by plasmon excitation. Chapter 1 gives the general introduction on the basic concept of plasmon, electrocatalysis of OER and application of plasmonic electrode on chemical reaction. Chapter 2 shows the effective utilization of solar light over wide wavelength by Ag / MoS<sub>2</sub> plasmonic strong coupling system. Chapter 3 reveal the unique catalysis performance of OER with Au / TiO<sub>2</sub> system. Chapter 4 shows the determination of Fermi level for novel plasmonic electrode by attaching graphene as a detector. Chapter 5 discusses the novel catalysis performance of nickel for OER with plasmon by isotope effect. Chapter 6 summarize the general conclusion.

## References

1. Hagfeldt, A.; Grätzel, M., Molecular Photovoltaics. *Acc. Chem. Res.* **2000**, *33* (5), 269-277.
2. Esswein, A. J.; Nocera, D. G., Hydrogen Production by Molecular Photocatalysis. *Chem. Rev.* **2007**, *107* (10), 4022-4047.
3. Oelgemöller, M.; Jung, C.; Ortner, J.; Mattay, J.; Zimmermann, E., Green Photochemistry: Solar Photooxygenations with Medium Concentrated Sunlight. *Green Chem.* **2005**, *7* (1), 35-38.
4. Ciamician, G., The Photochemistry of the Future. *Science* **1912**, *36* (926), 385-394.
5. Manassen, J.; Cahen, D.; Hodes, G.; Sofer, A., Electrochemical, Solid State, Photochemical and Technological Aspects of Photoelectrochemical Energy Converters. *Nature* **1976**, *263* (5573), 97-100.
6. Linic, S.; Christopher, P.; Ingram, D. B., Plasmonic-Metal Nanostructures for Efficient Conversion of Solar to Chemical Energy. *Nat. Mater.* **2011**, *10* (12), 911-921.

7. Mayer, K. M.; Hafner, J. H., Localized Surface Plasmon Resonance Sensors. *Chem. Rev.* **2011**, *111* (6), 3828-3857.
8. Willets, K. A.; Van Duyne, R. P., Localized Surface Plasmon Resonance Spectroscopy and Sensing. *Annu. Rev. Phys. Chem.* **2007**, *58*, 267-297.
9. Jain, P. K.; El-Sayed, M. A., Plasmonic Coupling in Noble Metal Nanostructures. *Chem. Phys. Lett.* **2010**, *487* (4-6), 153-164.
10. Hammond, J. L.; Bhalla, N.; Rafiee, S. D.; Estrela, P., Localized Surface Plasmon Resonance as a Biosensing Platform for Developing Countries. *Biosensors* **2014**, *4* (2), 172-188.
11. Zhang, X.; Chen, Y. L.; Liu, R. S.; Tsai, D. P., Plasmonic Photocatalysis. *Rep. Prog. Phys.* **2013**, *76* (4), 046401.
12. Jain, P. K.; Lee, K. S.; El-Sayed, I. H.; El-Sayed, M. A., Calculated Absorption and Scattering Properties of Gold Nanoparticles of Different Size, Shape, and Composition: Applications in Biological Imaging and Biomedicine. *J. Phys. Chem. B* **2006**, *110* (14), 7238-7248.
13. Link, S.; Wang, Z. L.; El-Sayed, M., Alloy Formation of Gold-Silver Nanoparticles and the Dependence of the Plasmon Absorption on Their Composition. *J. Phys. Chem. B* **1999**, *103* (18), 3529-3533.
14. Sönnichsen, C.; Franzl, T.; Wilk, T.; Von Plessen, G.; Feldmann, J.; Wilson, O.; Mulvaney, P., Drastic Reduction of Plasmon Damping in Gold Nanorods. *Phys. Rev. Lett.* **2002**, *88* (7), 077402.
15. Ueno, K.; Oshikiri, T.; Sun, Q.; Shi, X.; Misawa, H., Solid-State Plasmonic Solar Cells. *Chem. Rev.* **2017**, *118* (6), 2955-2993.
16. Bellessa, J.; Bonnand, C.; Plenet, J.; Mugnier, J., Strong Coupling between Surface Plasmons and Excitons in an Organic Semiconductor. *Phys. Rev. Lett.* **2004**, *93* (3), 036404.
17. Tse, E. C.; Hoang, T. T.; Varnell, J. A.; Gewirth, A. A., Observation of an Inverse Kinetic Isotope Effect in Oxygen Evolution Electrochemistry. *ACS Catal.* **2016**, *6* (9), 5706-5714.
18. Wen, J.; Wang, H.; Wang, W.; Deng, Z.; Zhuang, C.; Zhang, Y.; Liu, F.; She, J.; Chen, J.; Chen, H., Room-Temperature Strong Light–Matter Interaction with Active

Control in Single Plasmonic Nanorod Coupled with Two-Dimensional Atomic Crystals. *Nano Lett.* **2017**, *17* (8), 4689-4697.

19. Nagasawa, F.; Takase, M.; Murakoshi, K., Raman Enhancement Via Polariton States Produced by Strong Coupling between a Localized Surface Plasmon and Dye Excitons at Metal Nanogaps. *J. Phys. Chem. Lett.* **2014**, *5* (1), 14-19.

20. Kato, F.; Minamimoto, H.; Nagasawa, F.; Yamamoto, Y. S.; Itoh, T.; Murakoshi, K., Active Tuning of Strong Coupling States between Dye Excitons and Localized Surface Plasmons Via Electrochemical Potential Control. *ACS Photonics* **2018**, *5* (3), 788-796.

21. Gramotnev, D. K.; Bozhevolnyi, S. I., Plasmonics Beyond the Diffraction Limit. *Nature photonics* **2010**, *4* (2), 83.

22. Le Ru, E.; Etchegoin, P., Elsevier: 2008.

23. Bellessa, J.; Symonds, C.; Vynck, K.; Lemaitre, A.; Brioude, A.; Beaur, L.; Plenet, J.; Viste, P.; Felbacq, D.; Cambril, E., Giant Rabi Splitting between Localized Mixed Plasmon-Exciton States in a Two-Dimensional Array of Nanosize Metallic Disks in an Organic Semiconductor. *Phys. Rev. B* **2009**, *80* (3), 033303.

24. Shi, X.; Ueno, K.; Oshikiri, T.; Sun, Q.; Sasaki, K.; Misawa, H., Enhanced Water Splitting under Modal Strong Coupling Conditions. *Nat. Nanotechnol.* **2018**, *13* (10), 953-958.

25. Okazaki, M.; Suganami, Y.; Hirayama, N.; Nakata, H.; Oshikiri, T.; Yokoi, T.; Misawa, H.; Maeda, K., Site-Selective Deposition of a Cobalt Cocatalyst onto a Plasmonic Au/TiO<sub>2</sub> Photoanode for Improved Water Oxidation. *ACS Appl. Energy Mater.* **2020**.

26. Zhong, Y.; Ueno, K.; Mori, Y.; Shi, X.; Oshikiri, T.; Murakoshi, K.; Inoue, H.; Misawa, H., Plasmon-Assisted Water Splitting Using Two Sides of the Same SrTiO<sub>3</sub> Single-Crystal Substrate: Conversion of Visible Light to Chemical Energy. *Angew. Chem. Int. Ed.* **2014**, *53* (39), 10350-10354.

27. Tian, Y.; Tatsuma, T., Mechanisms and Applications of Plasmon-Induced Charge Separation at TiO<sub>2</sub> Films Loaded with Gold Nanoparticles. *J. Am. Chem. Soc.* **2005**, *127* (20), 7632-7637.

28. Tian, Y.; Tatsuma, T., Plasmon-Induced Photoelectrochemistry at Metal Nanoparticles Supported on Nanoporous TiO<sub>2</sub>. *Chem. Commun.* **2004**, (16), 1810-1811.

29. Boerigter, C.; Aslam, U.; Linic, S., Mechanism of Charge Transfer from Plasmonic Nanostructures to Chemically Attached Materials. *ACS nano* **2016**, *10* (6), 6108-6115.
30. Wu, K.; Chen, J.; McBride, J. R.; Lian, T., Efficient Hot-Electron Transfer by a Plasmon-Induced Interfacial Charge-Transfer Transition. *Science* **2015**, *349* (6248), 632-635.
31. Uskov, A. V.; Protsenko, I. E.; Ikhsanov, R. S.; Babicheva, V. E.; Zhukovsky, S. V.; Lavrinenko, A. V.; O'reilly, E. P.; Xu, H., Internal Photoemission from Plasmonic Nanoparticles: Comparison between Surface and Volume Photoelectric Effects. *Nanoscale* **2014**, *6* (9), 4716-4727.
32. Hou, W.; Cronin, S. B., A Review of Surface Plasmon Resonance-Enhanced Photocatalysis. *Adv. Funct. Mater.* **2013**, *23* (13), 1612-1619.
33. Kogo, A.; Takahashi, Y.; Sakai, N.; Tatsuma, T., Gold Cluster-Nanoparticle Diad Systems for Plasmonic Enhancement of Photosensitization. *Nanoscale* **2013**, *5* (17), 7855-7860.
34. Tatsuma, T.; Nishi, H.; Ishida, T., Plasmon-Induced Charge Separation: Chemistry and Wide Applications. *Chem. Sci.* **2017**, *8* (5), 3325-3337.
35. Minamimoto, H.; Toda, T.; Futashima, R.; Li, X.; Suzuki, K.; Yasuda, S.; Murakoshi, K., Visualization of Active Sites for Plasmon-Induced Electron Transfer Reactions Using Photoelectrochemical Polymerization of Pyrrole. *J. Phys. Chem. C* **2016**, *120* (29), 16051-16058.
36. Cao, Y.; Oshikiri, T.; Shi, X.; Ueno, K.; Li, J.; Misawa, H., Efficient Hot-Electron Transfer under Modal Strong Coupling Conditions with Sacrificial Electron Donors. *ChemNanoMat* **2019**, *5* (8), 1008-1014.
37. Subramanian, V.; Wolf, E. E.; Kamat, P. V., Catalysis with TiO<sub>2</sub>/Gold Nanocomposites. Effect of Metal Particle Size on the Fermi Level Equilibration. *J. Am. Chem. Soc.* **2004**, *126* (15), 4943-4950.
38. Minamimoto, H.; Yasuda, K.; Zhou, R.; Li, X.; Yasuda, S.; Murakoshi, K., Potential Energy Shift of the Fermi Level at Plasmonic Structures for Light-Energy Conversion Determined by Graphene-Based Raman Measurements. *J. Chem. Phys.* **2020**, *152* (12), 124702.

39. Koper, M. T., Theory of Multiple Proton–Electron Transfer Reactions and Its Implications for Electrocatalysis. *Chem. Sci.* **2013**, *4* (7), 2710-2723.
40. Giordano, L.; Han, B.; Risch, M.; Hong, W. T.; Rao, R. R.; Stoerzinger, K. A.; Shao-Horn, Y., pH Dependence of OER Activity of Oxides: Current and Future Perspectives. *Catal. Today* **2016**, *262*, 2-10.
41. Yamaguchi, A.; Inuzuka, R.; Takashima, T.; Hayashi, T.; Hashimoto, K.; Nakamura, R., Regulating Proton-Coupled Electron Transfer for Efficient Water Splitting by Manganese Oxides at Neutral Ph. *Nat. Commun.* **2014**, *5* (1), 1-6.
42. Coggins, M. K.; Zhang, M.-T.; Vannucci, A. K.; Dares, C. J.; Meyer, T. J., Electrocatalytic Water Oxidation by a Monomeric Amidate-Ligated Fe (III)–Aqua Complex. *J. Am. Chem. Soc.* **2014**, *136* (15), 5531-5534.
43. Takashima, T.; Ishikawa, K.; Irie, H., Induction of Concerted Proton-Coupled Electron Transfer During Oxygen Evolution on Hematite Using Lanthanum Oxide as a Solid Proton Acceptor. *ACS Catal.* **2019**, *9* (10), 9212-9215.
44. Koepke, S. J.; Light, K. M.; Vannatta, P. E.; Wiley, K. M.; Kieber-Emmons, M. T., Electrocatalytic Water Oxidation by a Homogeneous Copper Catalyst Disfavors Single-Site Mechanisms. *J. Am. Chem. Soc.* **2017**, *139* (25), 8586-8600.
45. Jiao, F.; Frei, H., Nanostructured Manganese Oxide Clusters Supported on Mesoporous Silica as Efficient Oxygen-Evolving Catalysts. *Chem. Commun.* **2010**, *46* (17), 2920-2922.
46. Ding, D.; Liu, K.; He, S.; Gao, C.; Yin, Y., Ligand-Exchange Assisted Formation of Au/TiO<sub>2</sub> Schottky Contact for Visible-Light Photocatalysis. *Nano Lett.* **2014**, *14* (11), 6731-6736.
47. Moon, S. Y.; Song, H. C.; Gwag, E. H.; Nedrygailov, I. I.; Lee, C.; Kim, J. J.; Doh, W. H.; Park, J. Y., Plasmonic Hot Carrier-Driven Oxygen Evolution Reaction on Au Nanoparticles/TiO<sub>2</sub> Nanotube Arrays. *Nanoscale* **2018**, *10* (47), 22180-22188.
48. Boriskina, S. V.; Zhou, J.; Hsu, W. C.; Liao, B.; Chen, G. In Limiting Efficiencies of Solar Energy Conversion and Photo-Detection via Internal Emission of Hot Electrons and Hot Holes in Gold, Infrared Remote Sensing and Instrumentation XXIII, International Society for Optics and Photonics: 2015; p 960816.

49. Ueno, K.; Oshikiri, T.; Shi, X.; Zhong, Y.; Misawa, H., Plasmon-Induced Artificial Photosynthesis. *Interface Focus* **2015**, *5* (3), 20140082.
50. Yeo, B. S.; Klaus, S. L.; Ross, P. N.; Mathies, R. A.; Bell, A. T., Identification of Hydroperoxy Species as Reaction Intermediates in the Electrochemical Evolution of Oxygen on Gold. *ChemPhysChem* **2010**, *11* (9), 1854-1857.
51. Diaz-Morales, O.; Calle-Vallejo, F.; De Munck, C.; Koper, M. T., Electrochemical Water Splitting by Gold: Evidence for an Oxide Decomposition Mechanism. *Chem. Sci.* **2013**, *4* (6), 2334-2343.
52. Nishi, H.; Tatsuma, T., Oxidation Ability of Plasmon-Induced Charge Separation Evaluated on the Basis of Surface Hydroxylation of Gold Nanoparticles. *Angew. Chem. Int. Ed.* **2016**, *55* (36), 10771-10775.
53. Morita, M.; Iwakura, C.; Tamura, H., The Anodic Characteristics of Manganese Dioxide Electrodes Prepared by Thermal Decomposition of Manganese Nitrate. *Electrochem. Acta* **1977**, *22* (4), 325-328.
54. Pokhrel, R.; Goetz, M. K.; Shaner, S. E.; Wu, X.; Stahl, S. S., The “Best Catalyst” for Water Oxidation Depends on the Oxidation Method Employed: A Case Study of Manganese Oxides. *J. Am. Chem. Soc.* **2015**, *137* (26), 8384-8387.
55. Zaharieva, I.; Chernev, P.; Risch, M.; Klingan, K.; Kohlhoff, M.; Fischer, A.; Dau, H., Electrosynthesis, Functional, and Structural Characterization of a Water-Oxidizing Manganese Oxide. *Energy & Environ. Sci.* **2012**, *5* (5), 7081-7089.
56. Takashima, T.; Hashimoto, K.; Nakamura, R., Mechanisms of Ph-Dependent Activity for Water Oxidation to Molecular Oxygen by MnO<sub>2</sub> Electrocatalysts. *J. Am. Chem. Soc.* **2012**, *134* (3), 1519-1527.
57. Huynh, M.; Bediako, D. K.; Liu, Y.; Nocera, D. G., Nucleation and Growth Mechanisms of an Electrodeposited Manganese Oxide Oxygen Evolution Catalyst. *J. Phys. Chem. C* **2014**, *118* (30), 17142-17152.
58. Surendranath, Y.; Kanan, M. W.; Nocera, D. G., Mechanistic Studies of the Oxygen Evolution Reaction by a Cobalt-Phosphate Catalyst at Neutral Ph. *J. Am. Chem. Soc.* **2010**, *132* (46), 16501-16509.

59. Mattioli, G.; Giannozzi, P.; Amore Bonapasta, A.; Guidoni, L., Reaction Pathways for Oxygen Evolution Promoted by Cobalt Catalyst. *J. Am. Chem. Soc.* **2013**, *135* (41), 15353-15363.
60. Du, P.; Kokhan, O.; Chapman, K. W.; Chupas, P. J.; Tiede, D. M., Elucidating the Domain Structure of the Cobalt Oxide Water Splitting Catalyst by X-Ray Pair Distribution Function Analysis. *J. Am. Chem. Soc.* **2012**, *134* (27), 11096-11099.
61. Farrow, C. L.; Bediako, D. K.; Surendranath, Y.; Nocera, D. G.; Billinge, S. J., Intermediate-Range Structure of Self-Assembled Cobalt-Based Oxygen-Evolving Catalyst. *J. Am. Chem. Soc.* **2013**, *135* (17), 6403-6406.
62. Risch, M.; Ringleb, F.; Kohlhoff, M.; Bogdanoff, P.; Chernev, P.; Zaharieva, I.; Dau, H., Water Oxidation by Amorphous Cobalt-Based Oxides: In Situ Tracking of Redox Transitions and Mode of Catalysis. *Energy & Environ. Sci.* **2015**, *8* (2), 661-674.
63. Bode, H., K, Dehmelt, and J. Witte. *Electrochim. Acta* **1966**, *11*, 1079.
64. Trotochaud, L.; Young, S. L.; Ranney, J. K.; Boettcher, S. W., Nickel–Iron Oxyhydroxide Oxygen-Evolution Electrocatalysts: The Role of Intentional and Incidental Iron Incorporation. *J. Am. Chem. Soc.* **2014**, *136* (18), 6744-6753.
65. Diaz-Morales, O.; Ferrus-Suspedra, D.; Koper, M. T., The Importance of Nickel Oxyhydroxide Deprotonation on Its Activity Towards Electrochemical Water Oxidation. *Chem. Sci.* **2016**, *7* (4), 2639-2645.

## Chapter 2.

# Active tuning the strong coupling state between Ag/MoS<sub>2</sub> heterostructure via electrochemical method

---

## 2.1 Introduction

As has been introduced in Chapter 1, strong coupling is proved to be the promising solution for the utilization of light with wide wavelength. Since plasmon has the ultra-small mode volume, it would be suitable for serving as the cavity for strong coupling regime.<sup>1</sup> With brilliant photoelectronic properties, molybdenum disulfide (MoS<sub>2</sub>) has been capturing dramatic attention during the past decade and has been widely applied in many fields such as photodetection, light harvesting, phototransistors, and lasers.<sup>2-6</sup> MoS<sub>2</sub> shows layer-dependent properties which provides us with new insight to probe into its optoelectronic application. First, it shifts from indirect semiconductor to direct one when the thickness of it is down to single layer as in Fig.2.1 (a) and (b).<sup>7</sup> Although the direct semiconductor absorb or emit a photon with higher energy than the band gap, the indirect semiconductor needs an extra phonon, resulting in the lower efficiency of photon absorption. For bulk MoS<sub>2</sub>, the band gap is about 1.2 eV while the band gap reaches to 1.9 eV when thinned down to monolayer.<sup>6</sup> The reason why the band structure changes with layer number is attribute to the quantum confinement and the resulting change in hybridization between  $p_z$  orbitals on S atoms and  $d$  orbitals on Mo atoms.<sup>6</sup> For the effective use of the MoS<sub>2</sub> in the photovoltaic devices, the enhancement of the interaction between the light energy and MoS<sub>2</sub> would be important. The confinement of light energy into nanoscale would be one of great way to improve the interaction between them. With this aim, the plenty works stress the importance the usage of two dimensional material such as (hBN), or MoS<sub>2</sub> in the strong coupling regime.<sup>8-10</sup> Especially for MoS<sub>2</sub> case, because the dipole moment of MoS<sub>2</sub> increase as the layer number decreases as in Fig. 2.1 (c), the effective confinement of light energy in the vicinity of MoS<sub>2</sub> seems to be innovative as reported in Klein and his co-workers work.<sup>11</sup> Since the coupling strength is proportional to  $d^{1/2}$ , it is significant to investigate strong coupling with multi-layer MoS<sub>2</sub>. MoS<sub>2</sub> has large exciton binding energy and dipole moment, which enable it as suitable candidate for the achievement of strong coupling. Fourth, the Raman shift will change according to the variation of layer numbers,



that is, the difference between  $E_{2g}^1$  and  $A_{1g}$  will decrease as the layer number decrease<sup>12</sup>, see Fig.2.1 (d) and the relationship between the peak position and the layer numbers is shown in Fig.2.1 (e). This property provides the method to determine the layer number of MoS<sub>2</sub> especially for the relative thin samples. However, for MoS<sub>2</sub> with layer number larger than 10, it is difficult to determine the specific layer number by means of Raman since the difference is not obvious. Fifth, MoS<sub>2</sub> shows strong exciton effect. Due to the spin-splitting effect of valence band, two peaks can be seen in the absorption spectrum, known as A exciton and B exciton, with energies of ~1.92 eV and ~2.08eV respectively, see Fig. 2.1 (d).<sup>13</sup>

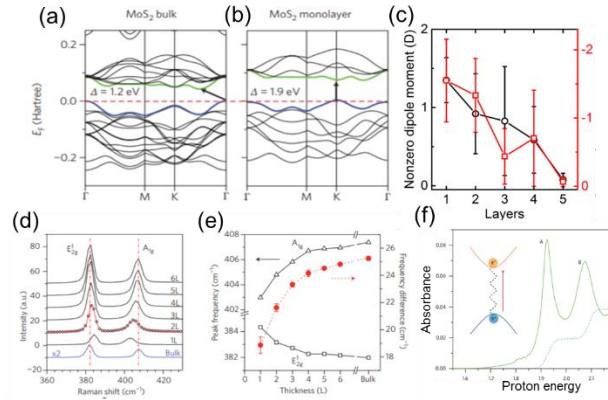


Figure 2.1. (a) and (b) Band structures for bulk and monolayer MoS<sub>2</sub>. (c) Mean values of the exciton dipole moment as a function of layer number. (d) Thickness-dependent Raman spectra for MoS<sub>2</sub>. (e) Peak position shifts for the  $E_{2g}$  and  $A_{1g}$  modes as a function of MoS<sub>2</sub>. (f) Absorbance of MoS<sub>2</sub>.

Although there are various results about the strong coupling, the active tuning of the strong coupling state is still a challenging issue.

In this study, I have tried to establish the electrochemically-tunable strong coupling state between the thin MoS<sub>2</sub> layer and plasmonic cavity generated by Ag nanoparticles. I have successfully controlled the strong coupling state by the tuning of the localized surface plasmon resonance energy via the electrochemical potential control. In addition, I have also confirmed the layer number dependence of MoS<sub>2</sub> layer on the strong coupling strength.

## 2.2 Experimental

### 2.2.1 Cleaning the indium tin oxide (ITO) substrate

ITO glass was cleaned ultrasonically with trichloromethane for 10 min and washed with acetone for 3~4 times. Then the ITO glass was cleaned again by acetone ultrasonically for 10 min. Finally, it was wash by Milli-Q water.

### 2.2.2 Preparation two dimensional MoS<sub>2</sub> by micromechanical cleavage

For the preparation of MoS<sub>2</sub> with different layers, I use physical cleavage method.<sup>14</sup> Commercial 3M tape was used to peel multi-layer MoS<sub>2</sub> from bulk. After peeling for several times, the tape with MoS<sub>2</sub> was attached to ITO glass. After 12 hours, the tape was removed from ITO. I can find that MoS<sub>2</sub> was remained on ITO.

### 2.2.3 Angle-resolved nanosphere lithography (AR-NSL)

Ag dimer nanostructures were fabricated on the MoS<sub>2</sub> / ITO substrate by Angle-resolved nanosphere lithography. First, a close-packed Langmuir–Blodgett monolayer of polystyrene beads (PS beads) was prepared on the surface of MoS<sub>2</sub> / ITO. For that, the solution of PS dissolved in ethanol and water was prepared. The diameter of PS was 350 nm. The detail procedure of the sample preparation was given in our previous method.

The Ag layer was deposited by electron beam evaporation. An evaporation rate of 20 nm / s was adopted in the experiment. In order to prepare the dimer structure, the substrate was moved with an angle of  $16^\circ \sim -16^\circ$ . After deposition, the mask of PS beads was removed by sonication. The progress could be described as follow:

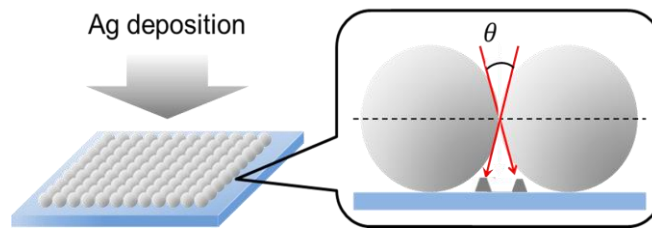


Figure 2.2. Illustration of the process of Ag NSL preparation

#### 2.2.4 Microscopic extinction measurements

The in situ extinction spectra was obtained by inverted microscopy (OLYMPUS IX-71) equipped with an objective lens (10x, NA=0.70, W.D.=0.1-1.3 mm, LUCPlanFLN) and a Xenon lamp (IX-HLSH1000, OLYMPUS) A slit of 20 was chosen for the measurement. A light source spectrum was acquired at an exposure time of 3 s in order to reduce the noise. Bare ITO glass which was also placed in the cell with the same dielectric environment was used as background. After that, in situ extinction of Ag / MoS<sub>2</sub> / ITO was measured with the same optical condition using a 3-electrode cell (Working electrode: Ag NSL / MoS<sub>2</sub> / ITO; counting electrode: Pt plate; reference electrode: AgCl/Ag. Electrolyte: 0.1 M NaClO<sub>4</sub> aq.). The incident polarization angle was 0 ° (NR minor axis direction) and 90 ° (NSL long axis direction).

### 2.3 Results and discussion

#### 2.3.1 Determination of layer number of MoS<sub>2</sub>

Since the properties of MoS<sub>2</sub> was closely related with the layer numbers, it was important to determine the layer number of our samples. Atomic force microscopy (AFM) could show the morphology information of substrate with thickness, therefore I applied AFM image to determine the layer number of MoS<sub>2</sub>.

Fig. 2.3 shows the AFM images of different MoS<sub>2</sub> samples. The dark and bright region imply ITO and MoS<sub>2</sub>, respectively. The thickness of samples in Fig.2.3 (a), (b) and (c) were around 30, 120 and 148 nm, respectively. Since the thickness of monolayer MoS<sub>2</sub> was around 0.85 nm, I could obtain the layer number of Fig.2.3 (a), (b) and (c) were about 35 (35 L), 141 (141 L) and 164 layers (164 L), respectively.

Fig. 2.4 shows the extinction spectra of MoS<sub>2</sub> / ITO of 35 L, 141 L and 164 L obtained in air. For all cases, two peaks appear at about 1.85 and 2.05 eV, which were corresponding to the A and B excitons of MoS<sub>2</sub> as discussed above. The line width of A exciton of all of the three examples were narrower than that of B exciton, indicating that damping of A excitation was less than that of B exciton. Based on it, in this experiment I tried to form strong coupling between plasmon and A exciton of MoS<sub>2</sub>.

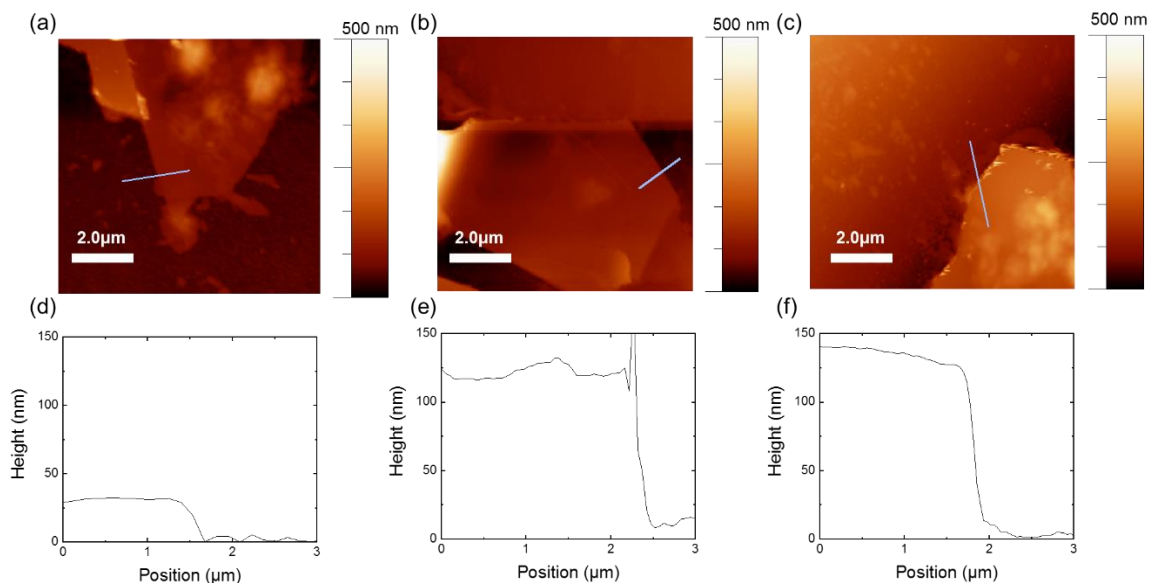


Figure 2.3. (a), (b), (c) AFM of MoS<sub>2</sub> / ITO with different thickness. (d), (e), (f) Isoheight of MoS<sub>2</sub> / ITO corresponding to (a), (b) and (c) respectively

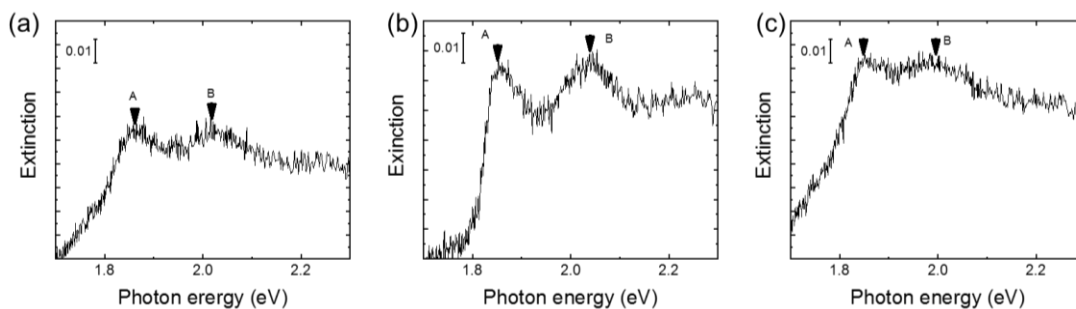


Figure 2.4. Extinction spectra of MoS<sub>2</sub> / ITO of (a) 35 L, (b) 141 L and (b) 164 L obtained in air. A and B indicates A and B excitons of MoS<sub>2</sub>

### 2.3.2 Interaction between MoS<sub>2</sub> and Ag LSPR in air

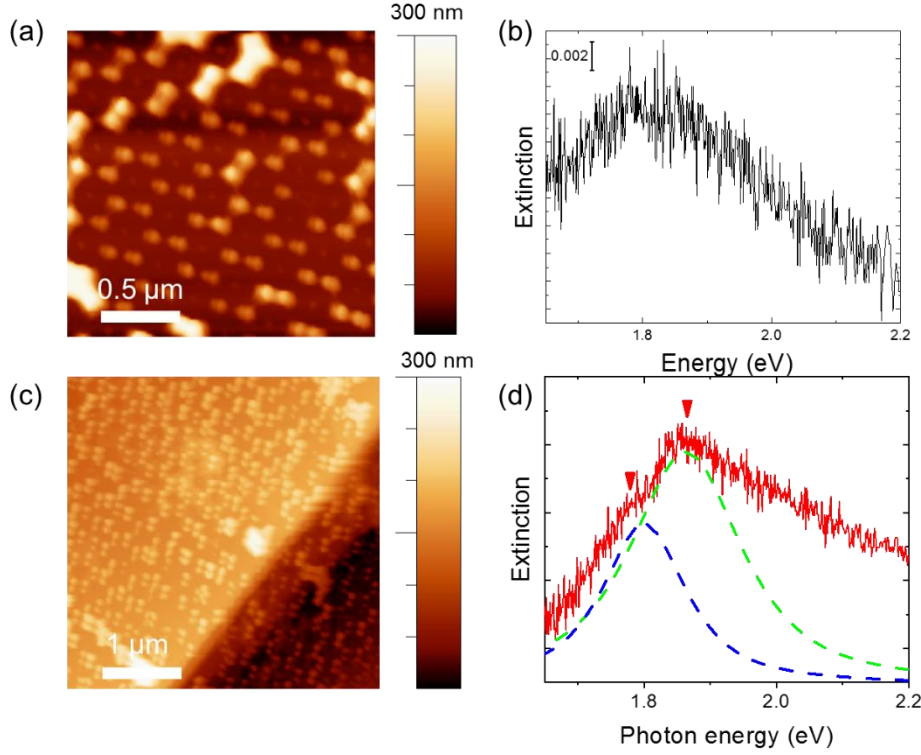


Figure 2.5. AFM of Ag dimer on (a) ITO and (c) MoS<sub>2</sub>. Extinction spectra of Ag dimer / ITO and Ag dimer / MoS<sub>2</sub> obtained in air. Green and blue broken line were the fitting line of upper branch and lower branch.

I firstly investigated the interaction between exciton of MoS<sub>2</sub> and Ag LSPR in air. The AFM of Ag dimer on ITO and MoS<sub>2</sub> was shown in Fig. 2.5 (a) and (c), the dimer structure could be observed from these pictures. The extinction of Ag / ITO obtained in air was shown in Fig.2.5 (b). The energy of Ag LSPR was at about 1.8 eV, which matches the energy of A exciton of MoS<sub>2</sub>. The extinction of Ag / MoS<sub>2</sub> substrate was shown in Fig.2.5 (d). Peak splitting could be observed from this figure. Two peaks appeared at about 1.78 and 1.86 eV. The strong coupling condition could be described as:

$$\hbar\Omega > \sqrt{\frac{\gamma_{UB}^2 + \gamma_{LB}^2}{2}} = \sqrt{\frac{\gamma_{exciton}^2 + \gamma_{LSPR}^2}{2}}$$

$\hbar\Omega$  was the splitting energy of strong coupling,  $\gamma_{UB}$  and  $\gamma_{LB}$  were the linewidth of upper and lower branches,  $\gamma_{exciton}$  and  $\gamma_{LSPR}$  were the linewidth of exciton mode and LSPR

mode. In this case,  $\gamma_{UB}$  and  $\gamma_{LB}$  was fitted as 0.0158 and 0.0045 eV, respectively, and the above situation was satisfied. From this fact, it can be recognized that the strong coupling formed between exciton of MoS<sub>2</sub> and Ag LSPR.

### 2.3.3 Active tuning of the strong coupling state between MoS<sub>2</sub> and Ag silver by electrochemical method

Since the frequency of plasmon was related with the electron density of metal nanoparticles, the energy of LSPR can be tuned by the control of the electrochemical potential.<sup>1</sup> This means that the state of strong coupling can be actively tuned by the electrochemical potential scan.

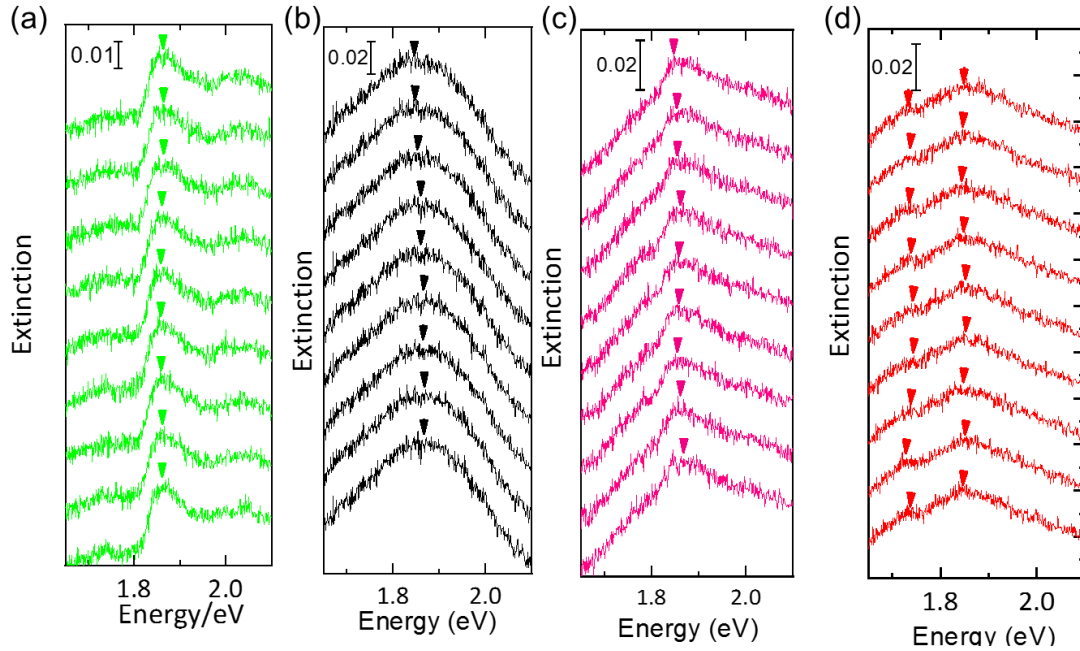


Figure 2.6. In situ extinction spectra of (a) MoS<sub>2</sub> / ITO, (b) Ag / ITO, (c) Ag / MoS<sub>2</sub> (35 L) and Ag / MoS<sub>2</sub> (164 L). The applied potential was from  $-0.8$  V (bottom) to  $0$  V (top). Triangles indicates the peak positions of the spectra.

Figure 2.6 (a) was the *in-situ* electrochemical extinction spectra of MoS<sub>2</sub>. Electrochemical potential was scanned from  $-0.8$  to  $0$  V corresponding to bottom to top. Triangles indicates the position of A exciton. Since the extinction of exciton was not related with electron density,<sup>15</sup> A exciton does not change during the potential shift, keeping with

a value of 1.85 eV. For Ag / ITO substrate, from Fig. 2.6 (b), a slightly shift from 1.815 to 1.881 eV was observed when the potential shift from 0 to  $-0.8$  V. This was due to the change of the electron density of the nanoparticles. For Ag / MoS<sub>2</sub> (164 L), only one peak could be observed during the electrochemical potential shift, indicating that strong coupling region was not generated. The reason of this phenomenon was that the dipole moment of MoS<sub>2</sub> decreases with increasing layer numbers,<sup>11</sup> and the coupling strength was proportional to the dipole moment.<sup>16</sup> For MoS<sub>2</sub> of 164 layers, the dipole moment was too small to form the strong coupling.

In the case of 35 L MoS<sub>2</sub>, peak splitting could be observed during the potential shift. The upper branch shift from 1.84 to 1.85 eV while the lower branch shifts from 1.734 to 1.73 eV with the electrochemical potential scan from 0 to  $-0.8$  V.

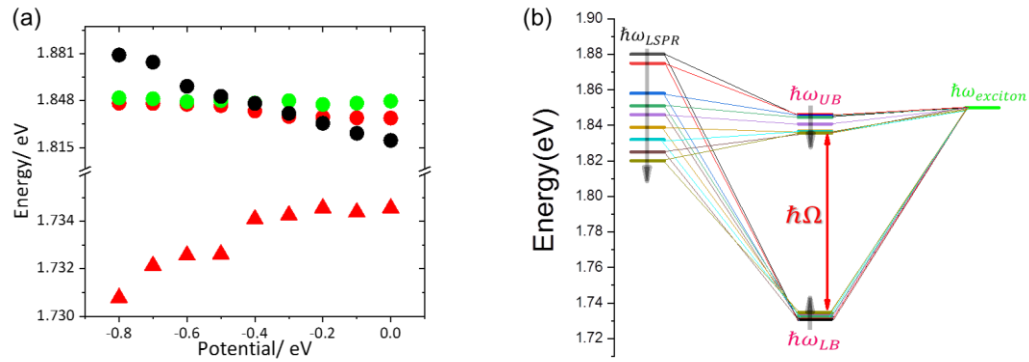


Figure 2.7. Energies of LSPR (black dots), MoS<sub>2</sub> (green dots), upper branches (red dots) and lower branches (triangle dots) of MoS<sub>2</sub> / ITO at different potential. (b) energy diagram of the active tuning of strong coupling state of MoS<sub>2</sub> / ITO system.

Figure 2.7 (a) and (b) summarized the energy diagram of LSPR, A exciton of MoS<sub>2</sub>, upper and lower branches of MoS<sub>2</sub> at different potential. As described in Fig.2.6, the frequency of LSPR red shift as the potential shift to negative direction due to the decrease of electron density and energy of exciton remains stable. Remarkably, the difference between upper and lower branches increases as the potential shift to  $-0.8$  V, reaching a

splitting energy of about 0.117 eV. Therefore, the active tune of strong coupling state was realized by electrochemical method.

## 2.4 Conclusion

In this chapter, I explored the method to extend the available solar spectra by strong coupling. Due to the unique thickness-dependent electronic properties and strong exciton, MoS<sub>2</sub> was adopted as a candidate for our experiment. For the plasmonic cavity, I choose Ag dimer due to the low extent of damping. By tuning the distance of gap between the dimer, I fabricated Ag nanostructure with the same energy of A exciton of MoS<sub>2</sub> and observed the peak splitting of extinction in air, which was demonstrated as strong coupling.

I later obtained the extinction spectra of Ag and Ag/MoS<sub>2</sub> under electrochemical control using the system. In the case of Ag dimer structures, the resonance wavelength shifts to the higher energy region by the electrochemical potential scan from 0 to −0.8 V. This was the result of the increase of electron density which was directly correlated with the plasmon resonance character. Based on this fact, I have measured extinction spectra for Ag/MoS<sub>2</sub> system at each electrochemical potential. By the cathodic potential scan from 0 to −0.8 V, I have confirmed that the splitting energy gradually became larger. This splitting energy change would be caused by the electrochemical tuning of the LSPR energy. Through the above attempts, I could conclude that the electrochemical method has the great advantage to tune the strong coupling state between Ag/MoS<sub>2</sub> heterostructure.

## References

1. Kato, F.; Minamimoto, H.; Nagasawa, F.; Yamamoto, Y. S.; Itoh, T.; Murakoshi, K., Active Tuning of Strong Coupling States between Dye Excitons and Localized Surface Plasmons Via Electrochemical Potential Control. *ACS Photonics* **2018**, 5 (3), 788-796.
2. Wang, X.; Wang, P.; Wang, J.; Hu, W.; Zhou, X.; Guo, N.; Huang, H.; Sun, S.; Shen, H.; Lin, T., Ultrasensitive and Broadband MoS<sub>2</sub> Photodetector Driven by Ferroelectrics. *Adv. Mater.* **2015**, 27 (42), 6575-6581.
3. Yuan, Y. J.; Tu, J. R.; Ye, Z. J.; Chen, D. Q.; Hu, B.; Huang, Y. W.; Chen, T. T.; Cao, D. P.; Yu, Z. T.; Zou, Z. G., MoS<sub>2</sub>-Graphene/ZnIn<sub>2</sub>S<sub>4</sub> Hierarchical Microarchitectures with an Electron Transport Bridge between Light-Harvesting Semiconductor and



Cocatalyst: A Highly Efficient Photocatalyst for Solar Hydrogen Generation. *Appl. Catal. B* **2016**, 188, 13-22.

4. Yin, Z.; Li, H.; Li, H.; Jiang, L.; Shi, Y.; Sun, Y.; Lu, G.; Zhang, Q.; Chen, X.; Zhang, H., Single-Layer MoS<sub>2</sub> Phototransistors. *ACS nano* **2012**, 6 (1), 74-80.
5. Yin, Z.; Zhang, X.; Cai, Y.; Chen, J.; Wong, J. I.; Tay, Y. Y.; Chai, J.; Wu, J.; Zeng, Z.; Zheng, B., Preparation of MoS<sub>2</sub>-MoO<sub>3</sub> Hybrid Nanomaterials for Light - Emitting Diodes. *Angew. Chem. Int. Ed.* **2014**, 53 (46), 12560-12565.
6. Tian, Z.; Wu, K.; Kong, L.; Yang, N.; Wang, Y.; Chen, R.; Hu, W.; Xu, J.; Tang, Y., Mode-Locked Thulium Fiber Laser with MoS<sub>2</sub>. *Laser. Phys. Lett.* **2015**, 12 (6), 065104.
7. Tongay, S.; Zhou, J.; Ataca, C.; Lo, K.; Matthews, T. S.; Li, J.; Grossman, J. C.; Wu, J., Thermally Driven Crossover from Indirect toward Direct Bandgap in 2d Semiconductors: MoSe<sub>2</sub> Versus MoS<sub>2</sub>. *Nano Lett.* **2012**, 12 (11), 5576-5580.
8. Liu, C.-H.; Kim, I. S.; Lauhon, L. J., Optical Control of Mechanical Mode-Coupling within a MoS<sub>2</sub> Resonator in the Strong-Coupling Regime. *Nano Lett.* **2015**, 15 (10), 6727-6731.
9. Lei, Z.; Xu, L.; Jiao, Y.; Du, A.; Zhang, Y.; Zhang, H., Strong Coupling of MoS<sub>2</sub> Nanosheets and Nitrogen - Doped Graphene for High-Performance Pseudocapacitance Lithium Storage. *Small* **2018**, 14 (25), 1704410.
10. Autore, M.; Li, P.; Dolado, I.; Alfaro-Mozaz, F. J.; Esteban, R.; Atxabal, A.; Casanova, F.; Hueso, L. E.; Alonso-González, P.; Aizpurua, J., Boron Nitride Nanoresonators for Phonon-Enhanced Molecular Vibrational Spectroscopy at the Strong Coupling Limit. *Light: Sci. Appl.* **2018**, 7 (4), 17172-17172.
11. Klein, J.; Wierzbowski, J.; Regler, A.; Becker, J.; Heimbach, F.; Müller, K.; Kaniber, M.; Finley, J. J., Stark Effect Spectroscopy of Mono-and Few-Layer MoS<sub>2</sub>. *Nano Lett.* **2016**, 16 (3), 1554-1559.
12. Dhakal, K. P.; Duong, D. L.; Lee, J.; Nam, H.; Kim, M.; Kan, M.; Lee, Y. H.; Kim, J., Confocal Absorption Spectral Imaging of MoS<sub>2</sub>: Optical Transitions Depending on the Atomic Thickness of Intrinsic and Chemically Doped MoS<sub>2</sub>. *Nanoscale* **2014**, 6 (21), 13028-13035.
13. Mak, K. F.; He, K.; Lee, C.; Lee, G. H.; Hone, J.; Heinz, T. F.; Shan, J., Tightly Bound Trions in Monolayer MoS<sub>2</sub>. *Nat. Mater.* **2013**, 12 (3), 207-211.

14. Novoselov, K. S.; Jiang, D.; Schedin, F.; Booth, T.; Khotkevich, V.; Morozov, S.; Geim, A. K., Two-Dimensional Atomic Crystals. *P. Natl. Acad. Sci. USA* **2005**, *102* (30), 10451-10453.
15. Fox, M., Optical Properties of Solids. American Association of Physics Teachers: 2002.
16. Marquier, F.; Sauvan, C.; Greffet, J. J., Revisiting Quantum Optics with Surface Plasmons and Plasmonic Resonators. *ACS photonics* **2017**, *4* (9), 2091-2101.

## *Chapter 3.*

# **In-situ monitoring of electronic structure of modal strong coupling electrode for enhanced plasmonic water oxidation**

---

### **3.1 Introduction**

Solar energy conversion is regarded as an effective solution for the problem of energy and the environment.<sup>1-3</sup> Thus, various photo conversion systems for oxygen evolution reactions (OERs) have been investigated during the past decades.<sup>4-11</sup> Localized surface plasmon resonance (LSPR) is the collective oscillation of free electrons, which generates an enhanced electromagnetic field in the vicinity of a metal nanostructure surface. LSPR allows efficient use of light energy on the nanoscale.<sup>12-15</sup> Excited charge carriers generated in metal nanostructures can promote efficient multi-electron transfer reactions.<sup>16-18</sup> A representative system is the combination of a plasmonic nanostructure with a wide band-gap semiconductor electrode.<sup>9, 19-22</sup> In this system, the oxidation reactions are triggered at the interface between a metal and semiconductor while the excited electrons are injected into the conduction band of the semiconductor.<sup>23-24</sup> Our research not only clarified the spatial distribution of the reactive site but also gave information on the absolute electrochemical potential of the generated holes.<sup>25</sup>

In a plasmonic photoconversion system, the photoresponse depends strongly on the optical property of the metal nanostructures, which is limited to the relatively narrow absorption band region.<sup>26-27</sup> To overcome this limitation, a lot of research has been conducted to broaden the available wavelength.<sup>9, 28-34</sup> For instance, a metal–insulator–metal structure has a broad absorption band in the range of visible light.<sup>35-37</sup> Lu and coworkers have fabricated TiO<sub>2</sub> electrode sandwiched with an Au film and Au nanoparticles (Au NPs). This Au NP/TiO<sub>2</sub>/Au film has a fivefold-enhanced incident photon-to-current conversion efficiency (IPCE) in the broad range.<sup>38</sup> Mulvaney's group investigated the mechanism for generating and separating hot carriers on such a sandwiched structure.<sup>39</sup> However, for broadening the absorption wavelength region, the strong coupling that forms the new hybridized state owing to the electronic interaction between two energy states is also a good candidate.<sup>40-42</sup>

Recently, modal strong coupling has been successfully applied to a plasmonic OER electrode consisting of a Au NP/TiO<sub>2</sub>/Au film (ATA).<sup>43</sup> In this system, the interaction between the LSPR mode on Au NPs and the Fabry–Pérot cavity formed between the TiO<sub>2</sub> and Au layers leads to Rabi splitting, which broadens the absorption wavelength.<sup>43</sup> Although this system has achieved high photoconversion efficiency, the electronic structure of the system during OER and the photon localization effect are not fully understood yet. It is important to determine the absolute potential of the Fermi level in the plasmonic system, because the electrochemical potential of the electrified interfaces is essential for OER reactivity.<sup>44-48</sup>

Graphene-based electrochemical Raman measurement is quite useful for *in-situ* monitoring of the electronic structure at electrified interfaces. Raman bands on graphene can provide a lot of information such as the interaction between the graphene and substrate,<sup>49-50</sup> strain,<sup>49</sup> and the Fermi energy.<sup>51-53</sup> In our previous investigation, a blueshift of the 2D band ( $\omega_{2D}$ ) was detected on metal substrates compared with insulator substrates because of the reduction of the Fermi velocity.<sup>50</sup> The Raman spectrum showed the following variations with doping:<sup>53</sup>

(1) The G band position ( $\omega_G$ ) blueshifts and becomes sharper when the hole doping is increased, owing to the nonadiabatic removal of the Kohn anomaly at  $\Gamma$  and the blockage of phonon decay into electron–hole pairs because of the Pauli exclusion principle.<sup>51-52, 54-55</sup>

(2) The intensity ratio of the 2D band and G band decreases with the hole doping because the contribution of electron–electron scattering decreases with decreasing carrier concentration.<sup>56</sup>

Recently, we have shown that the localization of the plasmonic field also affects the intensity ratio of the 2D and G bands via the change in the electronic excitation process, which affects the resonance in Raman scattering.<sup>57</sup>

On the basis of the above, this study attempted to determine the electrochemical potential of the Fermi level at the ATA electrode during an OER using graphene-based Raman measurements. This method allowed us to investigate the Fermi level of ATA electrodes showing different OER performances. Our Raman measurements have revealed that an electrode with a more positive Fermi level has higher OER performance. Other ATA properties, such as the charge separation efficiency, were also characterized. This

investigation provides new insight on the electronic structure in a high-performance ATA system.

## **3.2 Experimental**

### **3.2.1 Preparation of the Au NPs / TiO<sub>2</sub> / Au film (ATA) substrate**

Firstly, Au film with the thickness of 100 nm was sputtered onto the surface of silica glass. The TiO<sub>2</sub> layer of 30 nm thickness was deposited using atomic layer deposition method. Then, Au film with 3 nm was evaporated and annealed in air at 300 °C to obtain Au NPs. In order to embed Au nanoparticles into the TiO<sub>2</sub> layer to enhance the interaction between LSPR and Fabry-Pérot cavity, additional TiO<sub>2</sub> layer with the thickness of 7 nm was deposited to the electrode.

### **3.2.2 Preparation of graphene supported ATA and Raman measurements**

Single layer graphene was synthesized on 1 cm<sup>2</sup> Cu foil at 1000 °C using the chemical vapor deposition method. The detailed method for transferring graphene was reported in our previous paper. Single layer graphene was transferred to the surface of ATA electrode using poly methyl methacrylate. Electrochemical Raman measurements have been conducted using a three-electrode cell. Graphene supported ATA (Gr / ATA) electrodes were used as the working electrode. Saturated Ag / AgCl electrode and Pt coil were served as reference and counter electrodes, respectively. The electrolyte solution was 0.5 M NaClO<sub>4</sub> aq. Raman spectra were collected with the homebuilt confocal Raman scope equipped with 785 nm laser. The laser exposure time was 600 sec. The laser power was set as 0.1 mW. The potential was controlled with a potentiostat with the potential range of 0 to 0.4 V.

## **3.3 Results and discussion**

### **3.3.1 Morphology and optical properties of ATA substrate**

Fig. 3.1 (a) and (b) show the schematic of the ATA electrode with graphene coverage (Gr/ATA) and the SEM image of the surface, respectively. The dark side in the SEM image is attributed to the region covered with single-layer graphene. I prepared two ATA electrodes with distinct coupling strengths. The reflection spectra for both electrodes are shown in Fig. 3.1 (c). The spectra confirm the formation of modal strong coupling on one electrode (strongly coupled (SC)-ATA), while another electrode shows just a single peak (non-strongly coupled (NSC)-ATA). The verification of strong coupling on the ATA is given as follow:

Theoretically, the condition for the definition of the strong coupling condition could be described as follow:<sup>43</sup>

$$\hbar\Omega > \sqrt{\frac{\gamma_{UB}^2}{2} + \frac{\gamma_{LB}^2}{2}} = \sqrt{\frac{\gamma_{cavity}^2}{2} + \frac{\gamma_{LSPR}^2}{2}}$$

where  $\hbar\Omega$ ,  $\gamma_{UB}$ , and  $\gamma_{LB}$ , represent the splitting energy defined as the difference of two peak positions, the linewidths of the upper and lower branch modes, respectively and  $\gamma_{cavity}$  and  $\gamma_{LSPR}$  are the linewidths of the nanocavity and LSPR modes, respectively. For SC-ATA described in the main text,  $\hbar\Omega$  was 0.38 eV while  $\gamma_{UB}$  and  $\gamma_{LB}$  were 0.35 and 0.22 eV, respectively. Therefore,  $\sqrt{\frac{\gamma_{UB}^2}{2} + \frac{\gamma_{LB}^2}{2}}$  was calculated as 0.29 eV, indicating that the strong coupling condition could be satisfied.

Two peaks appear for the SC-ATA electrode around 700 and 550–600 nm, corresponding to the lower and upper branches, respectively. This leads to a coupling strength of about 0.38 eV. The difference in modal coupling strength has been shown to be due to an appropriate interlayer depth of Au nanoparticles in the TiO<sub>2</sub> layer around 7 nm.<sup>19,</sup>  
<sup>43</sup> To investigate the electrode dependence, I also conducted our experiment using two additional electrodes prepared with the same method (Fig. 3.2). Using these two electrodes, I collected photocurrents and Raman spectra simultaneously under an illumination of  $\lambda_{ex}$  = 785 nm with a continuous-wave (CW) laser with a diameter of 1  $\mu$ m.

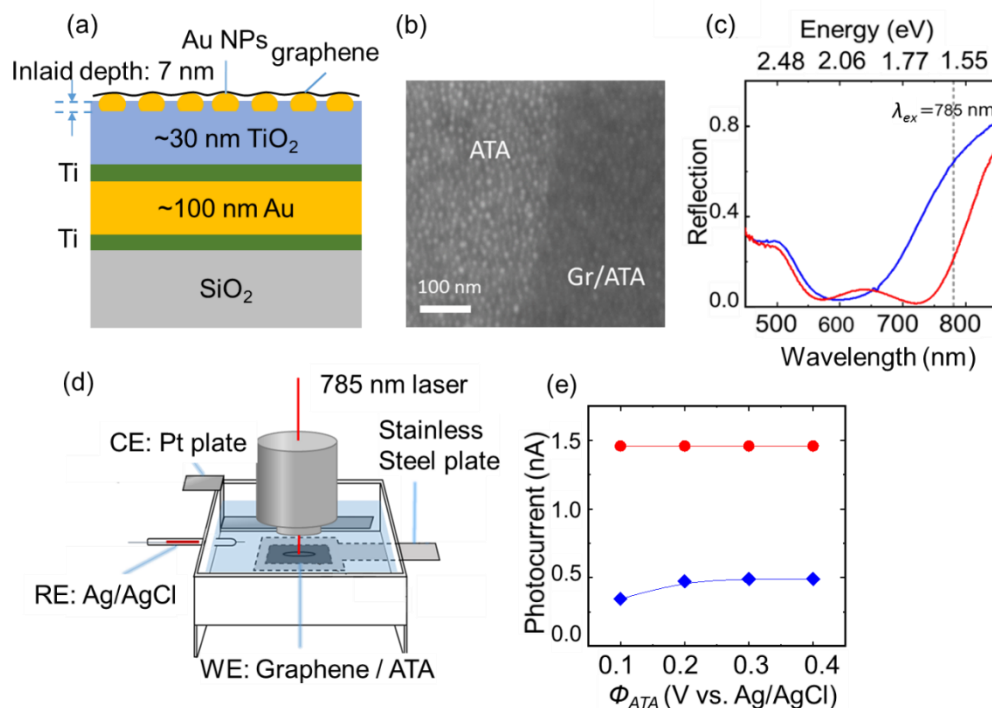


Figure 3.1. (a) Illustrated structure of graphene/ATA. (b) SEM of Gr/ATA. (c) Reflection spectra of ATA. Red line: SC-ATA; blue line: NSC-ATA; dashed gray line: laser energy. (d) Schematic of the cell used for electrochemical in-situ SERS. (e) Relationship between photocurrent and applied potential. Red solid circles: SC-ATA; blue rhombuses: NSC-ATA.

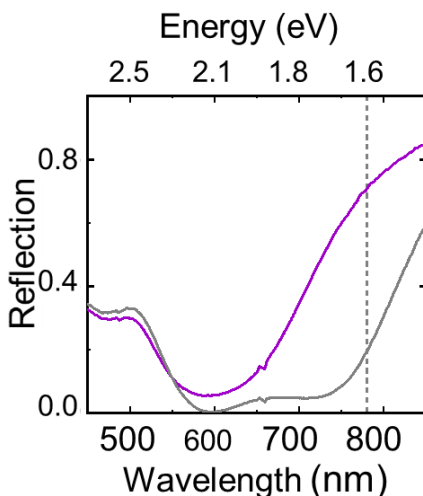


Figure 3.2. Reflection spectra of NSC-ATA2 and NSC-ATA3. Gray line indicates NSC-ATA2 and purple line indicated NSC-ATA3.

### 3.3.1 Catalysis performance of ATA

Photocurrent measurements were performed with a static electrochemical potential ranging between 0.1 to 0.4 V under laser illumination with a wavelength of  $\lambda_{\text{ex}} = 785$  nm using a three-electrode electrochemical cell as shown in Fig. 3.1(d). It is important that, in these experiments, both the photocurrents and Raman spectra were collected at the same time under the incident laser illuminations ( $I_{\text{ex}} = 0.1$  mW). The red circles and blue diamonds in Fig. 3.1 (e) represent the photocurrent values for Gr/SC-ATA and Gr/NSC-ATA, respectively, obtained at specific sites on the ATA surface. The original results of the photocurrent measurements are Fig. 3.3. Transferring single-layer graphene onto the ATA electrode did not affect the photoelectrochemical performance of the system in the present visible–near-infrared wavelength region. A stable photocurrent on SC-ATA was obtained at different electrochemical potentials. However, those on NSC-ATA were lower by one third, showing a slight increase with the anodic potential scan. The photocurrent variation at these two sites originated from the different optical properties. Considering that the reflections of SC-ATA and NSC-ATA were about 0.2 and 0.6, respectively, the threefold higher photocurrent reflects an OER efficiency 1.5 times higher at SC-ATA than at NSC-ATA under near-infrared laser illumination at 785 nm.

The potential dependence of the photocurrent directly indicates the charge separation efficiency because a relatively high charge separation efficiency results in independence from the electrode potential.<sup>59</sup> Therefore, I found that the charge separation efficiency on SC-ATA was superior to that on NSC-ATA. The heterogeneity of the  $\text{TiO}_2$  structure, as shown in Ref. 43 and Fig. 3.5, is one of the origins of the excited carrier recombination via the  $\text{TiO}_2$  surface states.<sup>60</sup> Considering the optical property difference, the formation of the modal strong coupling is also expected to contribute to the efficiency. I also performed these photocurrent measurements using other ATA electrodes as shown in Figs. 3.3 and Figs. 3.4 and found a similar tendency to that in Fig. 3.1 (e).



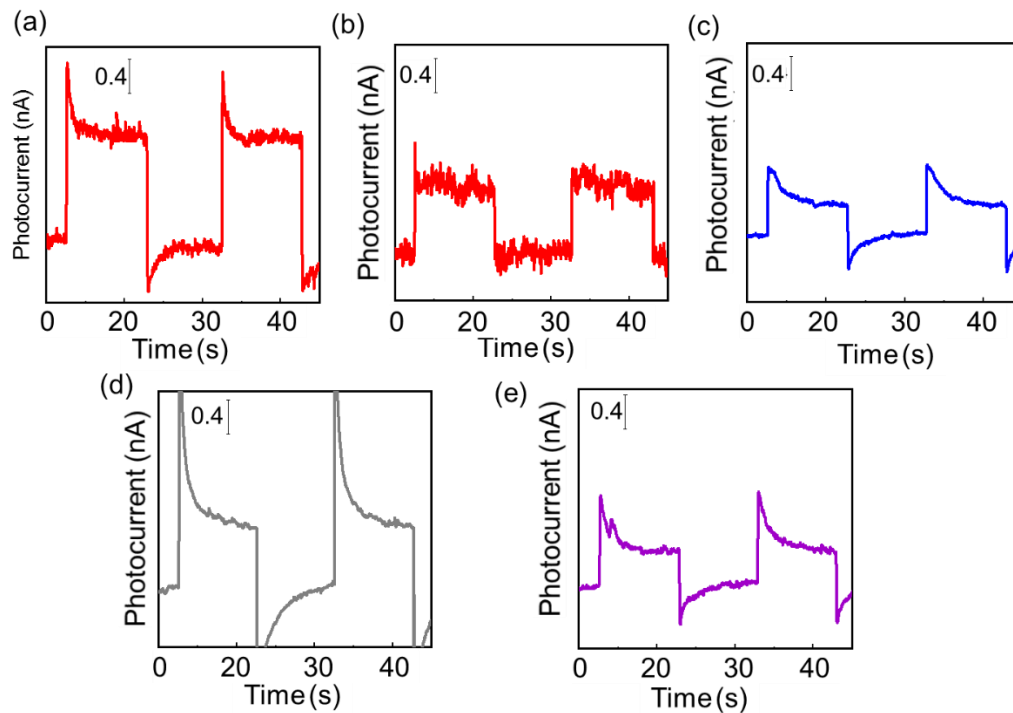


Figure 3.3. Photocurrents for (a) SC-ATA, (b) SC-ATA2, (b) NSC-ATA (c) NSC-ATA2 and (de) NSC-ATA3 at 0.4 V.

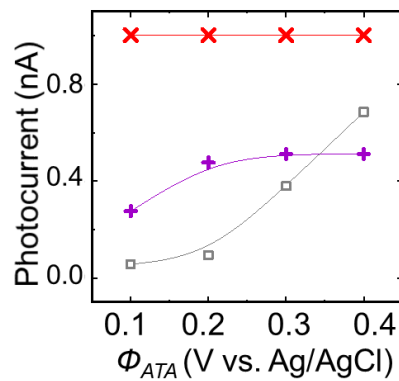


Figure 3.4. Relationship between photocurrents and applied potential. Red cross: SC-ATA2; purple cross: NSC-ATA2; gray hollow square: NSC-ATA3.

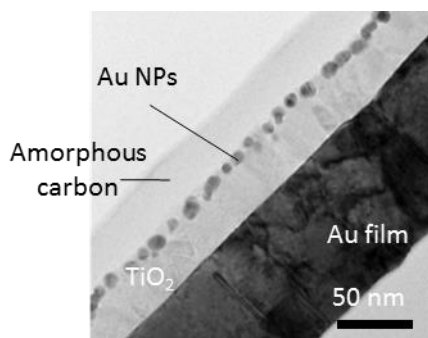


Figure 3.5. Cross sectional view of ATA.

### 3.3.1 Determination of the Fermi level of ATA

Considering the results of the photocurrent measurements, the Fermi level of Au NPs is expected to be different because it reflects the OER performance.<sup>61</sup> I obtained the electrochemical surface-enhanced Raman scattering (EC-SERS) spectra of the graphene layer supported on the ATA surface because the Raman band of graphene can be used to probe the Fermi level of the substrate.<sup>49-50</sup> Fig. 3.6 (a) and (b) show the EC-SERS spectra of graphene-ATA collected simultaneously with the photocurrent measurement of Fig. 3.1 (e). For comparison, I also prepared graphene-covered Au nanostructures on a conductive glass substrate (indium tin oxide; ITO) named Gr/Au/ITO as shown in Fig. 3.6(c). This is because the Fermi level of the Au on ITO is equal to that of ITO (equal to the applied potential) (see Fig. 3.9). At about 1580 and 2600  $\text{cm}^{-1}$ , the G and 2D bands can be observed with distinct intensities depending on the electrochemical potential. Previous research found no obvious change in the G band intensity ( $I_G$ ).<sup>53</sup> However, the intensity of the 2D band ( $I_{2D}$ ) exhibits potential dependence with the anodic potential scan. This could be due to the contribution of electron–electron scattering depending on the electron density.<sup>53</sup> The  $I_{2D}$  for SC-ATA was much lower than that for NSC-ATA. This implies that the doping level of the former was more positive than that of the later. Thus, these differences strongly correlate with the performance as shown in Fig. 3.1 (e).

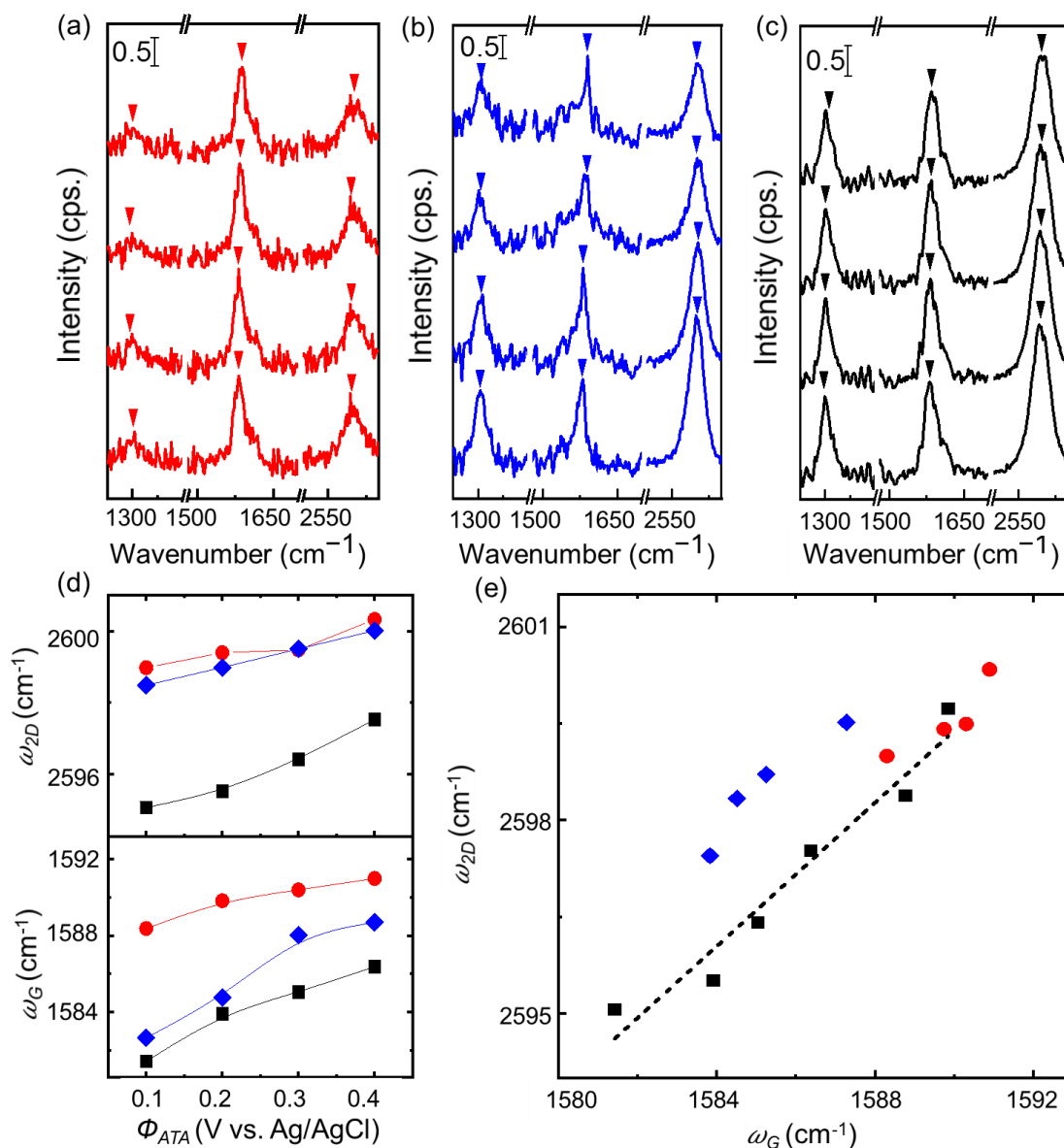
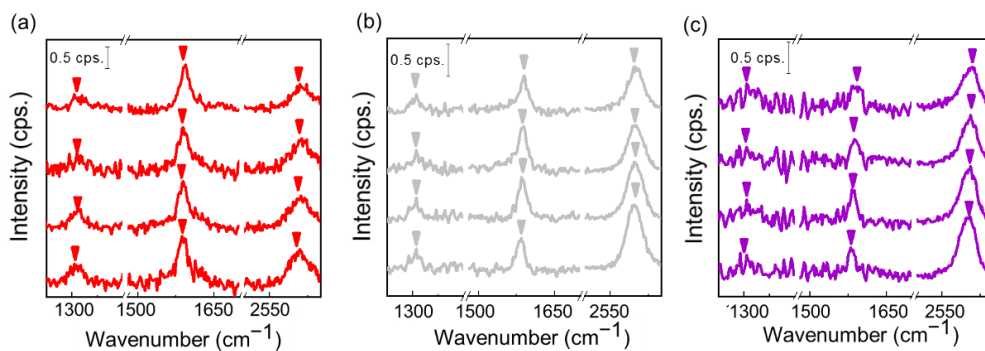


Figure 3.6. EC-SERS of (a) Gr/SC-ATA, (b) Gr/NSC-ATA, and (c) Au/ITO. Triangles indicate the positions of peaks. (d) G band position ( $\omega_G$ ) and 2D band position ( $\omega_{2D}$ ) of Gr/ATA and Gr/Au/ITO at potential from 0.1 to 0.4 V. (e)  $\omega_G$  vs.  $\omega_{2D}$  for hole-doped Gr/ATA, Gr/Au/ITO, and Gr/Au/TiO<sub>2</sub>. Red solid circles: SC-ATA; blue rhombuses: NSC-ATA; black squares: Au/ITO; dashed black line: linear fitting of  $\omega_G$  vs.  $\omega_{2D}$  for Gr/Au/ITO. The electrode potential was scanned from 0.1 to 0.4 V for Gr/ATA, from 0.1 to 0.6 V for Gr/Au/ITO, and from -0.4 to 0.9 V for Gr/Au/TiO<sub>2</sub> with an interval of 0.1 V.



**Figure 3.7.** Raw EC-SERS of different sites at potential from 0.1 V (bottom) to 0.4 V (upper). (a) SC-ATA2. (b) NSC-ATA2. (c) NSC-ATA3. Triangles indicates the peak positions of D, G and 2D peaks.

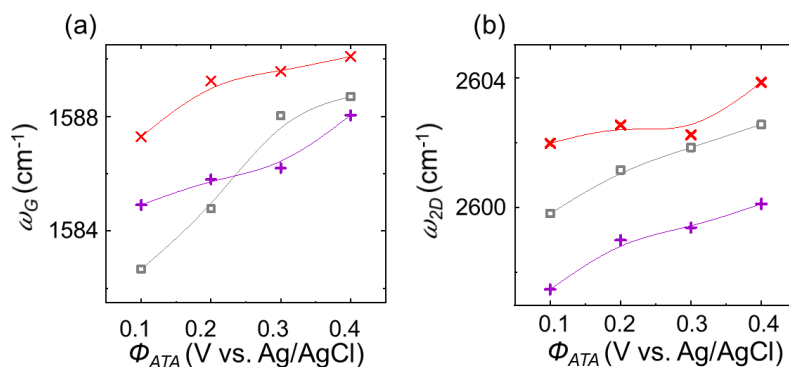


Figure 3.8. (a) G band position ( $\omega_G$ ) and (b) 2D band position ( $\omega_{2D}$ ) at potential from 0.1 V to 0.4 V. Red cross: SC-ATA2; purple cross: NSC-ATA2; gray hollow square: NSC-ATA3.

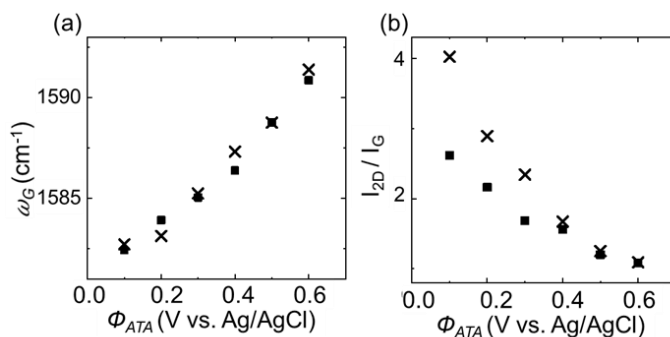


Figure 3.9. The  $\omega_G$  of Gr / Au / ITO and Gr / ITO as the function of applied potential. Black cross: Gr / ITO; black square: Gr / Au / ITO.

The  $\omega_G$  and  $\omega_{2D}$  band positions are plotted in Fig. 3.6 (d) as functions of the electrode potential. The  $\omega_G$  value for SC-ATA changes from 1588 to 1590  $\text{cm}^{-1}$ , while  $\omega_G$  on NSC-ATA shifts from 1585 to 1588  $\text{cm}^{-1}$  with the anodic potential scan. Both  $\omega_G$  positions for SC-ATA and NSC-ATA are at higher wavenumbers than that of Gr/Au/ITO. These changes in the wavenumber result from the Fermi level shift during the OER.<sup>60</sup> A similar potential dependence was also observed for the 2D band. It is known that positive doping of graphene against the Dirac point (at 0.1 V vs. Ag/AgCl)<sup>50</sup> results in blueshifts of both the  $\omega_G$  and  $\omega_{2D}$  bands.<sup>52-53</sup> Thus, from the present wavenumber shift, I can conclude that the Fermi level of SC-ATA is much more positive than those of NSC-ATA and Gr/Au/ITO. The  $\omega_G$  and  $\omega_{2D}$  vs. other ATA electrodes are shown in Fig. 3.8.

Information on charge doping can be obtained from correlation plots of  $(\omega_G, \omega_{2D})$ .<sup>49-50, 60, 62</sup> I prepared the G-2D correlation plots for SC-ATA, NSC-ATA, and Gr/Au/ITO using the spectra in Fig. 3.6 (d) at different electrochemical potentials as shown in Fig. 3.6 (e). In the figure, the positions of  $(\omega_G, \omega_{2D})$  for Gr/Au/ITO (black square plots) linearly changed in the range  $1581 < \omega_G < 1590 \text{ cm}^{-1}$  and  $2595 < \omega_{2D} < 2600 \text{ cm}^{-1}$  during a potential scan from 0.1 to 0.6 V. As I mentioned, this line could be used to indicate the shift of the Fermi level. The  $(\omega_G, \omega_{2D})$  position for SC-ATA was in a higher wavenumber region than that of NSC-ATA, indicating the positive doping of graphene on SC-ATA. The positive doping also signified the lower electronic density of Au nanoparticles on SC-ATA, reflecting the positive potential of the Fermi level. Furthermore, the distribution of  $(\omega_G, \omega_{2D})$  for NSC-ATA was wider than that of SC-ATA, showing the better charge separation efficiency of SC-ATA than NSC-ATA.<sup>60</sup> Incidentally, the strain effect could be also obtained from the slope of the correlation plot. Judging from Fig. 3.6 (e), the strain of the graphene layer was stable during the reactions.<sup>49-50, 62</sup>

Beside the shifts of  $\omega_G$ , the intensity ratio of the 2D band to the G band ( $I_{2D} / I_G$ ) depends on the graphene doping level.<sup>52-53</sup> To visualize the potential dependence on each band, Fig. 3.10 (a)-(b) show two-dimensional scattering intensity plots prepared from the EC-SERS spectra in Fig. 3.6. In addition, I examine the laser intensity dependence using NSC-ATA as shown in Fig. 3.10 (c). The scattering intensities for Fig. 3.10(a)–(c) were normalized with the laser intensity. The changes in the intensities of the G and 2D bands for SC-ATA and NSC-ATA can be seen qualitatively in these plots. In particular,  $I_G$  for

SC-ATA was much higher than  $I_{2D}$ , leading to a lower  $I_{2D}/I_G$ . The stable  $I_{2D}$  of SC-ATA at each potential can be considered as the result of the excellent charge separation efficiency, leading to the positive shift of the Fermi level. This is because  $I_{2D}$  is related to the electron–electron scattering rate.<sup>53, 63</sup> On NSC-ATA,  $I_G$  was almost constant while  $I_{2D}$  decreased under the anodic potential scan. The point is that the change in  $I_{2D}$  was much greater under the intense laser illumination (1.0 mW). This indicates that the strong laser makes the Fermi level shift on NSC-ATA more positive. This is understandable because stronger light illumination generates excess holes to improve photocurrent generation of OER on NSC-ATA. Similar results were observed in our previous study using a graphene-covered AuNP/TiO<sub>2</sub> system.<sup>60</sup> In that case, the Fermi level of the plasmonic electrode with high reactivity was negative under the weaker light illuminations, and shifted to the positive region owing to the excess hole accumulations. Therefore, I can conclude that a large number of carriers were generated under SC-ATA compared with the conventional AuNP/TiO<sub>2</sub>.

For further understanding, I estimated the absolute electrochemical potentials of the Fermi level ( $\Phi_{EF}$ ) for each electrode by comparing the EC-SERS spectra with those of Gr/Au/ITO. The correlation between  $\omega_G$  and the Fermi level is logarithmic near the Dirac point but linear far from the Dirac point.<sup>55</sup> Its slope depends on the peak width of the G band, which is not related to Landau damping.<sup>55</sup> For the Gr/Au/ITO electrode, it is generally difficult to determine such a linewidth because plasmon excitation could change the phonon dispersion and induce peak splitting of the G band. However, the plots of  $\omega_G$  vs.  $\Phi_{EF}$  for Gr/Au/ITO and Gr/ITO almost overlap as shown in Fig. 3.9. This means that comparison with  $\omega_G$  would be effective for estimating  $\Phi_{EF}$  for the ATA system. Fig. 3.10 (d) shows the correlations of  $\omega_G$  and  $I_{2D}/I_G$  for SC-ATA and NSC-ATA collected at 0.1 and 1 mW with the estimated Fermi level of graphene ( $\Phi_{EF}$ ). The above properties of Gr/Au/ITO are also shown as black squares. The estimated absolute  $\Phi_{EF}$  is depicted on the top axis and by the color scale. In this figure, the size of each circle represents the obtained photocurrent at each applied potential. When I compare these four conditions, I find that the electrode with a higher photocurrent at 0.4 V had a more positive Fermi level at 0.9 V. Therefore, I can conclude that the Fermi level is directly correlated with the OER activity of ATA electrodes.<sup>64</sup>

More importantly,  $I_{2D}/I_G$  for SC-ATA is lower in spite of the comparable photocurrents and the Fermi level for NSC-ATA at 1 mW. This indicates an additional contribution to changes in the intensity ratio. Recently, it has been reported that plasmon excitation changes the phonon dispersion.<sup>65</sup> The strong localization of LSPR energy has a counter-effect on phonon renormalization, giving rise to a hardening phonon.<sup>57</sup> An increase in G band intensity was observed under such conditions.<sup>57</sup> From this finding, I attribute the lower  $I_{2D}/I_G$  on SC-ATA to the strong localization of the photon energy under the modal strong coupling.

Finally, I propose the energy diagram of this ATA system in Fig. 3.10 (e). At  $\Phi_{ATA} = 0.4$  V, a Schottky barrier forms at the metal–semiconductor interface because of the flat band potential of  $\text{TiO}_2$  ( $\Phi_{fb} = -0.6$  V vs.  $\text{Ag}/\text{AgCl}$  at  $\text{pH} = 7$ ).<sup>66</sup> Under light illumination, excited electrons are generated and injected into the conduction band of  $\text{TiO}_2$ . All results show that electron–hole generation is promoted dramatically by the strong photon localization under the modal strong coupling. Because of the shorter dephasing time on ATA ( $\sim 4.5$  fs), the strong localization is the key to the high OER performance as reflected by the improved OER rate ( $k_{ox}$ ).<sup>43</sup> This important point was firstly revealed by our Raman measurements. In addition, because of the higher charge separation efficiency on SC-ATA, much more holes accumulate in Au NPs. The energy shift of electrons in Au NPs is estimated to be  $e|\Phi_{fb} - \Phi_{EF}| = e|(-0.6) - 0.9| = 1.5$  eV, which is comparable to the excitation energy because the energy of the 785 nm illumination light is 1.58 eV. Superior OER catalysis with higher  $k_{ox}$  for SC-ATA than for NSC-ATA results in a positive shift of the Fermi level despite illumination with low-energy near-infrared light with relatively weak intensity. The rate  $k_{ox}$  can be efficiently enhanced by strong localization of photons under the formation of modal strong coupling. Although there is still room for investigating its effect on charge separation efficiency, the strong coupling has now been revealed as the origin of the photocurrent at the ATA electrodes with higher OER efficiency.

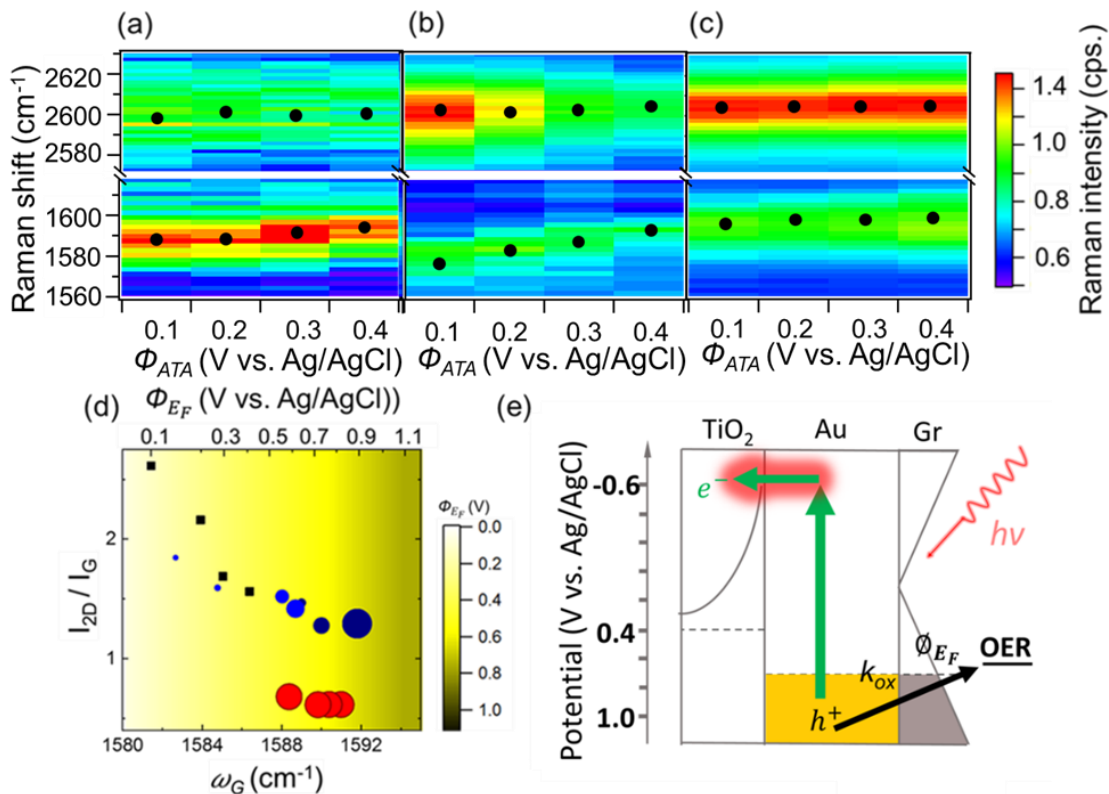


Figure 3.10. Raman shift of (a) Gr/SC-ATA (0.1 mW), (b) Gr/NSC-ATA (0.1 mW), and (c) Gr/NSC-ATA (1 mW) at potential from 0.1 to 0.4 V. (d) Correlation of Fermi level and catalytic performance of ATA. Red circles: Gr/SC-ATA; light blue circles: Gr/NSC-ATA (0.1 mW); dark blue circles: Gr/NSC-ATA (1 mW); black squares: Gr/Au/ITO. The diameter of each circle quantitatively indicates the magnitude of the photocurrent. (f) Proposed energy diagram of charge separation process of Gr/ATA for OER. The symbol  $k_{ox}$  indicates the OER rate constants of holes.

### 3.4 Conclusion

In conclusion, this work is the first to obtain the Fermi level of an ATA electrode during OER accelerated by modal strong coupling. This was done through graphene-based EC-SERS measurements. I have found that the positive Fermi level shift results from catalysis because of the promotion of electron-hole pair generation under modal coupling. These observed differences are derived from the different charge transfer efficiencies under modal strong coupling, which cannot be observed through other microscopic



measurements. This work provides practical information for understanding different OER activities. Additionally, our knowledge of internal properties of ATA can help in better designing new compositions of future photoconversion systems.

## References

1. Ciamician, G., The photochemistry of the future. *Science* **1912**, 36 (926), 385-394.
2. Manassen, J.; Cahen, D.; Hodes, G.; Sofer, A., Electrochemical, solid state, photochemical and technological aspects of photoelectrochemical energy converters. *Nature* **1976**, 263 (5573), 97-100.
3. Granqvist, C. G., Solar energy materials. *Advanced Materials* **2003**, 15 (21), 1789-1803.
4. Bamwenda, G. R.; Uesigi, T.; Abe, Y.; Sayama, K.; Arakawa, H., The photocatalytic oxidation of water to O<sub>2</sub> over pure CeO<sub>2</sub>, WO<sub>3</sub>, and TiO<sub>2</sub> using Fe<sup>3+</sup> and Ce<sup>4+</sup> as electron acceptors. *Appl. Catal. A* **2001**, 205 (1-2), 117-128.
5. Ishikawa, A.; Takata, T.; Kondo, J. N.; Hara, M.; Kobayashi, H.; Domen, K., Oxysulfide Sm<sub>2</sub>Ti<sub>2</sub>S<sub>2</sub>O<sub>5</sub> as a stable photocatalyst for water oxidation and reduction under visible light irradiation ( $\lambda \leq 650$  nm). *J. Am. Chem. Soc.* **2002**, 124 (45), 13547-13553.
6. Hitoki, G.; Takata, T.; Kondo, J. N.; Hara, M.; Kobayashi, H.; Domen, K., An oxynitride, TaON, as an efficient water oxidation photocatalyst under visible light irradiation ( $\lambda \leq 500$  nm). *Chem. Commun.* **2002**, (16), 1698-1699.
7. Brimblecombe, R.; Swiegers, G. F.; Dismukes, G. C.; Spiccia, L., Sustained water oxidation photocatalysis by a bioinspired manganese cluster. *Angew. Chem. Int. Ed.* **2008**, 47 (38), 7335-7338.
8. Li, Y.-F.; Liu, Z.-P.; Liu, L.; Gao, W., Mechanism and activity of photocatalytic oxygen evolution on titania anatase in aqueous surroundings. *J. Am. Chem. Soc.* **2010**, 132 (37), 13008-13015.
9. Nishijima, Y.; Ueno, K.; Kotake, Y.; Murakoshi, K.; Inoue, H.; Misawa, H., Near-infrared plasmon-assisted water oxidation. *J. Phys. Chem. Lett.* **2012**, 3 (10), 1248-1252.
10. Chemelewski, W. D.; Lee, H.-C.; Lin, J.-F.; Bard, A. J.; Mullins, C. B., Amorphous FeOOH oxygen evolution reaction catalyst for photoelectrochemical water splitting. *J. Am. Chem. Soc.* **2014**, 136 (7), 2843-2850.

11. Wang, D.; Sheng, T.; Chen, J.; Wang, H.-F.; Hu, P., Identifying the key obstacle in photocatalytic oxygen evolution on rutile TiO<sub>2</sub>. *Nat. Catal.* **2018**, *1* (4), 291-299.
12. Maier, S. A.; Atwater, H. A., Plasmonics: Localization and guiding of electromagnetic energy in metal/dielectric structures. *J. Appl. Phys.* **2005**, *98* (1), 10.
13. Willets, K. A.; Van Duyne, R. P., Localized surface plasmon resonance spectroscopy and sensing. *Annu. Rev. Phys. Chem.* **2007**, *58*, 267-297.
14. Jain, P. K.; El-Sayed, M. A., Plasmonic coupling in noble metal nanostructures. *Chem. Phys. Lett.* **2010**, *487* (4-6), 153-164.
15. Li, M.; Cushing, S. K.; Wu, N., Plasmon-enhanced optical sensors: a review. *Analyst* **2015**, *140* (2), 386-406.
16. Christopher, P.; Xin, H.; Marimuthu, A.; Linic, S., Singular characteristics and unique chemical bond activation mechanisms of photocatalytic reactions on plasmonic nanostructures. *Nat. Mater.* **2012**, *11* (12), 1044-1050.
17. Mukherjee, S.; Libisch, F.; Large, N.; Neumann, O.; Brown, L. V.; Cheng, J.; Lassiter, J. B.; Carter, E. A.; Nordlander, P.; Halas, N. J., Hot electrons do the impossible: plasmon-induced dissociation of H<sub>2</sub> on Au. *Nano Lett.* **2013**, *13* (1), 240-247.
18. Brongersma, M. L.; Halas, N. J.; Nordlander, P., Plasmon-induced hot carrier science and technology. *Nat. Nanotechnol.* **2015**, *10* (1), 25.
19. Shi, X.; Ueno, K.; Takabayashi, N.; Misawa, H., Plasmon-enhanced photocurrent generation and water oxidation with a gold nanoisland-loaded titanium dioxide photoelectrode. *J. Phys. Chem. C* **2013**, *117* (6), 2494-2499.
20. Tian, Y.; Tatsuma, T., Mechanisms and applications of plasmon-induced charge separation at TiO<sub>2</sub> films loaded with gold nanoparticles. *J. Am. Chem. Soc.* **2005**, *127* (20), 7632-7637.
21. Du, L.; Furube, A.; Yamamoto, K.; Hara, K.; Katoh, R.; Tachiya, M., Plasmon-induced charge separation and recombination dynamics in gold–TiO<sub>2</sub> nanoparticle systems: dependence on TiO<sub>2</sub> particle size. *J. Phys. Chem. C* **2009**, *113* (16), 6454-6462.
22. Mubeen, S.; Lee, J.; Singh, N.; Krämer, S.; Stucky, G. D.; Moskovits, M., An autonomous photosynthetic device in which all charge carriers derive from surface plasmons. *Nat. Nanotechnol.* **2013**, *8* (4), 247-251.

23. Kazuma, E.; Sakai, N.; Tatsuma, T., Nanoimaging of localized plasmon-induced charge separation. *Chem. Commun.* **2011**, 47 (20), 5777-5779.
24. Saito, K.; Tanabe, I.; Tatsuma, T., Site-Selective Plasmonic Etching of Silver Nanocubes. *J. Phys. Chem. Lett.* **2016**, 7 (21), 4363-4368.
25. Minamimoto, H.; Toda, T.; Futashima, R.; Li, X.; Suzuki, K.; Yasuda, S.; Murakoshi, K., Visualization of active sites for plasmon-induced electron transfer reactions using photoelectrochemical polymerization of pyrrole. *J. Phys. Chem. C* **2016**, 120 (29), 16051-16058.
26. Linic, S.; Christopher, P.; Ingram, D. B., Plasmonic-metal nanostructures for efficient conversion of solar to chemical energy. *Nat. Mater.* **2011**, 10 (12), 911-921.
27. Mayer, K. M.; Hafner, J. H., Localized surface plasmon resonance sensors. *Chem. Rev.* **2011**, 111 (6), 3828-3857.
28. Nishijima, Y.; Ueno, K.; Yokota, Y.; Murakoshi, K.; Misawa, H., Plasmon-assisted photocurrent generation from visible to near-infrared wavelength using a Au-nanorods/TiO<sub>2</sub> electrode. *J. Phys. Chem. Lett.* **2010**, 1 (13), 2031-2036.
29. Jye  $\text{\AA}$ si, K., Single-crystal caged gold nanorods with tunable broadband plasmon resonances. *Chem. Commun.* **2013**, 49 (83), 9630-9632.
30. Wu, X.; Centeno, A.; Zhang, X.; Darvill, D.; Ryan, M. P.; Riley, D. J.; Alford, N. M.; Xie, F., Broadband plasmon photocurrent generation from Au nanoparticles/mesoporous TiO<sub>2</sub> nanotube electrodes. *Sol. Energy Mater. Sol. Cells* **2015**, 138, 80-85.
31. Sung, Y.-M.; Lai, Y.-C.; Tsai, M.-F.; Hsieh, H.-H.; Yang, M.-H.; Wei, P. P.; Yeh, C.-S.; Hsu, F.-C.; Chen, Y.-F., Broad band plasmonic nanomaterials for high performance solar cells. *J. Mater. Chem. C* **2016**, 4 (3), 513-520.
32. Tang, M.; Sun, B.; Zhou, D.; Gu, Z.; Chen, K.; Guo, J.; Feng, L.; Zhou, Y., Broad-band plasmonic Cu-Au bimetallic nanoparticles for organic bulk heterojunction solar cells. *Org. Electron.* **2016**, 38, 213-221.
33. Naldoni, A.; Guler, U.; Wang, Z.; Marelli, M.; Malara, F.; Meng, X.; Besteiro, L. V.; Govorov, A. O.; Kildishev, A. V.; Boltasseva, A., Broadband hot - electron collection for solar water splitting with plasmonic titanium nitride. *Adv. Optical Mater.* **2017**, 5 (15), 1601031.

34. Fu, N.; Bao, Z. Y.; Zhang, Y.-L.; Zhang, G.; Ke, S.; Lin, P.; Dai, J.; Huang, H.; Lei, D. Y., Panchromatic thin perovskite solar cells with broadband plasmonic absorption enhancement and efficient light scattering management by Au@ Ag core-shell nanocuboids. *Nano Energy* **2017**, *41*, 654-664.
35. Luo, M.; Shen, S.; Zhou, L.; Wu, S.; Zhou, Y.; Chen, L., Broadband, wide-angle, and polarization-independent metamaterial absorber for the visible regime. *Optics express* **2017**, *25* (14), 16715-16724.
36. Wang, W.; Qu, Y.; Du, K.; Bai, S.; Tian, J.; Pan, M.; Ye, H.; Qiu, M.; Li, Q., Broadband optical absorption based on single-sized metal-dielectric-metal plasmonic nanostructures with high- $\epsilon$  "metals. *Applied Physics Letters* **2017**, *110* (10), 101101.
37. Lei, L.; Li, S.; Huang, H.; Tao, K.; Xu, P., Ultra-broadband absorber from visible to near-infrared using plasmonic metamaterial. *Optics express* **2018**, *26* (5), 5686-5693.
38. Lu, Y.; Dong, W.; Chen, Z.; Pors, A.; Wang, Z.; Bozhevolnyi, S. I., Gap-plasmon based broadband absorbers for enhanced hot-electron and photocurrent generation. *Scientific reports* **2016**, *6* (1), 1-9.
39. Ng, C.; Cadusch, J. J.; Dligatch, S.; Roberts, A.; Davis, T. J.; Mulvaney, P.; Gómez, D. E., Hot carrier extraction with plasmonic broadband absorbers. *ACS nano* **2016**, *10* (4), 4704-4711.
40. Reithmaier, J. P.; Sęk, G.; Löffler, A.; Hofmann, C.; Kuhn, S.; Reitzenstein, S.; Keldysh, L.; Kulakovskii, V.; Reinecke, T.; Forchel, A., Strong coupling in a single quantum dot–semiconductor microcavity system. *Nature* **2004**, *432* (7014), 197.
41. Bellessa, J.; Bonnard, C.; Plenet, J.; Mugnier, J., Strong coupling between surface plasmons and excitons in an organic semiconductor. *Phys. Rev. Lett.* **2004**, *93* (3), 036404.
42. Kato, F.; Minamimoto, H.; Nagasawa, F.; Yamamoto, Y. S.; Itoh, T.; Murakoshi, K., Active tuning of strong coupling states between dye excitons and localized surface plasmons via electrochemical potential control. *ACS Photonics* **2018**, *5* (3), 788-796.
43. Shi, X.; Ueno, K.; Oshikiri, T.; Sun, Q.; Sasaki, K.; Misawa, H., Enhanced water splitting under modal strong coupling conditions. *Nat. Nanotechnol.* **2018**, *13* (10), 953-958.
44. Nosaka, Y.; Norimatsu, K.; Miyama, H., The function of metals in metal-compounded semiconductor photocatalysts. *Chemical physics letters* **1984**, *106* (1-2), 128-131.

45. Wood, A.; Giersig, M.; Mulvaney, P., Fermi level equilibration in quantum dot– metal nanojunctions. *The Journal of Physical Chemistry B* **2001**, *105* (37), 8810-8815.
46. Burgeth, G.; Kisch, H., Photocatalytic and photoelectrochemical properties of titania–chloroplatinate (IV). *Coordination Chemistry Reviews* **2002**, *230* (1-2), 41-47.
47. Jakob, M.; Levanon, H.; Kamat, P. V., Charge distribution between UV-irradiated TiO<sub>2</sub> and gold nanoparticles: determination of shift in the Fermi level. *Nano letters* **2003**, *3* (3), 353-358.
48. Subramanian, V.; Wolf, E. E.; Kamat, P. V., Green emission to probe photoinduced charging events in ZnO– Au nanoparticles. Charge distribution and Fermi-level equilibration. *The Journal of Physical Chemistry B* **2003**, *107* (30), 7479-7485.
49. Ahn, G.; Kim, H. R.; Ko, T. Y.; Choi, K.; Watanabe, K.; Taniguchi, T.; Hong, B. H.; Ryu, S., Optical probing of the electronic interaction between graphene and hexagonal boron nitride. *ACS nano* **2013**, *7* (2), 1533-1541.
50. Zhou, R.; Yasuda, S.; Minamimoto, H.; Murakoshi, K., Sensitive Raman probe of electronic interactions between monolayer graphene and substrate under electrochemical potential control. *ACS omega* **2018**, *3* (2), 2322-2328.
51. Pisana, S.; Lazzeri, M.; Casiraghi, C.; Novoselov, K. S.; Geim, A. K.; Ferrari, A. C.; Mauri, F., Breakdown of the adiabatic Born–Oppenheimer approximation in graphene. *Nature materials* **2007**, *6* (3), 198.
52. Das, A.; Pisana, S.; Chakraborty, B.; Piscanec, S.; Saha, S. K.; Waghmare, U. V.; Novoselov, K. S.; Krishnamurthy, H. R.; Geim, A. K.; Ferrari, A. C., Monitoring dopants by Raman scattering in an electrochemically top-gated graphene transistor. *Nat. Nanotechnol.* **2008**, *3* (4), 210-215.
53. Casiraghi, C., Doping dependence of the Raman peaks intensity of graphene close to the Dirac point. *Phys. Rev. B* **2009**, *80* (23), 233407.
54. Lazzeri, M.; Mauri, F., Nonadiabatic Kohn anomaly in a doped graphene monolayer. *Phys. Rev. Lett.* **2006**, *97* (26), 266407.
55. Yan, J.; Zhang, Y.; Kim, P.; Pinczuk, A., Electric field effect tuning of electron-phonon coupling in graphene. *Phys. Rev. Lett.* **2007**, *98* (16), 166802.

56. Basko, D.; Piscanec, S.; Ferrari, A., Electron-electron interactions and doping dependence of the two-phonon Raman intensity in graphene. *Phys. Rev. B* **2009**, *80* (16), 165413.
57. Zhang, J.; Zhou, R.; Minamimoto, H.; Yasuda, S.; Murakoshi, K., Nonzero wavevector excitation of graphene by localized surface plasmons. *Nano Lett.* **2019**, *19* (11), 7887-7894.
58. Li, X.; Cai, W.; An, J.; Kim, S.; Nah, J.; Yang, D.; Piner, R.; Velamakanni, A.; Jung, I.; Tutuc, E., Large-area synthesis of high-quality and uniform graphene films on copper foils. *Science* **2009**, *324* (5932), 1312-1314.
59. Hoyer, P.; Weller, H., Potential-dependent electron injection in nanoporous colloidal ZnO films. *The Journal of Physical Chemistry* **1995**, *99* (38), 14096-14100.
60. Subramanian, V.; Wolf, E. E.; Kamat, P. V., Catalysis with TiO<sub>2</sub>/gold nanocomposites. Effect of metal particle size on the Fermi level equilibration. *Journal of the American Chemical Society* **2004**, *126* (15), 4943-4950.
61. H. Minamimoto, K. Y., R. Zhou, X. Li, S. Yasuda, K. Murakoshi, Potential Energy Shift of the Fermi Level at Plasmonic Structures for Light-Energy Conversion Determined by Graphene-Based Raman Measurements. *Journal of physical chemistry C* **2020**.
62. Lee, J. E.; Ahn, G.; Shim, J.; Lee, Y. S.; Ryu, S., Optical separation of mechanical strain from charge doping in graphene. *Nat. Commun.* **2012**, *3* (1), 1-8.
63. Kongkanand, A.; Kamat, P. V., Electron storage in single wall carbon nanotubes. Fermi level equilibration in semiconductor-SWCNT suspensions. *ACS nano* **2007**, *1* (1), 13-21.
64. Ikeda, K.; Takase, M.; Hayazawa, N.; Kawata, S.; Murakoshi, K.; Uosaki, K., Plasmonically nanoconfined light probing invisible phonon modes in defect-free graphene. *J. Am. Chem. Soc.* **2013**, *135* (31), 11489-11492.
65. Kavan, L.; Gräzel, M.; Gilbert, S.; Klemenz, C.; Scheel, H., Electrochemical and photoelectrochemical investigation of single-crystal anatase. *J. Am. Chem. Soc.* **1996**, *118* (28), 6716-6723.

## *Chapter 4.*

# **Investigation on the unique reaction mechanism of OER on plasmonic photoelectrode**

---

### **4.1 Introduction**

Oxygen evolution reaction (OER) has attracted great attention during the last few decades due to its prime role in water splitting. However, OER is not kinetically favored because it includes four proton-coupled electron transfers and oxygen-oxygen bond formation processes. Recently, the plasmonic photoconversion system is proved as a promising way for efficient OER.<sup>1-3</sup> The plasmonic photoconversion electrode is the combination of the wide-gap semiconductor electrode and the plasmonic metal nanostructures. Under the visible light illumination, hot electrons are injected to the conduction band of semiconductor. Because of the injection of charge carriers into the semiconductor beyond the Schottky-barriers, the recombination of electrons and holes can be reduced, resulting in the efficient multiple electron transfer process. Plenty of work has been to improve the catalysis performance of the plasmonic OER, as discussed in Chapter 1. However, about the reaction mechanism of OER on plasmonic system is still under investigation.

Surface enhanced Raman scattering (SERS) is a great way to investigate the reaction mechanism. Yeo *et al.* has applied in situ electrochemical SERS to observe the intermediate species formed during water oxidation at different applied potential and provide the detailed understanding about the reaction mechanism of OER on gold catalysis.<sup>4</sup> According to their research, Au(OH)<sub>3</sub> and AuOOH is generated as the precursor of OER depending on the electrode potential. Based on their research, in this chapter, we fabricated Au island on the cleaned TiO<sub>2</sub> (110) single crystal as the plasmonic electrode for photoconversion experiment. Potential dependence on the photocurrent values at different pH was measured. The intermediate species was also investigated by in situ electrochemical SERS measurements to understand the detailed mechanism of plasmonic OER. Koper *et al.* investigated the water splitting mechanism by combination of theoretical and experiment method and demonstrated the oxide decomposition mechanism which enriched the previous mechanism.<sup>5</sup>

## 4.2 Experimental

### 4.2.1 Preparation of the TiO<sub>2</sub> substrate

TiO<sub>2</sub> (110) single crystal was first rinsed by acetone and milli-Q water for 3~4 times. To etch the surface of TiO<sub>2</sub>, the substrates was immersed in 20% HF solution for 15 ~20 min. Finally, the cleaned TiO<sub>2</sub> substrate was annealed at 600 °C with the scheme shown in Fig.4.1 to obtain the atomically smooth surface.

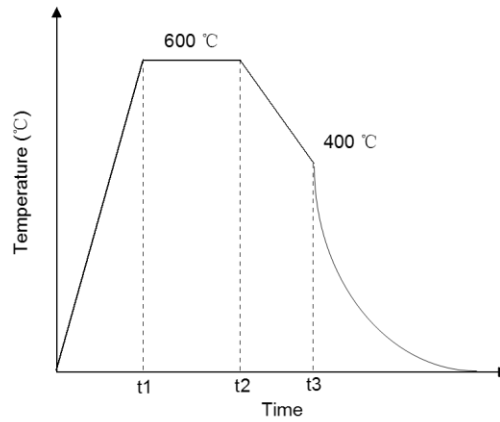


Figure 4.1. The recipe for TiO<sub>2</sub> annealing. t<sub>1</sub> was 2.15 h, t<sub>1</sub>~t<sub>2</sub> was 2.3 h and t<sub>2</sub>~t<sub>3</sub> was 1.45 h.

### 4.2.2 Preparation of Au islands

A 5 nm Au film was deposited on the surface of TiO<sub>2</sub> by electron beam evaporation with a deposition rate of 20 nm/s. After that, the substrate was annealed to form random Au island structures. The recipe of annealing temperature rise is provided in Fig.4.2. The surface image of the electrode was shown in Fig. 4.3.



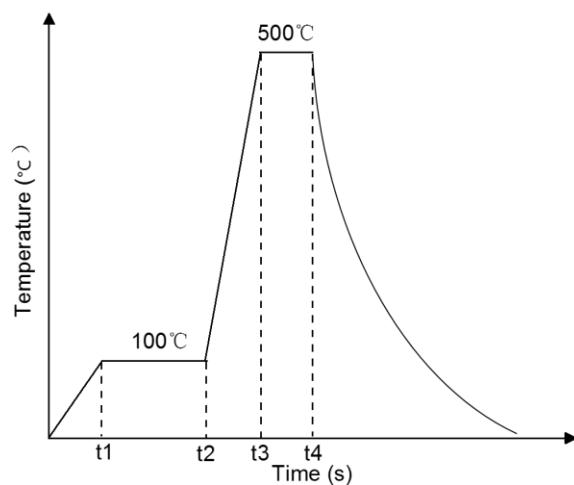


Figure 4.2. The recipe for Au annealing.  $t_1$ ,  $t_1 \sim t_2$ , and  $t_2 \sim t_3$ , and  $t_3 \sim t_4$  were 0.5, 1, 0.5 and 0.5 h, respectively.

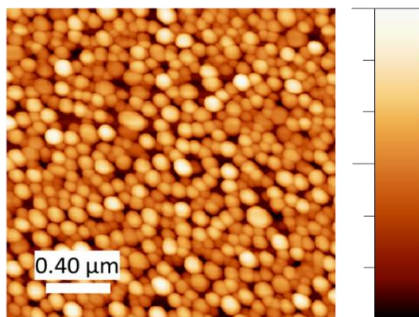


Figure 4.3. AFM image of Au island /  $\text{TiO}_2$  (110).

### 4.2.3 Preparation of Au dimer

The preparation method of Au dimer was similar as described in chapter 2. The monolayer PS beads mask was prepared on  $\text{TiO}_2$  surface. of the diameter of PS bead was 200 nm. After that, the Au thin layer was deposited with different angles of  $14^\circ \sim 1^\circ$  and each thickness was 30 nm. Figure 4.4 (a) shows the SEM image of Au dimer /  $\text{TiO}_2$  substrate. From it, the fine triangle structure could be confirmed. The extinction spectra obtained was shown in Fig. 4.4 (b). The wavelength in this case was about 830 nm.

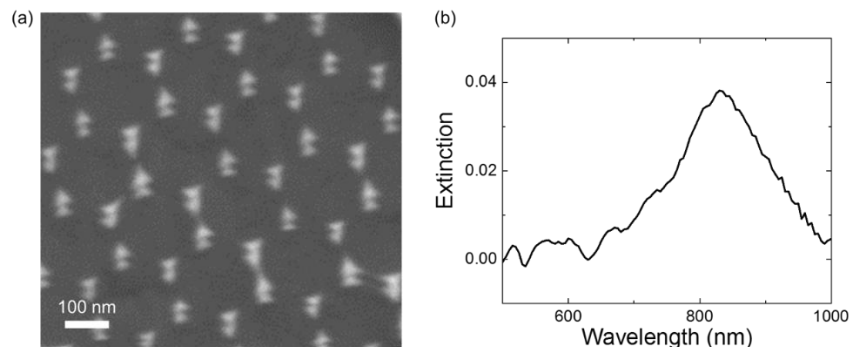


Figure 4.4. (a) SEM of Au dimer /  $\text{TiO}_2(110)$ . (b) Extinction of Au dimer /  $\text{TiO}_2(110)$ .

#### 4.2.4 Photoelectrochemical measurement

The conventional three-electrodes cell was used to measure the photocurrent (RE: Ag/AgCl, CE: Pt coil and WE: Au island /  $\text{TiO}_2(110)$ ). Visible light (540 ~ 800 nm) with 12 mW was illuminated onto the electrode. For the examination of pH dependence, neutral (0.5 M  $\text{NaClO}_4\text{aq.}$ ), basic (0.1 M  $\text{NaOHaq.}$ ), and acidic (0.1 M  $\text{HClO}_4\text{aq.}$ ) solutions were used. All measurements were carried out under Ar atmosphere.

#### 4.2.5 In situ electrochemical-SERS measurement

Electrochemical SERS measurements were conducted using a three-electrode system (W.E.: Au dimer /  $\text{TiO}_2(110)$ , C.E.: Pt, and R.E., Ag/AgCl). In order to reduce the resistance of solution, a supporting electrolyte of 0.5 M  $\text{NaClO}_4\text{aq.}$  was used. The 785 nm laser was used in the present measurements with a power of 0.1 mW.

### 4.3 Results and discussion

#### 4.3.1 Potential dependent photocurrent with different pH

Photocurrent under visible light was measured at different potential and pH. Figure 4.5 (a), (b), and (c) show the potential dependent photocurrent under acidic, neutral and

basic conditions, respectively. The photocurrent was about 0.03, 0.12 and 0.1  $\mu\text{A}/\text{cm}^2$  under acidic, neutral and basic condition respectively. The value of photocurrent at neutral condition was about almost 3 times higher than that of acidic condition.

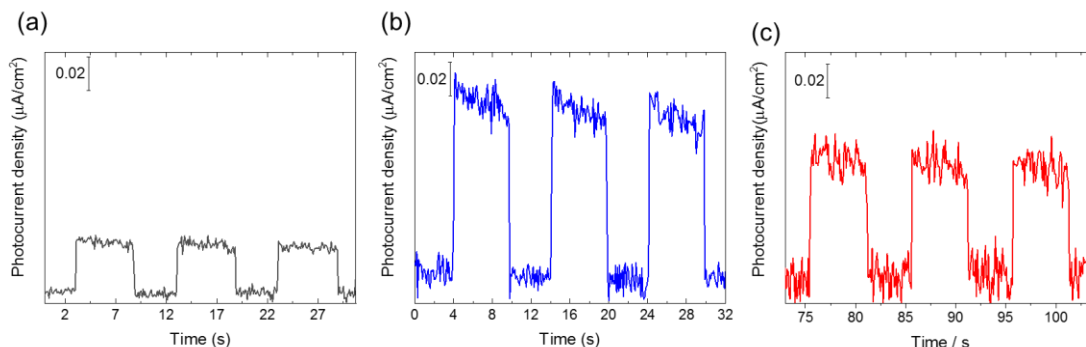


Figure 4.5. Photocurrent at (a) acidic (pH=0), (b) neutral (pH=7) and (c) (pH=13) basic condition (pH=13) respectively. The applied potential is 0.6 V was RHE.

#### 4.3.2 *In situ* SERS observation of the intermediate species of OER

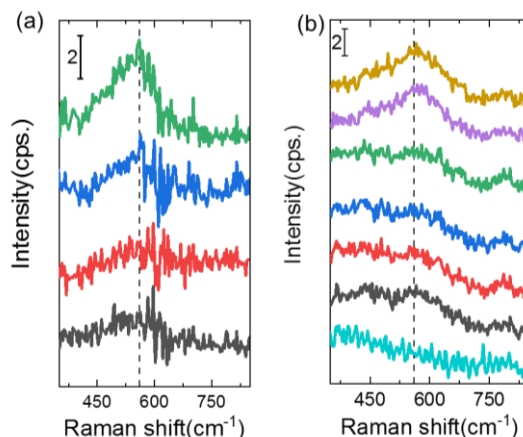


Figure 4.6. Differential in situ SERS of (a) Au /  $\text{TiO}_2$  and (b) Au / ITO. For Au /  $\text{TiO}_2$ , the applied potential is from 0.2 (up) to  $-0.4$  V (bottom). For Au / ITO, the applied potential is from 1.2 V (up) to  $-0.4$  V (bottom).

Since at neutral condition the photoelectrode exhibited highest catalysis performance, in situ SERS spectra was performed to investigate the intermediate species of OER during plasmonic photocatalysis. Since  $\text{TiO}_2$  (110) has a strong phonon peak at about  $610\text{ cm}^{-1}$ ,

which was near the vibration peak of Au-O, the differential spectra were prepared. The flat band potential of TiO<sub>2</sub> (110) in neutral condition is -0.57 V vs. Ag/AgCl,<sup>7</sup> indicating that water oxidation would not take place with a potential negative than -0.57 V. Therefore, I choose the Raman at -0.6 V as a background to obtain the Raman band of oxidation intermediate species. The calculation method was shown as follow formula:

$$Raman_x = Raw\ Raman_x - Raw\ Raman_{-0.6\ V} ,$$

where  $Raman_x$  indicated the Raman spectrum at each potential. The Raman spectrum of water oxidation on Au NSL/TiO<sub>2</sub> at different potential was shown in Fig. 4.6 (a). A Raman band at about 560 cm<sup>-1</sup> appears, which attributed to the Au-OOH species,<sup>4</sup> with different intensities at each potential. For common electrocatalysis of OER, Au-OOH was the intermediate specie for OER which generated at relatively high overpotential. In my case, the applied potential was much negative than the equilibrium potential of OER, indicating that because of plasmon effect, the catalysis efficiency was enhanced greatly. However, when the potential was 0 and 0.2 V, the intensity of Raman band reached maximum and remained stable, while at negative potential, the intensity increased as the anodic potential shift. The reason of this phenomenon was that when the applied potential was less positive, the height of schottky barrier was lower, increasing the possibility of recombination of carriers.

In order to compare the OER on the general metal electrode, I also measured the SERS spectra using Au / ITO substrate. When the potential were 1.0 and 1.2 V, an obvious peak appeared at about 560 cm<sup>-1</sup>, attributing to Au-OOH species. Obviously, the potential was much positive than that in Au / TiO<sub>2</sub> system. When the potentials were 0.2, 0.4, and 0.6 V, two peaks appeared at about 480 and 560 cm<sup>-1</sup>, corresponding to \*O on Au and Au-O respectively.<sup>4-5, 8</sup> From the spectra on Au /ITO at different potential, I could obtain the stepwise evolution of Au surface during OER.

#### 4.4 Conclusion

In this chapter, the unique catalysis performance of Au / TiO<sub>2</sub> plasmonic electrode for water oxidation was investigated. I first measured the pH dependent photocurrent at acidic, neutral and basic conditions. I could find that for all of the three cases, the on-set potential

for OER was much negative than the equilibrium potential of OER, indicating that plasmon could enable the reaction at low electric potential, thus saving electronic energy. Second, photoenergy conversion efficiency showed sensitive pH dependence. For common Au electrode, the catalysis performance increased when the pH increased. However, on the plasmonic anode system, the photocurrent became highest at neutral condition. This phenomenon would be discussed in detailed in the following chapter. I then conducted the in situ electrochemical SERS spectra to investigate the reaction mechanism in the neutral condition. Since a Raman shift at about  $560\text{ cm}^{-1}$  was observed on the surface of Au /TiO<sub>2</sub> from 0.61 V vs. RHE, I could imply that Au-OOH was generated at a potential much negative than the redox potential on common gold electrode. In another word, the catalysis performance was improved with the existence of plasmon.

## References

1. Nishijima, Y.; Ueno, K.; Kotake, Y.; Murakoshi, K.; Inoue, H.; Misawa, H., Near-Infrared Plasmon-Assisted Water Oxidation. *J. Phys. Chem. Lett.* **2012**, 3 (10), 1248-1252.
2. Shi, X.; Ueno, K.; Takabayashi, N.; Misawa, H., Plasmon-Enhanced Photocurrent Generation and Water Oxidation with a Gold Nanoisland-Loaded Titanium Dioxide Photoelectrode. *J. Phys. Chem. C* **2013**, 117 (6), 2494-2499.
3. Zhong, Y.; Ueno, K.; Mori, Y.; Shi, X.; Oshikiri, T.; Murakoshi, K.; Inoue, H.; Misawa, H., Plasmon - Assisted Water Splitting Using Two Sides of the Same SrTiO<sub>3</sub> Single-Crystal Substrate: Conversion of Visible Light to Chemical Energy. *Angew. Chem. Int. Ed.* **2014**, 53 (39), 10350-10354.
4. Yeo, B. S.; Klaus, S. L.; Ross, P. N.; Mathies, R. A.; Bell, A. T., Identification of Hydroperoxy Species as Reaction Intermediates in the Electrochemical Evolution of Oxygen on Gold. *ChemPhysChem* **2010**, 11 (9), 1854-1857.
5. Diaz-Morales, O.; Calle-Vallejo, F.; De Munck, C.; Koper, M. T., Electrochemical Water Splitting by Gold: Evidence for an Oxide Decomposition Mechanism. *Chem. Sci.* **2013**, 4 (6), 2334-2343.

6. Vázquez, G. C.; Peche-Herrero, M. A.; Maestre, D.; Cremades, A.; Ramírez-Castellanos, J.; González-Calbet, J. M.; Piqueras, J., Cr Doped Titania Microtubes and Microrods Synthesized by a Vapor–Solid Method. *CrystEngComm* **2013**, 15 (27), 5490-5495.
7. Enright, B.; Redmond, G.; Fitzmaurice, D., Spectroscopic Determination of Flatband Potentials for Polycrystalline TiO<sub>2</sub> Electrodes in Mixed Solvent Systems. *J. Phys. Chem.* **1994**, 98 (24), 6195-6200.
8. Desilvestro, J.; Weaver, M. J., Surface Structural Changes During Oxidation of Gold Electrodes in Aqueous Media as Detected Using Surface-Enhanced Raman Spectroscopy. *J. Electroanal. Chem. Interf. Electrochem.* **1986**, 209 (2), 377-386.

## *Chapter 5.*

# **Acceleration of water oxidation reaction on Ni-Loaded Au / TiO<sub>2</sub> electrode by plasmon**

---

### **5.1 Introduction**

As described in Chapter 1, nickel catalysis has been proved to be an effective and economic catalysis for water oxidation. However, the overpotential of water oxidation on Ni has been proved to be very large, which hindered the industrialization. Additionally, Ni catalysis is proved to exhibit high catalysis performance only at basic condition, while in the neutral condition, there still existing contradictions.<sup>1</sup>

Our previous work has discovered that with plasmon, the catalysis performance was enhanced dramatically. Remarkably, the catalysis performance exhibits maximum when pH was 9 with a laser of 785 nm. In order to understand the reaction mechanism, in situ SERS was conducted to observe the intermediate species. I found that when the pH was less than 10, Ni(OH)<sub>2</sub> was observed. When the pH was 11, a phase transition took place and full OH terminated Ni was observed and when continue to increase the pH to 13, partially O terminated NiOOH was observed. From the intermediate species I could say that CPET (concerted proton and electron transfer) took place, which has lower activation barrier therefore the catalysis performance was enhanced.<sup>2</sup>

In order to understand the reaction mechanism more deeply especially from the point of rate determining step, in my experiment, three parts of work has been down. First, the layer thickness of Ni(OH)<sub>2</sub> was optimized for OER. Second, I prepared the plasmonic Ni(OH)<sub>2</sub> / Au / TiO<sub>2</sub> electrodes and applied them to the water oxidation reaction to investigate the relationship between the catalysis performance and pH. To understand the role of plasmon, Ni(OH)<sub>2</sub> / Au wire electrode was also prepared to enable electrocatalysis of water oxidation. Third, isotope effects using H<sub>2</sub><sup>18</sup>O and D<sub>2</sub>O have been examined for both the plasmonic and electrochemical catalysis system.

Our result indicated that the best layer number of Ni(OH)<sub>2</sub> is 2~3 L. For plasmonic Au / TiO<sub>2</sub> electrode, with visible light (540~800 nm), the maximum catalysis performance still took place at pH = 9 and for Ni loaded on Au wire, the catalysis performance increased with increase of pH. In the case of the isotope effect, I found that, for both the plasmonic and electrochemical

electrodes, the isotope effects of both D<sub>2</sub>O and H<sub>2</sub><sup>18</sup>O exhibit the distinct pH dependence, indicating the rate determining step (RDS) changed depending on pH values. Remarkably, the isotope effects of both D<sub>2</sub>O and H<sub>2</sub><sup>18</sup>O of electrochemical Ni(OH)<sub>2</sub> / Au wire electrode were more obvious than those with plasmon, indicating that the slow steps of water oxidation were accelerated by plasmon.

## 5.2 Experimental

### 5.2.1 Preparation of the Au / TiO<sub>2</sub> electrode

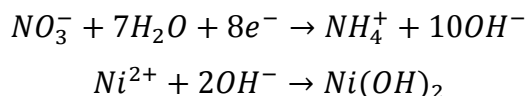
The preparation process of Au / TiO<sub>2</sub> electrode includes the cleaning of TiO<sub>2</sub>, electron beam evaporation and annealing of gold, which are same processes as those described in Chapter 3.

### 5.2.2 Cleaning Au wire

Au wire was washed with Piranha solution (H<sub>2</sub>SO<sub>4</sub>:H<sub>2</sub>O<sub>2</sub> = 3:1) to remove the organic contamination. Then, the wire was washed in boiled Milli Q water to remove the residual sulfonate ligand.

### 5.2.1 Deposition of nickel catalysis on Au / TiO<sub>2</sub> electrode and Au wire

Nickel was deposited on the surface of electrode by electrochemical method. A three electrode cell (WE: Au / TiO<sub>2</sub>, CE: Pt wire, RE: Ag/AgCl) was used, with electrolyte of 0.01 M Ni(NO<sub>3</sub>)<sub>2</sub> solution. The reaction of the electrodeposition is as follow:



Before depositing, I first measured the Faradic efficiency. Au wire was used as the working electrode and an amount of 100 μC electrons was passed through the circuit potentiostatically. After that, cyclic voltammetry experiment was conducted with this electrode in 0.1 M NaOH. By measuring the proportion of the area of the oxidation peak of Ni and the input amount of electrons, Faradic efficiency was calculated as 63%.<sup>1</sup> With this value, I deposited Ni(OH)<sub>2</sub> / Au / TiO<sub>2</sub> with layer numbers of <1, 2~3 L or 5~6 L. Same measurements were conducted using Au wire to determine the thickness of Ni(OH)<sub>2</sub>.



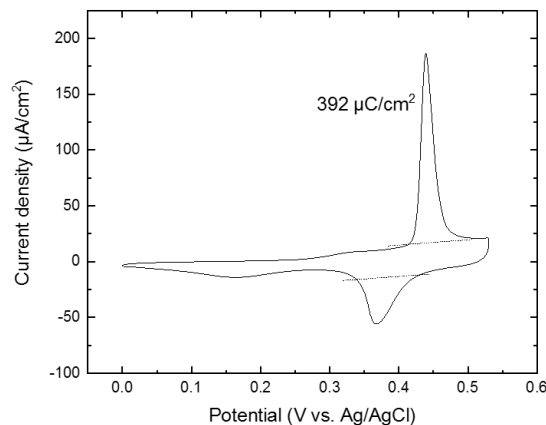


Figure 5.1. Cyclic voltammetry of  $\text{Ni(OH)}_2$  / Au wire in 0.1 M NaOH

### 5.2.2 Photoelectronic measurement

The photocurrent of  $\text{Ni(OH)}_2$  / Au /  $\text{TiO}_2$  was obtained using a cell same as the one described in Chapter 3. The light source was visible light (540~800 nm) with an intensity of  $3.56 \text{ mW/cm}^2$ . The electrolyte was a combination of  $\text{Na(OH)}_2$  and  $\text{HClO}_4$  with different proportion to obtain the pH from 7~13. For isotope effect, the solvent of water was replaced with  $\text{D}_2\text{O}$  and  $\text{H}_2^{18}\text{O}$ . For the  $\text{D}_2\text{O}$  electrolyte, the pH was measured as 0.4 plus the value obtained from pH test paper.<sup>3</sup>

## 5.3 Results and discussion

### 5.3.1 Optimization of the layer number of $\text{Ni(OH)}_2$

Previous research indicated that the layer number of  $\text{Ni(OH)}_2$  influenced the catalysis performance.<sup>4</sup> I prepared the electrode with  $\text{Ni(OH)}_2$  with different thickness and the photocurrent was measured on these three electrodes compared with bare Au /  $\text{TiO}_2$ , as shown in Fig.5.2.

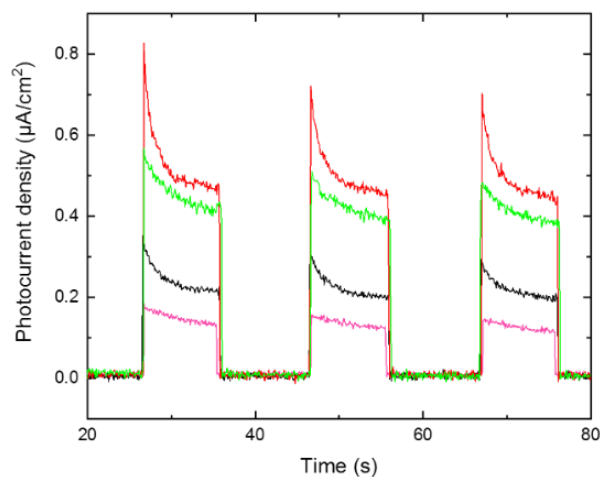


Figure 5.2. Photocurrent density of  $\text{Ni(OH)}_2$  / Au /  $\text{TiO}_2$  with different layer number. Red, green, black and purple lines indicated  $\text{Ni(OH)}_2$  of 2~3 L, 4~6 L, <1 L and bare Au /  $\text{TiO}_2$ , respectively.

From Fig.5.2 I observed the enhancement of catalysis performance by  $\text{Ni(OH)}_2$  compared with bare gold. However, the extent of enhancement was different with layer number. When the layer number was less than 1, the photocurrent was about  $0.2 \mu\text{A}/\text{cm}^2$ , which was about 1.5 times higher than that of Au /  $\text{TiO}_2$ . When the layer number was 2~3 L, the photocurrent increased dramatically and reached about  $0.5 \mu\text{A}/\text{cm}^2$ , however, when the layer number was increased to 5~6 L, the photocurrent decreased slightly compared with that of 2~3 L. Therefore, the optimized layer number was 2~3 L.

### 5.3.2 Investigation of water oxidation on $\text{Ni(OH)}_2$ / Au wire.

Before investigating the plamon system, the electrocatalysis of OER on  $\text{Ni(OH)}_2$  / Au wire was examined. I deposited 2~3 L  $\text{Ni(OH)}_2$  on the surface of Au wire as described above and measured the cyclic voltammetry at pH from 8 to 13, the results were shown in Fig. 5.3. From it was found that OER took place from about 1.5 V vs. RHE, which was much more positive than the equilibrium potential of OER ( $E = 1.23$  vs. NHE). The current density at 1.7 V vs. RHE was used to evaluate the catalysis performance and the relationship between the photocurrent at 1.7 V and pH was shown as the insert in the figure. The photocurrent increased when the electrolyte became more basic. In order to compare,

I also measured the cyclic voltammetry of bare Au wire at different pH and the result was shown in Fig.5.3. During the positive sweep, a peak appeared at about 1.25~1.35 V, which was attributed to the oxidation of Au oxides. This peak tended to be distributed along a plateau. The reason for this phenomenon was hysteresis. In this case, hysteresis was due to the post electrochemical processes. During the formation of dipole species ( $\text{Au}^{\delta+}\text{OH}^{\delta-}$ ), when the coverage increased, the repel between each species also increased, raised the energy required to produce more dipoles. Therefore, there was an increase in potential with increasing coverage. During the negative sweep, these dipole species were reduced progressively, no additional electrostatic repulsion barrier was required, therefore, the reduction peak was sharp. I also observed that the oxidation and reduction peak in this CV showing dependence on pH, as the oxidation peak appeared at more negative potential when increasing the pH while the reduction peak tended to occur at more positive potential. This was because the existence of hydrous species.<sup>5</sup>

The water oxidation reaction on bare gold wire took place from about 1.6 V. I also adopted the photocurrent at 1.7 V to evaluate the catalysis performance. The relationship between the photocurrent at 1.7 V and pH was shown in the insert figure and also it could be seen that the catalysis performance was higher in basic condition.

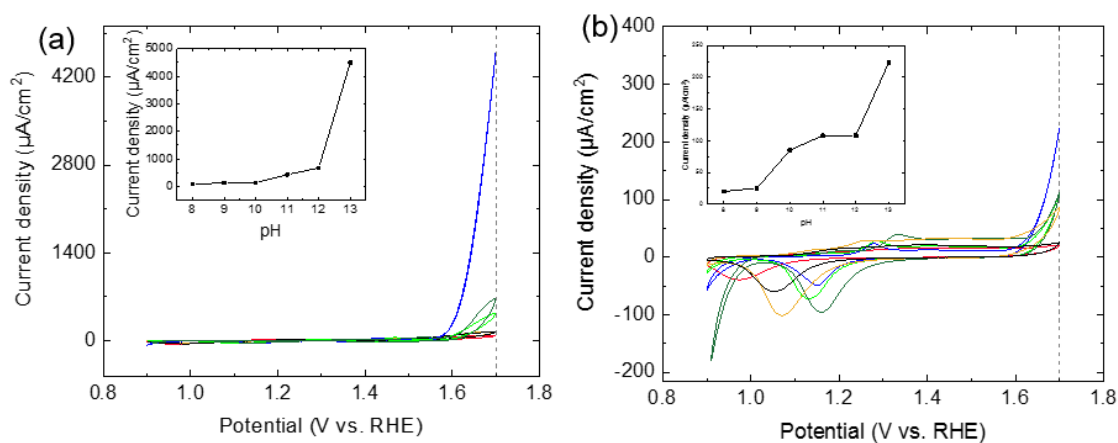


Figure 5.3. Cyclic voltammetry of (a)  $\text{Ni}(\text{OH})_2$  / Au wire and (b) Au wire. Insert figures are relationship between pH and photocurrent at 1.7 V vs. RHE of  $\text{Ni}(\text{OH})_2$  / Au wire and Au wire. Green, red, yellow purple, cyan and red lines indicate pH from 13 to 8.

### 5.3.3 Investigation of water oxidation on Ni(OH)<sub>2</sub> / Au / TiO<sub>2</sub>

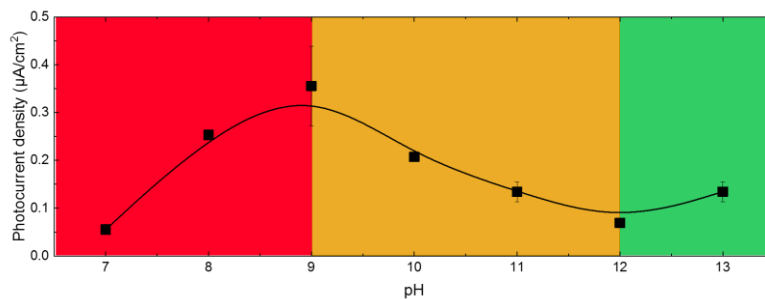


Figure 5.4. Photocurrent density on Ni(OH)<sub>2</sub> / Au / TiO<sub>2</sub> vs. pH. The photocurrent was obtained at 1.364 V vs. RHE with a power density of 3.56 mW/ cm<sup>2</sup>

Based on the understanding on conventional catalysis of OER on nickel catalysis, the plasmonic OER on Ni(OH)<sub>2</sub> / Au / TiO<sub>2</sub> was investigated. The photocurrent obtained at 1.35 V vs. RHE on Ni(OH)<sub>2</sub> / Au / TiO<sub>2</sub> under visible light illumination was shown in Fig.5.4. Different from conventional catalysis, the catalysis performance exhibited maximum at pH=9. When the pH was less than 9, the photocurrent increased with increase of pH. When the pH was located between 9 and 12, the photocurrent decreased. Finally, when pH continued to increase from pH = 12, the catalysis performance increased. This phenomenon indicated that the reaction mechanism of plasmonic photocatalysis was totally different from conventional electrocatalysis. A pH dependent transformation might be involved in the reaction.

### 5.3.4 Discussion about the reaction mechanism of plasmonic OER

In order to understand the unique reaction activity of plasmonic nickel catalysis for OER, isotope effect of both D/H and <sup>18</sup>O/O were investigated.

The isotope effect was discussed from the electrochemical point of view. For the system with plasmon excitation, the photocurrent was measured in H<sub>2</sub>O, D<sub>2</sub>O and H<sub>2</sub><sup>18</sup>O. The isotope effect was defined as the photocurrent obtain in D<sub>2</sub>O or H<sub>2</sub><sup>18</sup>O divided that obtained in H<sub>2</sub>O, as  $I_{\text{H}_2^{18}\text{O}}/I_{\text{H}_2\text{O}}$  and  $I_{\text{D}_2\text{O}}/I_{\text{H}_2\text{O}}$ . For the system in dark obtained on Au wire, the isotope effect was defined as the current density ratio of  $I_{\text{H}_2^{18}\text{O}}/I_{\text{H}_2\text{O}}$  and  $I_{\text{D}_2\text{O}}/I_{\text{H}_2\text{O}}$  obtained at 1.7 V vs. RHE from CV.

When pH=12, the photocurrent and CV obtained in H<sub>2</sub>O, D<sub>2</sub>O were shown in Fig. 5.5 (a) and (b). It was clear that the photocurrent was almost same in H<sub>2</sub>O, D<sub>2</sub>O, indicating there was no isotope effect of D with plasmon excitation, while in dark, the reaction activity decreased a lot, showing strong isotope effect, as Fig. 5.5 (c) indicated.

For the isotope effect of <sup>18</sup>O/O, the  $I_{\text{H}_2^{18}\text{O}}/I_{\text{H}_2\text{O}}$  with plasmonic excitation was about 0.6, much weaker than that in dark, as shown in Fig. 5.6

Under neutral condition when pH=8, similar analysis was conducted. For D/H, the photocurrent with plasmonic excitation and the CV obtained in dark is shown in Fig. 5.7 (a) and (b). In this case with plasmon excitation, the photocurrent in D<sub>2</sub>O was lower than that in H<sub>2</sub>O and the  $I_{\text{D}_2\text{O}}/I_{\text{H}_2\text{O}}$  was about 0.7. This isotope effect was still weaker than that in dark, as Fig. 5.7(c) indicated.

For <sup>18</sup>O/O, as shown in Fig. 5.8, the photocurrent obtained in H<sub>2</sub><sup>18</sup>O was almost as large as that in H<sub>2</sub>O, indicating that with plasmon excitation, there was almost no isotope effect. In dark, strong isotope effect could be observed.

From the result of isotope effect, the reaction mechanism of OER could be probed into. Under basic condition, for electrochemical OER on Ni in dark, much work has been done to expound the reaction mechanism.<sup>6-8</sup> One of the typical mechanism proposed by Nocera and Zhang was shown in Fig.5.9.<sup>9-10</sup>

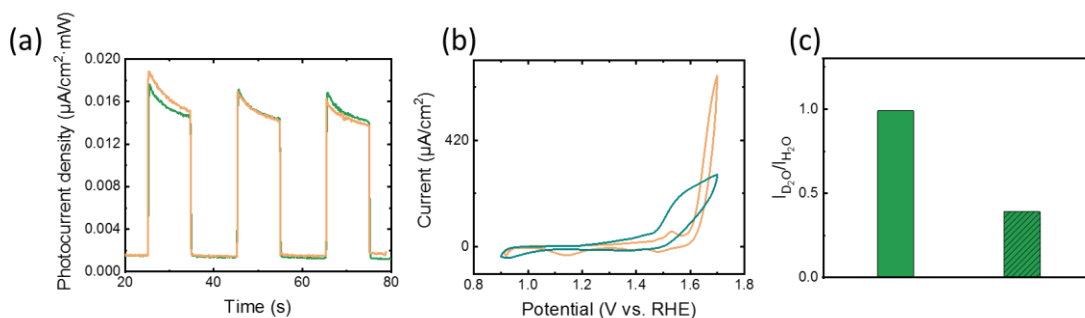


Figure 5.5. (a) photocurrent density obtained on Ni(OH)<sub>2</sub> / Au / TiO<sub>2</sub> at 1.364 V at pH=12. Pink line and green line indicated the photocurrent obtained from H<sub>2</sub>O and D<sub>2</sub>O respectively. (b) CV of Ni(OH)<sub>2</sub> / Au wire. Pink line and green line indicated the CV

obtained from H<sub>2</sub>O and D<sub>2</sub>O respectively. (c)  $I_{D_2O}/I_{H_2O}$  of Ni(OH)<sub>2</sub> / Au / TiO<sub>2</sub> (without shadow) and Ni(OH)<sub>2</sub> / Au wire (with shadow).

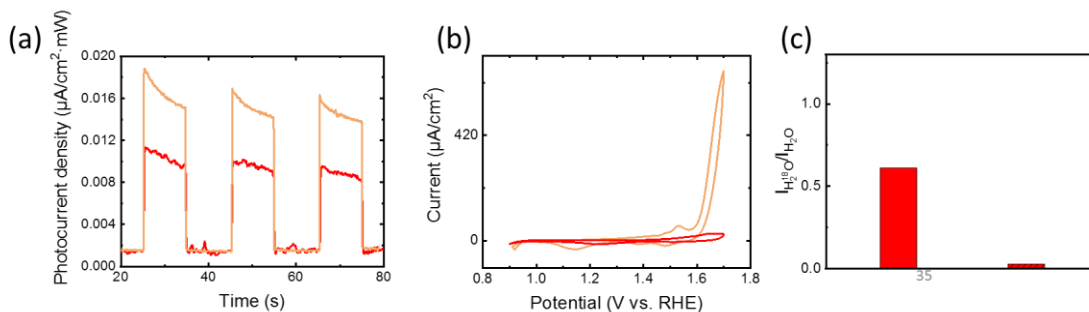


Figure 5.6. (a) photocurrent density obtained on Ni(OH)<sub>2</sub> / Au / TiO<sub>2</sub> at 1.364 V at pH=12. Pink line and red line indicated the photocurrent obtained from H<sub>2</sub>O and H<sub>2</sub><sup>18</sup>O respectively. (b) CV of Ni(OH)<sub>2</sub> / Au wire. Pink line and red line indicated the CV obtained from H<sub>2</sub>O and H<sub>2</sub><sup>18</sup>O respectively. (c)  $I_{H_2^{18}O}/I_{H_2O}$  of Ni(OH)<sub>2</sub> / Au / TiO<sub>2</sub> (without shadow) and Ni(OH)<sub>2</sub> / Au wire (with shadow).

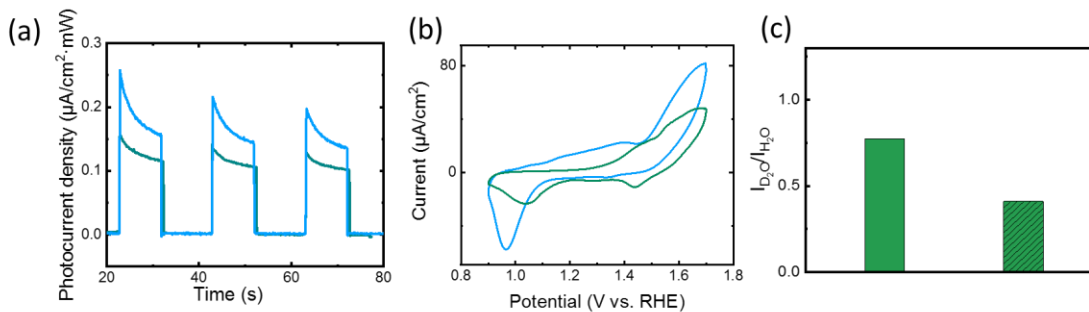


Figure 5.7. (a) photocurrent density obtained on Ni(OH)<sub>2</sub> / Au / TiO<sub>2</sub> at 1.364 V at pH=8. Blue line and green line indicated the photocurrent obtained from H<sub>2</sub>O and D<sub>2</sub>O respectively. (b) CV of Ni(OH)<sub>2</sub> / Au wire. Blue line and green line indicated the CV obtained from H<sub>2</sub>O and D<sub>2</sub>O respectively. (c)  $I_{D_2O}/I_{H_2O}$  of Ni(OH)<sub>2</sub> / Au / TiO<sub>2</sub> (without shadow) and Ni(OH)<sub>2</sub> / Au wire (with shadow).

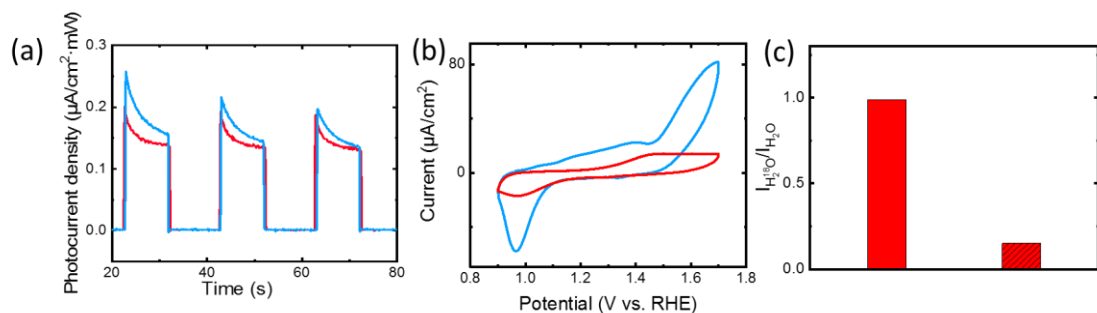


Figure 5.8. (a) photocurrent density obtained on  $\text{Ni(OH)}_2 / \text{Au} / \text{TiO}_2$  at 1.364 V at pH=8. Blue line and red line indicated the photocurrent obtained from  $\text{H}_2\text{O}$  and  $\text{H}_2^{18}\text{O}$  respectively. (b) CV of  $\text{Ni(OH)}_2 / \text{Au}$  wire. Blue line and red line indicated the CV obtained from  $\text{H}_2\text{O}$  and  $\text{H}_2^{18}\text{O}$  respectively. (c)  $I_{\text{H}_2^{18}\text{O}}/I_{\text{H}_2\text{O}}$  of  $\text{Ni(OH)}_2 / \text{Au} / \text{TiO}_2$  (without shadow) and  $\text{Ni(OH)}_2 / \text{Au}$  wire (with shadow).

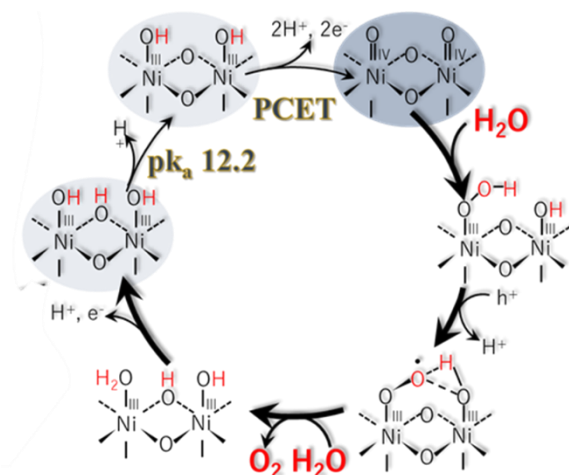


Figure 5.9. Electrochemical catalysis mechanism of water oxidation on Ni catalysis under basic condition. Blue shadow indicate the intermediate species observed by *in situ* SERS.<sup>9</sup>

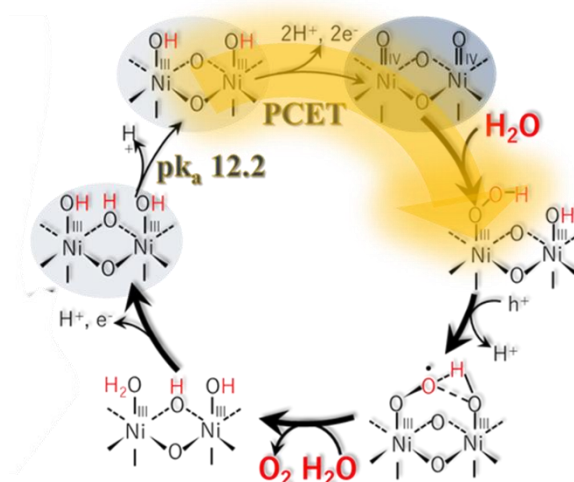


Figure 5.10. Proposed plasmonic photo catalysis mechanism of water oxidation on Ni catalysis under basic condition. Blue shadow indicated the intermediate species observed by *in situ* SERS and yellow arrow indicated the steps accelerated by plasmon.

When the  $pH=12$ , in the case of conventional electrocatalysis, as revealed by Nocera and Zhang<sup>9-10</sup>, Ni catalysis for OER went through several steps as shown in Fig. 5.9. the strong isotope effect of D and  $^{18}O$  indicated that both the proton transfer step and the O-O bond involving step were slow in this case. Previous *in situ* SERS study has revealed that the intermediate species was observed as  $Ni(OH)_2$ , fully OH-terminated, partially terminated  $NiOOH$  and nickel oxides, as indicated with blue shadow in Fig.5.9.<sup>11</sup> This results made me fix the slow proton transfer process on the PCET step as indicated in the figure. Since if one species was observed, the formation step toward this species was fast while the consumption step was slow. The deprotonation from  $Ni(OH)_2$  was also excluded, since the  $pH$  was large and preferred the proton transfer process. Additionally, since  $I_{H_2^{18}O}/I_{H_2O}$  was lower than  $I_{D_2O}/I_{H_2O}$ , indicating the O-O bond involving step was slower than the proton transfer step, thus the former is the rate determining step in this case.

With plasmon excitation, both the isotope effect of D and  $^{18}O$  became weaker, indicating both proton transfer and O-O involving step were accelerated. Since partially terminated  $NiOOH$  could be observed,<sup>11</sup> the accelerated “slow” proton transfer was still



the PCET step as shown in Fig. 5.10. Since  $I_{\text{H}_2^{18}\text{O}}/I_{\text{H}_2\text{O}}$  was still lower than  $I_{\text{D}_2\text{O}}/I_{\text{H}_2\text{O}}$ , the rate determining step was still the O-O bond involving step.

Under neutral condition, in the case of conventional electrocatalysis in dark, the reaction mechanism is similar, as Fig. 5.11. In this case, still both D and  $^{18}\text{O}$  showed strong isotope effect. Since fully OH terminated NiOOH was observed,<sup>11</sup> the slow proton transfer process was still the PCET step. The O-O bond involve step was still rate determining step.

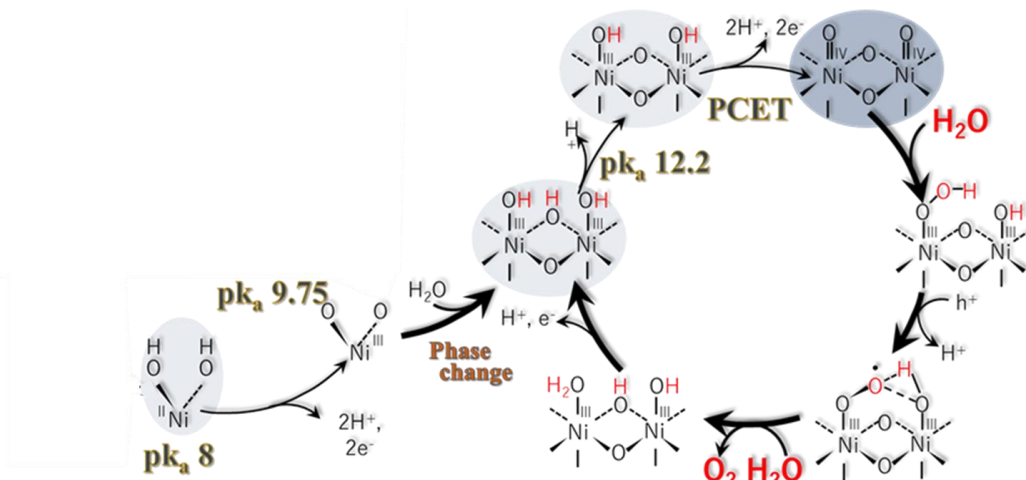


Figure 5.11. Electrochemical catalysis mechanism of water oxidation on Ni catalysis under neutral condition. Blue shadow indicate the intermediate species observed by *in situ* SERS.

With plasmon excitation, the current isotope effect indicated that OER took place under a new reaction mechanism, as shown in Fig. 5.12.<sup>11</sup> Also both isotope effect of D and  $^{18}\text{O}$  became weak, as Fig. 5.7 (c) and Fig. 5.8 (c) indicated. This result also meant that both proton transfer and O-O bond involving step was accelerated. Remarkably, it was found that the isotope effect of  $^{18}\text{O}$  almost disappear, as Fig. 5.8 (c) indicated. This meant that the O-O bond step was accelerated greatly, and the proton transfer step became rate determining step.

Fig 5.13 summarized the reaction activity and isotope effect of both D and  $^{18}\text{O}$  with plasmon excitation and under dark. The reaction activity decreased when increased the pH with plasmon excitation while increased with pH in dark, as described above. The obvious disappearance of  $^{18}\text{O}$  isotope effect could be observed in Fig. 5.13 (a).

Fig. 5.14 showed the two O-O bond involving steps with and without plasmon excitation under neutral condition. There are two pathways with plasmon excitation and both of them involve the covalently linked bridge structure, in another word, the distance between two O atoms in the reactant is shorter. In addition, the multi electron transfer process induced by collective excitation is in the system. Both of these two factors contribute to the lower reorganization energy, therefore, this step is accelerated greatly.<sup>12</sup> In dark, since the distance between O from H<sub>2</sub>O and O from NiOOH is longer and there was no multi electron transfer, thus the reorganization energy is high, resulting to the slow rate.

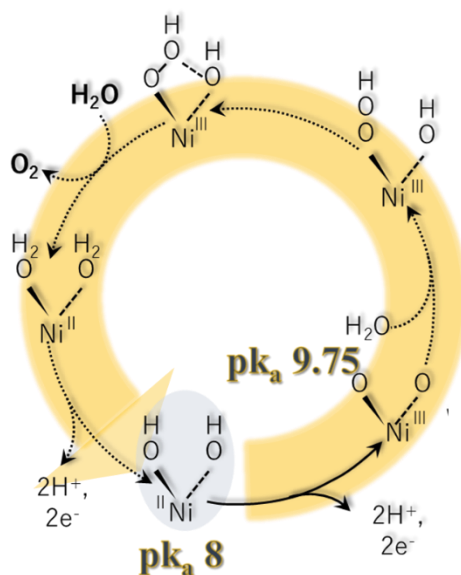


Figure 5.12. Proposed plasmonic photo catalysis mechanism of water oxidation on Ni catalysis under neutral condition. Blue shadow indicated the intermediate species observed by *in situ* SERS and yellow arrow indicated the steps accelerated by plasmon.<sup>11</sup>

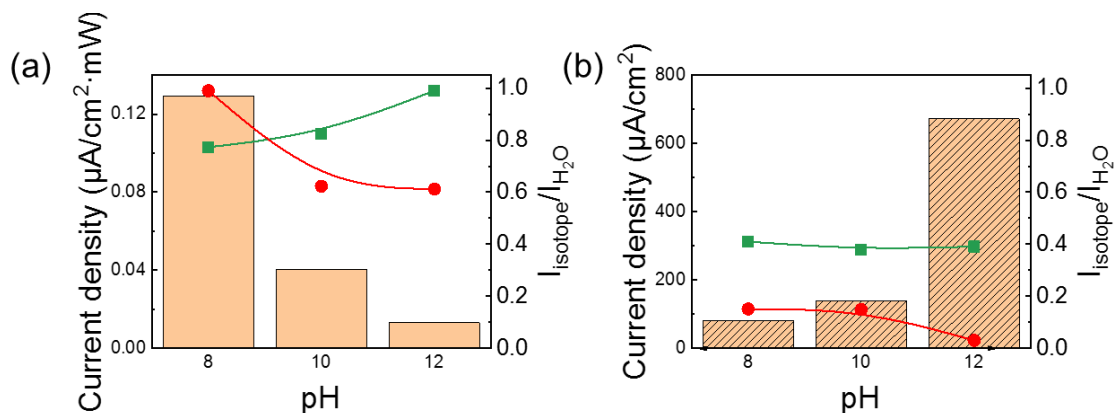


Figure 5.13. Reaction activity and isotope effect at different pH. (a)  $\text{Ni(OH)}_2 / \text{Au} / \text{TiO}_2$ . (b)  $\text{Ni(OH)}_2 / \text{Au}$  wire. Red circle and green square indicate  $I_{\text{H}_2^{18}\text{O}}/I_{\text{H}_2\text{O}}$  and  $I_{\text{D}_2\text{O}}/I_{\text{H}_2\text{O}}$  respectively.

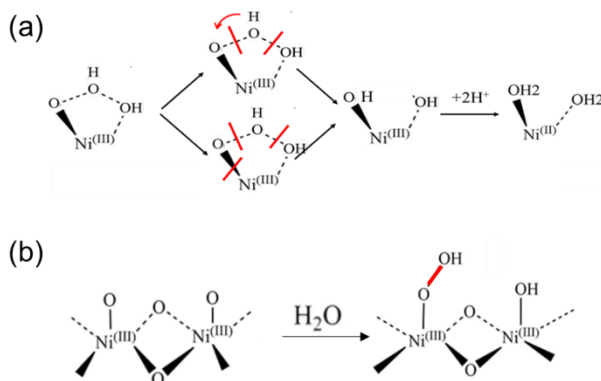


Figure 5.14. The O-O involving step under neutral condition with plasmon excitation (a) and (b) in dark.

## 5.4 Conclusion

The PCET process of water oxidation on Ni catalysis is closely related with the catalysis reaction and previous research has proved that plasmon could trigger the CPET and enhance the catalysis performance. However, the reaction mechanism need to be understand further. In order to probe into the mechanism deeply understand the influence of plasmon on the reaction, I measured the catalysis performance of both plasmonic and electrochemical catalysis of water oxidation system and observed the unique enhancement at neutral pH originated from plasmon. To understand the mechanism, I measure the

isotope effect of D and  $^{18}\text{O}$  of both electrochemical and plasmonic OER system. I found that for the former, when pH=8, the isotope effect of  $\text{D}_2\text{O}$  was more obvious than that of  $^{18}\text{O}$ , while for pH=10 and 12 the isotope effect of  $\text{H}_2^{18}\text{O}$  became more obvious. With the help of SERS spectra, I proposed the possible rate determining step. Based on the same thinking, the isotope effect of plasmonic system was also investigated. Similar tendency was observed, as for pH=8,  $\text{D}_2\text{O}$  reduced the reaction rate obviously while under basic condition,  $^{18}\text{O}$  showed more obvious isotope effect. Interestingly, the  $I_{\text{D}_2\text{O}}/I_{\text{H}_2\text{O}}$  and  $I_{\text{H}_2^{18}\text{O}}/I_{\text{H}_2\text{O}}$  value of plasmonic system were higher than those of electrocatalysis OER system, indicating that the slow steps was accelerated by plasmon.

## References

1. Kostecki, R.; McLarnon, F., Electrochemical and in Situ Raman Spectroscopic Characterization of Nickel Hydroxide Electrodes I. Pure Nickel Hydroxide. *J. Electrochem. Soc.* **1997**, 144 (2), 485-493.
2. Takashima, T.; Ishikawa, K.; Irie, H., Efficient Oxygen Evolution on Hematite at Neutral Ph Enabled by Proton-Coupled Electron Transfer. *Chem. Commun.* **2016**, 52 (97), 14015-14018.
3. Brodsky, C. N.; Hadt, R. G.; Hayes, D.; Reinhart, B. J.; Li, N.; Chen, L. X.; Nocera, D. G., In Situ Characterization of Cofacial Co (IV) Centers in  $\text{Co}_4\text{O}_4$  Cubane: Modeling the High-Valent Active Site in Oxygen-Evolving Catalysts. *P. Natl. Acad. Sci. USA* **2017**, 114 (15), 3855-3860.
4. Yeo, B. S.; Bell, A. T., In Situ Raman Study of Nickel Oxide and Gold-Supported Nickel Oxide Catalysts for the Electrochemical Evolution of Oxygen. *J. Phys. Chem. C* **2012**, 116 (15), 8394-8400.
5. Burke, L.; Nugent, P., The Electrochemistry of Gold: I the Redox Behaviour of the Metal in Aqueous Media. *Gold Bulletin* **1997**, 30 (2), 43-53.
6. Yang, C.; Fontaine, O.; Tarascon, J. M.; Grimaud, A., Chemical Recognition of Active Oxygen Species on the Surface of Oxygen Evolution Reaction Electrocatalysts. *Angew. Chem. Int. Ed.* **2017**, 56 (30), 8652-8656.

7. Shinagawa, T.; Garcia-Esparza, A. T.; Takanabe, K., Insight on Tafel Slopes from a Microkinetic Analysis of Aqueous Electrocatalysis for Energy Conversion. *Sci. Rep.* **2015**, 5, 13801.
8. Fletcher, S., Tafel Slopes from First Principles. *J. Solid State Electrochem.* **2009**, 13 (4), 537-549.
9. Bediako, D. K.; Surendranath, Y.; Nocera, D. G., Mechanistic Studies of the Oxygen Evolution Reaction Mediated by a Nickel–Borate Thin Film Electrocatalyst. *J. Am. Chem. Soc.* **2013**, 135 (9), 3662-3674.
10. Zhang, M.; De Respinis, M.; Frei, H., Time-Resolved Observations of Water Oxidation Intermediates on a Cobalt Oxide Nanoparticle Catalyst. *Nat. Chem.* **2014**, 6 (4), 362.
11. Suzuki, K. In-Situ Raman Observation of Reaction Intermediates at Plasmon-Induced Water Oxidation Processes. Hokkaido University, 2015.
12. Kim, Y.; Wilson, A. J.; Jain, P. K., The Nature of Plasmonically Assisted Hot-Electron Transfer in a Donor–Bridge–Acceptor Complex. *ACS Catal.* **2017**, 7 (7), 4360-4365.

## *Chapter 6.*

### **General Conclusion**

---

In this thesis, the plasmon induced electron transfer system was investigated. Not only focusing on preparing the catalytic electrode with high performance, I also hope to understand the intrinsic principle and origin of the enhancement resulting from plasmon. Based on this target, our work mainly including four parts.

First, I hope to extent the available range of solar spectra. Strong coupling was introduced to the system to realize this aim since two energy states were generated, increasing the width of absorption peak. In our experiment, Ag / MoS<sub>2</sub> was adopted to entered strong coupling regime. As a novel photoelectronic material, MoS<sub>2</sub> exhibits unique thickness dependent properties, providing a new thinking for the active tuning of the strong coupling state. It also has strong excitation effect and large dipole moment. For silver, due to its unique photoelectronic properties, the line width of its plasmonic peak is narrow, all of these properties making this system a good candidate for the research of strong coupling. I measured the extinction spectrum of Ag / MoS<sub>2</sub> in air and obtained the peak splitting which was proved to be strong coupling. I then prepared Ag on MoS<sub>2</sub> with different layer numbers and measured the in situ extinction spectra on the system. I found that on MoS<sub>2</sub> with 35 L, peak splitting could be observed at all applied potential while for MoS<sub>2</sub> with 164 L, peak splitting did not occur. I also found that the coupling strength of 35 L MoS<sub>2</sub> could be actively tuned by applying different potential. When the potential was  $-0.8$  V vs. Ag / AgCl, a splitting energy of 0.177 V could be obtained.

Then I hope to understand the system from the point of chemical reaction. In another word, I managed to investigate the unique reaction mechanism of plasmonic water oxidation on Au / TiO<sub>2</sub> electrode. Potential dependent photocurrent was measured at different pH, the principle of photocatalysis process of semiconductor/plasmon could be reflected from the results. Since the reaction was enabled via the electron and hole separation with the formation of Schottky barrier, the stability of photocurrent with pH was observed. The unique high catalysis performance at neutral was also observed compared with that at basic condition, which provided a promising prospect for utilization.

Based on the understanding from above work, the third part of our research was to try to enhance the catalysis of plasmonic electrode. I deposited nickel on Au / TiO<sub>2</sub> by electrochemical method and applied this electrode to the photocatalysis of OER. Compared with electrocatalysis on Ni / Au wire, the catalysis performance was enhanced greatly by plasmon. The reason is that the phase transition of nickel during OER on Ni / Au wire was skipped because of plasmon. Unlike the performance on Ni / Au wire, as showing high catalysis performance in more basic electrolyte, plasmonic system exhibited highest performance at neutral condition. By analyzing the isotope effect of D and <sup>18</sup>O, I inferred the possible rate determining step and revealed the pH dependent properties of these slow steps. The role of plasmon on the enhancement was also figured out as accelerating the slow steps.

Then I managed to understand the system from the respect of electrode. Fermi level of ATA electrode was determined by transferring graphene on it as a probe and measuring the situ SERS. By analyzing the properties of G and 2D band of graphene, I could obtain the relationship between Fermi level and G band position quantitatively. I found that the electrode with higher catalysis performance always processing more positive Fermi Level. From our results, the structural properties of electrode could also be reflected.

In conclusion, the unique plasmonic effect on the photoelectrochemical process was investigated in my thesis. The plasmonic photocatalysis of water oxidation was probed deeply, both from the respect of chemical reaction and the electronic properties of electrode. Our research could provide a solid base for the further optimization of water splitting.

## Acknowledgements

I am greatly indebted to my supervisor Professor Kei Murakoshi, for his great guidance, encouragement and support not only for my research but for my life. As a teacher, he was always patiently imparting knowledge to me; as a scientist, he was also creative and his attitude towards science was so rigorous that to be respected. As my supervisor, he also concerned about my life and provided me a lot of support. I am also impressed on his great enthusiastic and energetic attitude towards work. He also provided me a lot of opportunities of academic conferences to communicate with other researchers. Thanks to him, I spent a meaningful three years in Hokkaido University and I believe this experience will exert a profound influence on my future life.

I also would like to express my sincere gratitude to Professor Tetuya Taketugu, Professor Hiroki Habazaki and Professor Kosei Ueno for their kind attendance to my defense and valuable suggestions to my research. I am also grateful to Dr. Hiro Minamimoto for his kind support for my research. He provided me a much needed and perspective advises for my experiment and thesis and spent much time on discussing with my data and revising my documents. His rigorous attitude towards science and dedication to work inspired me a lot. Every step of my progress owes to his great effort.

I also would like to express my sincere appreciation to Professor Hiroaki Misawa and Dr. Xu Shi, who provided me extremely valuable suggestions and prepared ATA electrode with high quality when I was trying to measure Fermi level of ATA electrodes. Without their help, I could not obtain these important data.

I am also grateful to Dr. Ruifeng Zhou, Dr. Tomohiro Fukushima and Dr. Xiaowei Li for their valuable suggestions on my experiment. Dr. Ruifeng Zhou gave me a lot of suggestions on the optimization of my experiment and the Raman measurement of graphene. Dr. Tomohiro Fukushima suggested me a lot on my electrochemical measurement. Dr. Xiaowei Li helped me a lot when I prepared the strong coupling system between  $\text{MoS}_2$  and Ag.

Ms. Akiyama, Ms. Yonezawa and Ms. Hattori also helped me a lot during my life in Sapporo. Due to my poor Japanese, they helped me prepared a lot of document such as establishing bank account, paying for insurance and preparing the document for applying for my degree.

I also would like to express my appreciation to every member in Murakoshi's lab. Mr. Oikawa shared his experience of experiment with me selflessly and I am impressed with his talented ability. Mr. Oyamada, Mr. Hayashi and Mr. Suzuki supported me greatly when I just arrived in Japan. Of course during the whole three years they gave me a lot of help. They are very smart boys with great merits such as responsibility and hardworking and I learnt much from them. Mr. Sato is always be patient to me and spent much time on understanding my crappy Japanese and talking to me with easy understood Japanese. Mr. Miyauchi and Mr. Hasebe introduced a lot of interesting culture to me. All of them helped me a lot for my experiment. Mr. Homma, Mr. Komai, Mr. Cai and Mr. Iwahara also taught me a lot both in experiment but also in Japanese culture. Mr. Ashizawa, Mr. Suzuki, Mr. Miyoshi and Mr. Yoshimitsu also provide a lot of help for my research.

I also hope to express my thanks to my family and friends for their encouragement for my career. Without them I could not fulfill my target even with one step.

Yuchun WANG